People's Democratic Republic of Algeria
Ministry of Higher Education and Scientific Research
University of Saad Dahleb Blida 1
Faculty of Sciences
Physics Department

Master's Thesis in Theoretical Physics

Reconstructing the Higgs signal from ATLAS data

Prepared by: **Amira BENHOUHOU** and **Khaoula HAMMOUDENE**

Defended in February 11th, 2021 before the jury composed of:

Dr B. SI LAKHAL	Professor	Ecole Nationale Polytechnique - Algiers	President
Dr A. YANALLAH	MCB	University of Saad Dahleb - Blida 1	Examiner
Dr N. BOUAYED	MCA	University of Saad Dahleb - Blida 1	Supervisor
Dr M. OULD MOHAMED	MCB	University of Saad Dahleb - Blida 1	Co-Supervisor

2019/2020 - Blida 1

Abstract

After being hunted for about half a century since its prediction by Peter Higgs, the Higgs boson was finally discovered by CERN at the Large Hadron Collider (LHC) in July 2012. The experimental confirmation of its existence marked the last step of completing the Standard Model of electroweak and strong interactions, and started the era of Higgs precision tests to look for new physics. This discovery is particularly important, since it confirms the consistency of the Higgs mechanism in generating particle masses through the first ever discovered scalar field.

In this master degree thesis, we take a deeper look at the way the Higgs has been discovered at LHC. Firstly, we aim attention at the whole process taking place at LHC, by focusing particularly on the $pp \to H \to ZZ^* \to 4$ leptons golden channel. Starting from the proton-proton collision, all the way to the detection of the final state four leptons in the ATLAS detector. Secondly, taking MadGraph5_aMC@NLO as our event generator, we focus on the simulation of the parton collision events leading us to the four leptons final state. Here, we lay stress upon the way our knowledge about Standard Model interactions, parton showering, hadronization and detector processes is involved in simulating events. Lastly, we make use of the ATLAS Open Data datasets. We compare the given experimental data with the corresponding simulated ones, then we reconstruct the Higgs signal using some statistical tools.

Keywords : Higgs boson, Standard Model, LHC, ATLAS experiment.

Résumé

Après avoir été traqué pendant près d'un demi-siècle depuis sa prédiction par Peter Higgs, le boson de Higgs fut finalement découvert par le CERN au grand collisionneur de hadrons (LHC) en juillet 2012. La confirmation expérimentale de son existence a marqué la dernière étape qui compléta le Modèle Standard des interactions électrofaibles et fortes, et a initié l'ère des tests de précision du Higgs à la recherche de la nouvelle physique. Cette découverte est particulièrement importante, puisqu'elle confirme la consistance et la validité du mécanisme de Higgs dans la génération des masses des particules à travers le premier champ scalaire découvert.

Dans cette thèse de master, nous regardons de plus près comment le boson de Higgs a été découvert au LHC. D'abord, nous portons l'attention sur tout le processus se déroulant au LHC, en nous concentrant particulièrement sur le canal d'or $pp \to H \to ZZ^* \to 4$ leptons. À partir de la collision proton-proton jusqu'à la détection des quatre leptons de l'état final dans le détecteur ATLAS. Ensuite, en prenant MadGraph5_aMC@NLO comme générateur d'événements, on se concentre sur la simulation des événements de collisions de partons nous menant vers l'état final des quatre leptons. Ici, nous mettons l'accent sur la manière dont nos connaissances sur les interactions du Modèle Standard, les cascades de partons, l'hadronisation et les processus de détection sont impliquées dans la simulation des événements. Enfin, nous utilisons les ensembles de données ATLAS Open Data. Nous comparons les données expérimentales fournies avec celles simulées correspondantes, puis nous reconstruisons le signal du Higgs en utilisant certains outils statistiques.

Mots-clés : boson de Higgs, Modèle Standard, LHC, expérience ATLAS.

ملخص

إن رحلة البحث التي دامت ما يقارب نصف قرن من الزمن، منذ التنبؤ به من طرف بيتر هيغز، كللت أخيرا باكتشاف بوزون هيغز من قبل CERN في مصادم الهدرونات الكبير (LHC) في جويلية 2012. التأكيد التجريبي لوجوده كانت الخطوة الأخيرة لاستكمال النموذج القياسي للقوة الكهروضعيفة والقوة النووية القوية، وبداية عهد جديد لاختبارات دقة الهيغز من أجل التطلع لفيزياء جديدة. يعد هذا الاكتشاف مهم بشكل خاص، لأنه يؤكد إتساق آلية هيغز في توليد كتل الجسيمات من خلال أول حقل سلمي تم اكتشافه.

في أطروحة الماستر هذه، نلقي نظرة أعمق على الطريقة التي تم بها اكتشاف هيغز في LHC . أولا، نبرز كل العمليات التي تجري في LHC مع التركيز بشكل خاص على القناة الذهبية $pp \to H \to ZZ^* \to 4l$. انطلاقا من تصادم بروتون - بروتون، وصولا إلى اكتشاف الحالة النهائية للبتونات الأربعة في الكاشف أطلس. ثانيا، باستعمال MadGraph5_aMC@NLO كمنشأ للأحداث، نولي اهتماما لمحاكاة أحداث تصادم البارتون التي تقودنا إلى الحالة النهائية للبتونات الأربعة. هنا، نؤكد على أن كل معرفتنا بتفاعلات النموذج القياسي، و شلالات البارتون و العمليات الهدرونية و عمليات الكشف معنية بمحاكاة الأحداث. أخيرا، نستخدم مجموعة بيانات أطلس المفتوحة. نقارن البيانات التجريبية المقدمة مع ما يقابلها من المحاكات. ثم نقوم بإعادة بناء إشارة هيغز باستعمال بعض الأدوات الإحصائية.

الكلمات المفتاحية : بوزون هيغز، النموذج القياسي، LHC، تجربة أطلس.

Dedications

To my dear late father,
This work is entirely dedicated to you,
You're no longer here with us,
But your memory keeps being my main source of motivation,
Thank you for having believed in me,
I wouldn't have come this far without you.

Amira BENHOUHOU

I dedicate this work to the most precious persons in my life. My dear mother, to my support in the world. My dear father, you are the only reason for not giving up despite all circumstances and difficulties.
To my brothers, and my sister for their observation supports.
I thank of course all my friends and relatives, without exception, to my esteemed teachers at all stages.

Khaoula HAMMOUDENE

Contents

List of Figures

List of Tables

Abbreviations

SM	Standard Model.
CERN	Centre Européen de Recherche Nucléaire.
LHC	Large Hadron Collider.
ATLAS	A Toroidal LHC ApparatuS.
CMS	Compact Muon Solenoid.
QED	Quantum Electro-Dynamics.
QCD	Quantum Chromo-Dynamics.
EW	Electro-Weak.
NLO	Next-to-Leading Order.
NNLO	Next-to-Next-to-Leading Order.
NNLL	Next-to-Next-to-Leading Logarithmic.
ggF	gluon-gluon Fusion.
VBF	Vector Boson Fusion.
LEP	Large Electron Positron.
ALICE	A Large Ion Collider Experiment.
LHCb	Large Hadron Collider beauty.
ID	Inner Detector.
MS	Muon Spectrometer.
CPU	Central Processing Unit.
HLT	High-Level Trigger.
SFOS	Same Flavor and Opposite Sign.
PDF	Parton Distribution Function.
pdf	probability density function.
MCEG	Monte Carlo Event Generator.
PS	Parton Shower.
HEP	High Energy Physics.

Introduction

A great way to make considerable progress in physics, is to come up with revolutionary ideas. Suggesting brand new theories and views, or general theories that can combine already existing and verified ones. These new theories are capable of giving not only the same results as the former ones (sometimes through applying approximations, limits or special cases...), but adds further to the comprehension of physics' phenomena. For example, Maxwell was the first one to link the electricity and magnetism. He considered them as different manifestations of the same phenomenon, combining them into one single branch of physics we call "the electromagnetism". Theoretical implications of it, especially regarding the speed of light, gave rise to the development of "the special relativity" by Einstein. Which in turn unified space and time.

And the best way to confirm the accuracy of a theory or prediction is through experimental approaches. This is what physicists were aiming for when they built the *Large Hadron Collider* (LHC): to unravel the missing pieces associated to the comprehension of the theory of fundamental interactions, the Standard Model. This theory has shown to be the most successful model of subatomic particles since its development in the 1960s. It provides an elegant mathematical framework, that describes the way the fundamental constituents of matter interact with one another, through the fundamental forces mediated by gauge bosons: the electromagnetic force carried by photons, the weak force by $W^{\pm}$ and Z bosons and the strong force by gluons. It succeeded in explaining several experimental results and precisely predicting different kinds of phenomena. Like the experimental confirmation of the existence of quarks in 1968, $W^{\pm}$ and Z bosons in 1983, top quark t in 1995, and the tau neutrino ν_{τ} in 2000.

However, it took almost half a century to discover the Higgs boson, the last missing piece of the Standard Model. This dicovery was announced in July 2012 by the ATLAS and CMS collaborations, with a mass around 125 GeV. The Higgs' existence was postulated to explain "how do particles acquire mass?". And thus in 2013, The Nobel Prize in Physics was handed jointly to Peter Higgs and François Englert for:
"The theoretical discovery of a mechanism that contributes to our understanding of the origin of mass of subatomic particles, and which recently was confirmed through the discovery of the predicted fundamental particle, by the ATLAS and CMS experiments at CERN's Large Hadron Collider" [1].

The aim of this master degree thesis, is to reconstruct and analyse the Higgs signal in the $pp \to H \to ZZ^* \to 4$ leptons golden channel with real and simulated data, and using statistical tools. This in order to better understand the importance of this discovery in the Standard Model, and why it is a huge step in the history of physics.

The content of our thesis is organised as follows:

- In the first chapter, we talk about the Higgs boson and its role in the Standard Model [2–6]. We explain the spontaneous breaking of the electroweak symmetry, as well as the generation of particle masses. We also look at the hadronic Higgs production and the Higgs decay modes.

- The second chapter is dedicated to the physics behind the Large Hadron Collider and the ATLAS detector. Why the LHC is designed the way it is, and what kind of observables and data it provides.

- As for the third chapter, after discussing the background estimation and event selection for the $pp \to H \to ZZ^* \to 4l$ channel, we'll be focusing on how events in the LHC are simulated. We take a deeper look at Madgraph5_aMC@NLO as a Monte Carlo event generator, and we use it to generate a process simulation as an example application.

- In the last chapter, we finally use data and simulation samples from the ATLAS Open Data datasets, to reconstruct histograms fitting the Higgs signal and background noise with data. Then we'll try to compare the simulated results with the experimental data using statistical tools, mainly by calculating the p-value.

Chapter 1

The Standard Model Higgs boson

1.1 What is the Standard Model Higgs Boson?

The Standard Model Higgs boson is the only scalar particle predicted by the Standard Model (SM) [2–6] of particle physics. It was hunted for half a century, to be finally discovered at the Large Hadron Collider (LHC) in July 2012, with a mass of $M_H = 125.36 \pm 0.41 GeV$ [7,8]. A chronology of the discoveries of the Standard Model particles is given in the Figure 1.1.

This scalar particle, before having been introduced in the weak and electromagnetic unified theory of the SM in 1967-1968 [2–6] , was hypothesized in 1964 through a classical formulation by P. Higgs [9], and separately through a quantum formulation by F. Englert and R. Brout [10]. The goal of the introduction of this particle in connection with gauge vector fields was to explain how we can avoid the unobserved massless spin zero particles predicted by Goldstone, when a continuous symmetry group leaves the Lagrangian but not the vacuum invariant [11, 12].

The main idea pointed out by P. Higgs, F. Englert and R. Brout was the introduction of the gauge invariance constraint simultaneously on both the scalar and the gauge Lagrangians. Then, similarly as done by Goldstone, they added the assumption that the scalar field $\Phi(x)$, ruled by a $\Phi^4(x)$ self interaction, undergoes a spontaneous breaking of its degenerate minima states, that brings it to one specific vacuum. This vacuum breaks the gauge symmetry but the Lagrangian is still gauge and Lorentz invariant. Despite the fact that this procedure gives the scalar Higgs boson its mass as mentioned by Goldstone, it furthermore allows weak gauge vector bosons to acquire finite values of mass. It is worthwhile to point out here that G. S. Guralnik, C. R. Hagen and T. W. B. Kibble showed explicitely that, in this formulation, the disappearance of the massless unphysical scalar degrees of freedom makes the gauge vector degrees of freedom acquire their corresponding physical masses [13]. This procedure that generates the gauge vector boson masses in the SM is called *the Higgs mechanism*.

Let us now look more deeply into how the mass of SM elementary particles is generated.

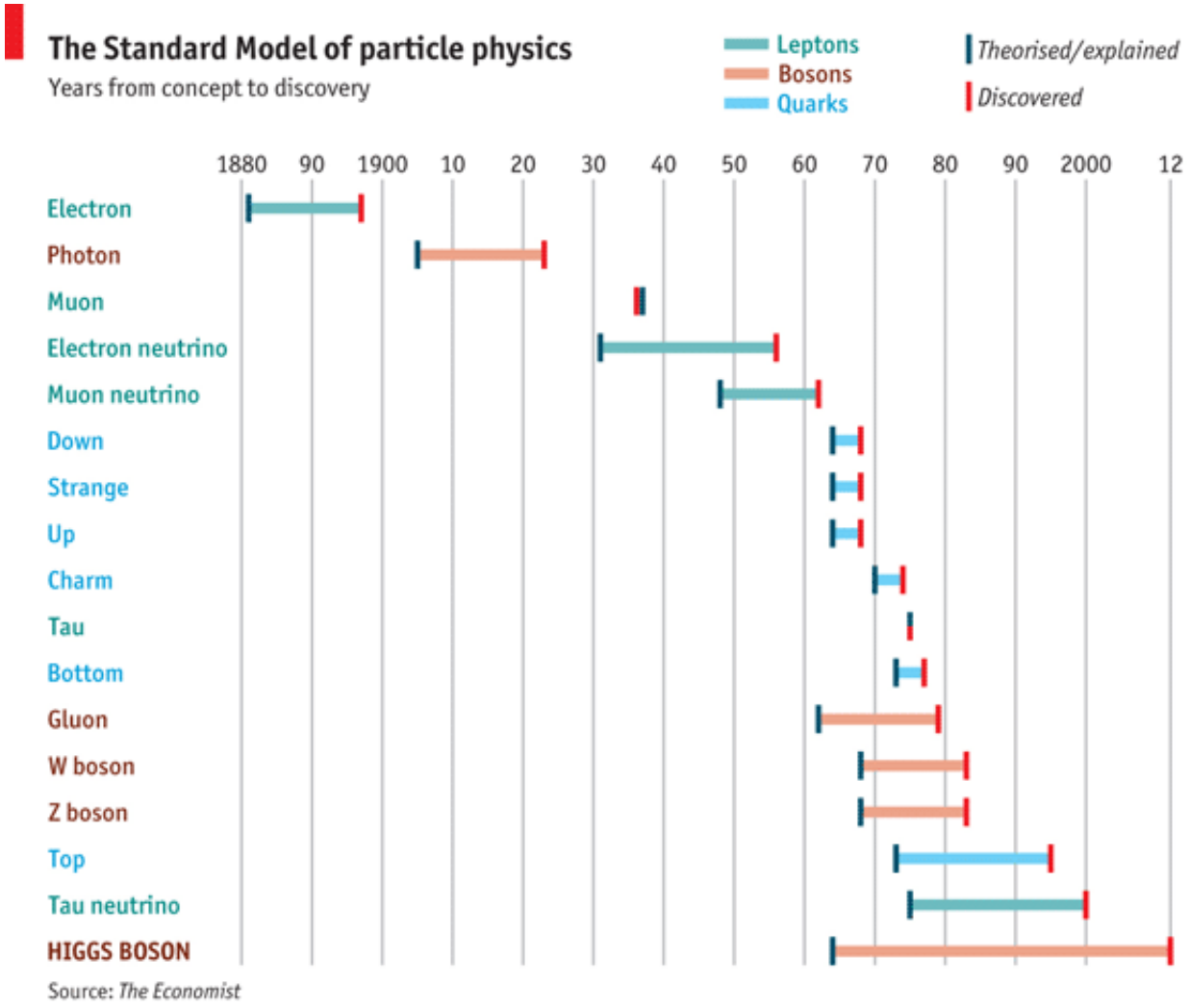

Figure 1.1: Chronology of the discoveries of the Standard Model particles [14].

In the SM approach, there are three different ways through which the scalar, the vector and the spinor elementary particles can get their respective masses. But they all share the same characteristic of being related to a specific kind of interaction with the Higgs field. In fact, to generate masses we need the $\Phi^4(x)$ self interaction for the scalar particle, the minimal gauge coupling interaction for the gauge vector particles and the Yukawa interaction for the spinor particles. Furthermore, we always take profit from the fact the Higgs is currently living around one of its minima states due to a spontaneous broken symmetry driven by the cooling down of the universe temperature. This break in symmetry brought the ground state of elementary particles from underlying to the $SU_c(3) \otimes SU_{I_W}(2) \otimes U_Y(1)$ gauge group, to appear as state of the $SU_c(3) \otimes U_{em}(1)$ gauge group. Hence, color and electromagnetic symmetries are the current residual symmetries of states in our universe. Yet, the Lagrangian $\mathcal{L}_{SM}$ still being governed by the $SU_c(3) \otimes SU_{I_W}(2) \otimes U_Y(1)$ gauge symmetry.

1.1.1 Generation of the scalar Higgs boson mass (Goldstone mechanism)

In the SM, we assume that the Higgs field $\Phi(x)$ is a complex scalar Klein Gordon field with respect to Lorentz group, a doublet under the weak isospin non abelian group $SU_{I_W}(2)$, a singlet under the non abelian color group $SU_c(3)$ with no color charge, and a singlet under the abelian hypercharge group $U_Y(1)$ with hypercharge value $Y_{(\Phi)} = 1$.

Hence, we can write:

$$\Phi(x) = \begin{pmatrix} \phi^{(+)}(x) \\ \phi^{(0)}(x) \end{pmatrix} = \begin{pmatrix} \phi_1(x) + i\phi_2(x) \\ \phi_3(x) + i\phi_4(x) \end{pmatrix} \tag{1.1}$$

This field is subject to the following Lagrangian $\mathcal{L}_S$ with a Φ^4 self interaction.

$$\mathcal{L}_S = (D_\mu \Phi)^\dagger (D^\mu \Phi) - V(|\Phi|^2) \tag{1.2}$$

Where D_μ denotes the covariant derivative:[1]

$$D_\mu = \partial_\mu - ig \sum_{k=1}^{3} \frac{\hat{\sigma}_k}{2} W_\mu^k(x) - ig' \frac{Y}{2} B_\mu(x). \tag{1.3}$$

And $V(|\Phi|^2)$ is the Higgs potential energy:

$$V(|\Phi|^2) = \mu^2 \Phi^\dagger \Phi + \lambda (\Phi^\dagger \Phi)^2 = \mu^2 |\Phi|^2 + \lambda |\Phi|^4 \tag{1.4}$$

which, for the free parameters μ^2 and λ chosen as $\mu^2 < 0$ and $\lambda > 0$, can be depicted as in the Figure 1.2.

This potential has an infinite number of possible stable minima (vacuum states)[2] corresponding to:

$$|\Phi|^2_{(min)} = \left(\phi_1^2 + \phi_2^2 + \phi_3^2 + \phi_4^2\right)_{(min)} = \frac{1}{2}\left(\frac{-\mu^2}{\lambda}\right) \equiv \frac{1}{2}\upsilon^2 \tag{1.5}$$

Hence, when the universe cooled down, the Higgs state falls into a specific stable vacuum state (amounting to a choice of a non observable phase factor). So without loss of generality, we can choose this Higgs minimum state as being:

[1] Where σ_k stands for the Pauli matrices, $W_\mu^k(x)$ stands for the three quadri-vector fields belonging to the adjoint representation of the $SU_{I_W}(2)$ group with the corresponding coupling constant g, and $B_\mu(x)$ stands for the quadri-vector field belonging to the adjoint representation of the $U_Y(1)$ group with the corresponding coupling constant g'.

[2] States for which: $V'(|\Phi|^2)|_{|\Phi|^2=|\Phi|^2_{(min)}} = 0$ and $V''(|\Phi|^2)|_{|\Phi|^2=|\Phi|^2_{(min)}} > 0$

$$\Phi_0 = \frac{1}{\sqrt{2}} \begin{pmatrix} 0 \\ v \end{pmatrix} \tag{1.6}$$

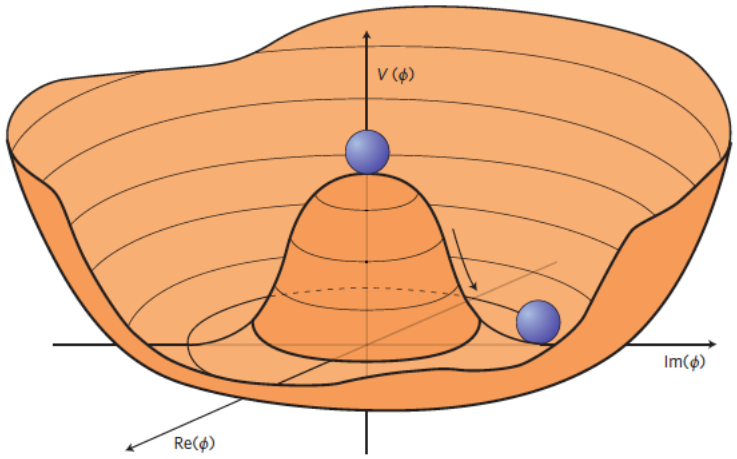

Figure 1.2: Illustration of the shape of the Higgs potential $V(|\Phi|^2)$ for $\mu^2 < 0$ and $\lambda > 0$ [15].

Here, it is worthwhile to note that the Lagrangian $\mathcal{L}_S$ is invariant under the gauge transformations of the $SU_{I_W}(2) \otimes U_Y(1)$ group but not the vacuum Φ_0.

In fact, the scalar field Φ and the gauge fields B^μ and W_k^μ are subject to the following gauge transformations simultaneously:

$$\begin{cases} \Phi(x) \to \Phi'(x) = exp\left\{ \dfrac{i}{2} \left(\displaystyle\sum_{k=1}^{3} \theta_k(x)\, \sigma^k + \varphi(x)\, Y \right) \right\} \Phi(x), \\ \\ B^\mu(x) \to B'^\mu(x) = B^\mu(x) - \dfrac{1}{g'} \partial^\mu \varphi(x) \\ \\ W_k^\mu(x) \longrightarrow W'^\mu_k(x) = W_k^\mu(x) - \dfrac{1}{g} \partial^\mu \theta_k(x) + \varepsilon_{kln}\, \theta^l(x)\, W^{\mu,n}(x) \end{cases} \tag{1.7}$$

This leads to:

$$\begin{aligned} & D^\mu\, \Phi(x) \longrightarrow D'^\mu\, \Phi'(x) \\ & = \left[\partial_\mu - ig \sum_{k=1}^{3} \frac{\hat{\sigma}^k}{2} W_k'^\mu(x) - ig' \frac{Y}{2} B'^\mu(x) \right] exp\left\{ \frac{i}{2} \left(\sum_{k=1}^{3} \theta_k(x)\, \sigma^k + \varphi(x)\, Y \right) \right\} \Phi(x) \\ & = exp\left\{ \frac{i}{2} \left(\sum_{k=1}^{3} \theta_k(x)\, \sigma^k + \varphi(x)\, Y \right) \right\} \left[\partial_\mu - ig \sum_{k=1}^{3} \frac{\hat{\sigma}^k}{2} W_k^\mu(x) - ig' \frac{Y}{2} B^\mu(x) \right] \Phi(x) = D^\mu\, \Phi(x) \end{aligned} \tag{1.8}$$

Hence:

$$\mathcal{L}'_S = \left[D'_\mu \Phi'(x)\right]^\dagger \left[D'^\mu \Phi'(x)\right] - V(|\Phi'(x)|^2) = \mathcal{L}_S \tag{1.9}$$

is gauge invariant.

But the Higgs vacuum state transforms as:

$$\begin{aligned}
\Phi_0 \longrightarrow \Phi'_0 &= exp\left\{\frac{i}{2}\left(\sum_{k=1}^{3}\theta_k(x)\,\sigma^k + \varphi(x)\,Y\,\mathbb{1}\right)\right\}\Phi_0 \\
&\simeq \left\{\mathbb{1} + \frac{i}{2}\left(\sum_{k=1}^{3}\theta_k(x)\,\sigma^k + \varphi(x)\,\mathbb{1}\right)\right\}\Phi_0 \\
&= \Phi_0 + \left\{\frac{i}{2}\left(\sum_{k=1}^{3}\theta_k(x)\,\sigma^k + \varphi(x)\,\mathbb{1}\right)\right\}\Phi_0 \\
&= \Phi_0 + \frac{i}{2\sqrt{2}}\begin{pmatrix}\varphi(x)+\theta_3(x) & \theta_1(x)-i\theta_2(x)\\ \theta_1(x)+i\theta_2(x) & \varphi(x)-\theta_3(x)\end{pmatrix}\begin{pmatrix}0\\ \upsilon\end{pmatrix} \\
&= \left(1+\frac{i}{2}[\varphi(x)-\theta_3(x)]\right)\Phi_0 + \frac{i}{2\sqrt{2}}[\theta_1(x)-i\theta_2(x)]\begin{pmatrix}\upsilon\\ 0\end{pmatrix} \\
&\neq \Phi_0
\end{aligned} \tag{1.10}$$

Which means that the vaccum Φ_0 is not invariant under the gauge group $SU_{I_W}(2)\otimes U_Y(1)$. Besides, it is invariant under a new gauge group. In fact, if we consider just the third component of the weak isospin, and combine it with the hypercharge in a way that forces the relation $\theta_3(x) = \phi(x) \equiv \theta(x)$, then we get:

$$\begin{aligned}
\Phi_0 \longrightarrow \tilde{\Phi}_0 &= exp\left\{\frac{i}{2}\theta(x)\left(\sigma^3 + \mathbb{1}\right)\right\}\Phi_0 = exp\left\{i\theta(x)\begin{pmatrix}1 & 0\\ 0 & 0\end{pmatrix}\right\}\Phi_0 \\
&\simeq \begin{pmatrix}1+i\theta(x) & 0\\ 0 & 1\end{pmatrix}\Phi_0 = \frac{1}{\sqrt{2}}\begin{pmatrix}1+i\theta(x) & 0\\ 0 & 1\end{pmatrix}\begin{pmatrix}0\\ \upsilon\end{pmatrix} = \frac{1}{\sqrt{2}}\begin{pmatrix}0\\ \upsilon\end{pmatrix} \\
&= \Phi_0
\end{aligned}$$

This leads us to the $U_{em}(1)$ group for which the electromagnetic charge Q should be given by the Gell-Man formula: $Q = I_{W_3} + Y/2$.

• Fluctuations around the vacuum

Let us now consider that the Higgs field undergoes small fluctuations around the vacuum Φ_0. We can then parametrize it as follows:

$$\Phi(x) = \frac{1}{\sqrt{2}}\begin{pmatrix}\chi_2(x)+i\chi_1(x)\\ \upsilon + H(x) - i\chi_3(x)\end{pmatrix} = \frac{1}{\sqrt{2}}\,exp\left(\frac{\vec{\sigma}.\vec{\chi}(x)}{\upsilon}\right)\begin{pmatrix}0\\ \upsilon + H(x)\end{pmatrix} \tag{1.11}$$

Then by applying the $exp\left(-\frac{\vec{\sigma}.\vec{\chi}(x)}{\upsilon}\right)$ gauge transformation to the field $\Phi(x)$, we get:

$$exp\left(-\frac{\vec{\sigma}.\vec{\chi}(x)}{\upsilon}\right)\Phi(x) = \frac{1}{\sqrt{2}}\begin{pmatrix}0\\ \upsilon + H(x)\end{pmatrix} \tag{1.12}$$

We see that by this trick, all the fluctuations $\chi_1(x)$, $\chi_2(x)$, $\chi_3(x)$ have been ruled out. Then those are unphysical fields named Goldstone fields. The only remaining physical field is the truly Higgs field $H(x)$. So if we stick only with the physical field, we are allowed to write:

$$\Phi(x) = \frac{1}{\sqrt{2}}\begin{pmatrix}0\\ \upsilon + H(x)\end{pmatrix} \tag{1.13}$$

We are now interested in the mass of this physical Higgs field. For that, let's replace this expression into the Lagrangian $\mathcal{L}_S$, then pick only the terms that are quadratic in the field $H(x)$.

$$\mathcal{L}_S \to \mathcal{L}_{(H^2)} = \frac{1}{2}\partial^\mu H(x)\partial_\mu H(x) - \frac{1}{2}(\mu^2 + 3\lambda\upsilon^2)H^2(x) \tag{1.14}$$

Then, eliminating the tadpole $\upsilon(\mu^2 + \lambda\upsilon^2)H(x)$ by the imposing constraint $\mu^2 + \lambda\upsilon^2 = 0$, our Higgs Lagrangian in equation (1.14) takes the form:

$$\mathcal{L}_{(H^2)} = \frac{1}{2}\partial^\mu H(x)\partial_\mu H(x) - \frac{1}{2}\overbrace{(-2\mu^2)}^{=M_H^2}H^2(x) \tag{1.15}$$

A simple comparison with the Klein-Gordon Lagrangian enables us to deduce that the mass of the Higgs boson is:

$$M_H = \sqrt{-2\mu^2} = \sqrt{2\lambda}\,\upsilon \tag{1.16}$$

The current corresponding experimental value is [16]:

$$M_H = 125.10(14)\,GeV \tag{1.17}$$

Besides, the value of υ deduced from muon decay experiment is [16]:

$$\upsilon = \sqrt{1/(\sqrt{2}\,G_F)} = 246.219651(64)\,GeV \qquad \text{with:} \quad G_F = 1.1663787(6)\,10^{-5}\,GeV^{-2} \tag{1.18}$$

This allows us to deduce the numerical value of the quartic Higgs self coupling as being:

$$\lambda = \frac{M_H^2}{2\,\upsilon^2} = 0.12907(29) \tag{1.19}$$

which is of the same order as the strong coupling [16] $\alpha_s(M_Z) = 0.1179(10)$.

1.1.2 Generation of the electroweak vector gauge boson masses (Higgs mechanism)

Now let us consider the electroweak Lagrangian $\mathcal{L}_{EW}$:

$$\mathcal{L}_{EW} = \mathcal{L}_S + \mathcal{L}_G \tag{1.20}$$

where $\mathcal{L}_G$ is given by [3]:

$$\mathcal{L}_G = -\frac{1}{4} W^k_{\mu\nu} W^{k\mu\nu} - \frac{1}{4} B_{\mu\nu} B^{\mu\nu} \tag{1.21}$$

and

$$\begin{cases} W^k_{\mu\nu} = \partial_\mu W^k_\nu - \partial_\nu W^k_\mu + g\, \varepsilon^{klm} W^l_\mu W^m_\nu \\ \\ B_{\mu\nu} = \partial_\mu B_\nu - \partial_\nu B_\mu \end{cases} \tag{1.22}$$

In this Lagrangian we replace the Higgs field by the expression (1.13). Then we extract only the quadratic terms in W^k_ν and B_ν and their mixing. After some tedious rearrangements, we can write:

$$\begin{aligned} \mathcal{L}_{EW} \to \mathcal{L}_{W^2} \;=\; & -\frac{1}{2(g^2+g'^2)} \partial_\mu \left(g' W^3_\nu - g B_\nu\right) \partial^\mu \left(g' W^{3\,\nu} - g B^\nu\right) \\ & -\frac{1}{2(g^2+g'^2)} \partial_\mu \left(g W^3_\nu - g' B_\nu\right) \partial^\mu \left(g W^{3\,\nu} - g' B^\nu\right) \\ & -\frac{1}{2} \partial_\mu \left(W^1_\nu - i W^2_\nu\right) \partial^\mu \left(W^{1\,\nu} + i W^{2\,\nu}\right) \\ & +\frac{1}{8} g^2 \upsilon^2 (W^1_\mu + i W^2_\mu)(W^{1\mu} - i W^{2\mu}) \\ & +\frac{1}{8} \upsilon^2 (g W^3_\mu - g' B_\mu)(g W^{3\mu} - g' B^\mu) \end{aligned}$$

Then, by introducing the following transformations [4]:

$$\begin{cases} W^+_\mu = \dfrac{1}{\sqrt{2}}(W^1_\mu - i W^2_\mu) = \dfrac{1}{\sqrt{2}}(W^1_\mu + i W^2_\mu)^\dagger \equiv (W^-_\mu)^\dagger \\ \\ Z_\mu = \dfrac{g W^3_\mu - g' B_\mu}{\sqrt{g^2+g'^2}} \equiv W^3_\mu \cos\theta_W - B_\mu \sin\theta_W \\ \\ A_\mu = \dfrac{g' W^3_\mu - g B_\mu}{\sqrt{g^2+g'^2}} \equiv W^3_\mu \sin\theta_W - B_\mu \cos\theta_W \end{cases} \tag{1.23}$$

[3] W^k_μ and B_μ are real electroweak states.
[4] θ_W is the Weinberg angle.

we obtain:

$$\begin{aligned}\mathcal{L}_{W^2} &= \underbrace{-\frac{1}{2}\partial_\mu A_\nu \partial^\mu A^\nu}_{\text{massless photon}} \underbrace{-\frac{1}{2}\left[\partial_\mu Z_\nu \partial^\mu Z^\nu - \frac{1}{4}\upsilon^2(g^2+g'^2)Z^\mu Z_\mu\right]}_{\text{massive Z weak gauge boson}} \\ &\underbrace{-\frac{1}{2}\left[(\partial_\mu W^-_\nu)^\dagger \partial^\mu W^{-\nu} - \frac{1}{4}g^2\upsilon^2\left(W^{-\mu}\right)^\dagger W^-_\mu\right]}_{\text{massive } W^- \text{ weak gauge boson}} \underbrace{-\frac{1}{2}\left[(\partial_\mu W^+_\nu)^\dagger \partial^\mu W^{+\nu}) - \frac{1}{4}g^2\upsilon^2\left(W^{+\mu}\right)^\dagger W^+_\mu\right]}_{\text{massive } W^+ \text{ weak gauge boson}}\end{aligned} \tag{1.24}$$

Hence, we deduce that the masses of the electroweak gauge bosons are:

$$M_\gamma = 0, \qquad M_Z = \frac{\upsilon}{2}\sqrt{g^2+g'^2}, \qquad \text{and} \qquad M_{W^+} = M_{W^-} \equiv M_W = \frac{1}{2}\upsilon g \tag{1.25}$$

The current experimental values of those masses are [16]:

$$\begin{cases} M_\gamma < 10^{-18}\, eV \\ M_Z = 91.1876(21)\, GeV \\ M_W = 80.379(12)\, GeV \end{cases} \tag{1.26}$$

We can then estimate the values of the electroweak couplings g and g' as [5]:

$$\left.\begin{cases} g = \dfrac{2M_W}{\upsilon} \rightarrow 0.652904(17) \\ g' = \dfrac{2}{\upsilon}\sqrt{M_Z^2 - M_W^2} \rightarrow 0.349790(09) \end{cases}\right\} \Rightarrow e = \frac{gg'}{\sqrt{g^2+g'^2}} \rightarrow 0.30832(04) \simeq \sqrt{4\pi\alpha} \rightarrow 0.30286 \tag{1.27}$$

1.1.3 Generation of the spinor fermion masses (Yukawa mechanism)

In the SM, to be in line with the experimental results concerning the decays of particles, Dirac fermions are classified into three families. Furthermore, for each specific fermionic flavor and with respect to the weak isospin interaction, the left handed chiral particle behaves differently than the right handed chiral one.

Let us now confine ourself in the study of one leptonic family composed of two flavors l_u and l_d. Each one of these flavors can be split into two kinds of particles, left and right handed ones. So we have: $l_u^{(L)}$, $l_u^{(R)}$, $l_d^{(L)}$ and $l_d^{(R)}$. Now with respect to the weak $SU(2)_{I_W}$ gauge group, $l_u^{(L)}$ and $l_d^{(L)}$ live in the same doublet state L_l, while $l_u^{(R)}$ and $l_d^{(R)}$ live in separate singlet states

[5] Where the fine structure coupling $\alpha = \frac{1}{137}$.

$R_{l,u}$ and $R_{l,d}$. This allows us to write:

$$L_l = \begin{pmatrix} l_u^{(L)} \\ l_d^{(L)} \end{pmatrix}, \qquad R_{l,u} = l_u^{(R)}, \qquad R_{l,d} = l_d^{(R)} \tag{1.28}$$

The idea is now to use the Higgs field $\Phi(x)$:

$$\Phi(x) = \frac{1}{\sqrt{2}} \begin{pmatrix} 0 \\ \upsilon + H(x) \end{pmatrix}$$

and its charge conjugate $\Phi_C(x)$:

$$\Phi_C(x) = i\,\sigma_2 \Phi^*(x) = \frac{1}{\sqrt{2}} \begin{pmatrix} \upsilon + H(x) \\ 0 \end{pmatrix} \tag{1.29}$$

to generate a SM gauge invariant Yukawa interaction, involving the scalar and the spinor fields.

For the down type flavor, the corresponding Yukawa Lagrangian reads:

$$\mathcal{L}_{Y,d} = -\lambda_d \left(\bar{L}_l(x) \Phi(x) R_{l,d}(x) + \Phi^\dagger(x) \bar{R}_{l,d}(x) L_l(x) \right) \tag{1.30}$$

And for the up type flavor, the corresponding Yukawa Lagrangian reads:

$$\mathcal{L}_{Y,u} = -\lambda_u \left(\bar{L}_l(x) \Phi_C(x) R_{l,u}(x) + \Phi_C^\dagger(x) \bar{R}_{l,u}(x) L_l(x) \right) \tag{1.31}$$

where λ_d and λ_u are the Yukawa coupling for the down and the up flavors. These Yukawa Lagrangians are then combined with the Dirac fermionic kinetic Lagrangian $\mathcal{L}_F$, that can be written in the form:

$$\mathcal{L}_F \;=\; i\bar{L}_l(x) D_\nu^{(l,L)} \gamma^\nu L_l(x) + i\bar{R}_{l,u}(x) D_\nu^{(l,R)} \gamma^\nu R_{l,u}(x) + i\bar{R}_{l,d}(x) D_\nu^{(l,R)} \gamma^\nu R_{l,d}(x) \tag{1.32}$$

where the covariant derivatives $D_\nu^{(l,L)}$ and $D_\nu^{(l,R)}$ are given by:

$$\begin{cases} D_\nu^{(l,L)} = \partial_\nu - ig \sum_{k=1}^{3} \dfrac{\hat{\sigma}^k}{2} W_\nu^k(x) - ig' \dfrac{Y}{2} B_\nu(x) \\ \\ D_{R,\,\nu}^{l} = \partial_\nu - ig' \dfrac{Y}{2} B_\nu(x) \end{cases} \tag{1.33}$$

After that, we extract from the Lagrangian $\mathcal{L}_F + \mathcal{L}_{Y,d} + \mathcal{L}_{Y,u}$ the quadratic terms in the fermionic

fields $l_d(x)$ and $l_u(x)$. We then end up with two expressions:

$$\begin{cases} \mathcal{L}_{l_d^2} = i\,\bar{l}_d\,(\partial_\nu\gamma^\nu)\,l_d - \dfrac{\lambda_d\,\upsilon}{\sqrt{2}}\,\bar{l}_d\,l_d \\ \\ \mathcal{L}_{l_u^2} = i\,\bar{l}_u\,(\partial_\nu\gamma^\nu)\,l_u - \dfrac{\lambda_u\,\upsilon}{\sqrt{2}}\,\bar{l}_u\,l_u \end{cases} \tag{1.34}$$

Hence, the corresponding masses are:

$$M_d = \frac{\lambda_d\,\upsilon}{\sqrt{2}} \qquad \text{and} \qquad M_u = \frac{\lambda_u\,\upsilon}{\sqrt{2}} \tag{1.35}$$

The current experimental values of the masses of the three generations of fermions in the SM are presented in the Table 1.1. We point out here that the top quark t has the largest Yukawa coupling, with a value nearly equal to unit ($\lambda_t \simeq 1$). This makes the top quark the fermion that interacts the most strongly with the Higgs boson. Hence, this interaction between the Higgs and the top quark can be used as a suitable tool to probe Higgs sectors.

Flavor	**Flavor symbol**	**Observed mass** [16]	**Yukawa coupling** $\simeq$
Electron neutrino	ν_e	$< 1.1\,10^{-6}\,MeV$	$6.32\,10^{-12}$
Muon neutrino	ν_μ	$< 0.19\,MeV$	$1.09\,10^{-6}$
Electron	e	$0.5109989461(31)\,MeV$	$3.34\,10^{-6}$
Up	u	$2.6(4)\,MeV$	$1.49\,10^{-5}$
Down	d	$5.3(4)\,MeV$	$3.04\,10^{-5}$
Tau neutrino	ν_τ	$< 18.2\,MeV$	0.0001
Strange	s	$92.47(69)\,MeV$	0.0005
Muon	μ	$105.6583745(24)\,MeV$	0.0006
Charm	c	$1.27(2)\,GeV$	0.0073
Tau	τ	$1776.86(12)\,MeV$	0.0102
Bottom	b	4.18(3)GeV	0.0240
Top	t	$172.76(30)\,GeV$	0.9923

Table 1.1: Experimental mass values of the Standard Model fermions.

The different experimental values of all the SM particles masses including scalar Higgs boson, fermions and vector bosons are illustrated in the Figure 1.3. This figure highlights the hierarchy structure of these mass values. They range from a value less than $10^{-18}\,eV$ for m_γ,

to the value $\simeq 1.73\,10^{11} eV$ for m_t.

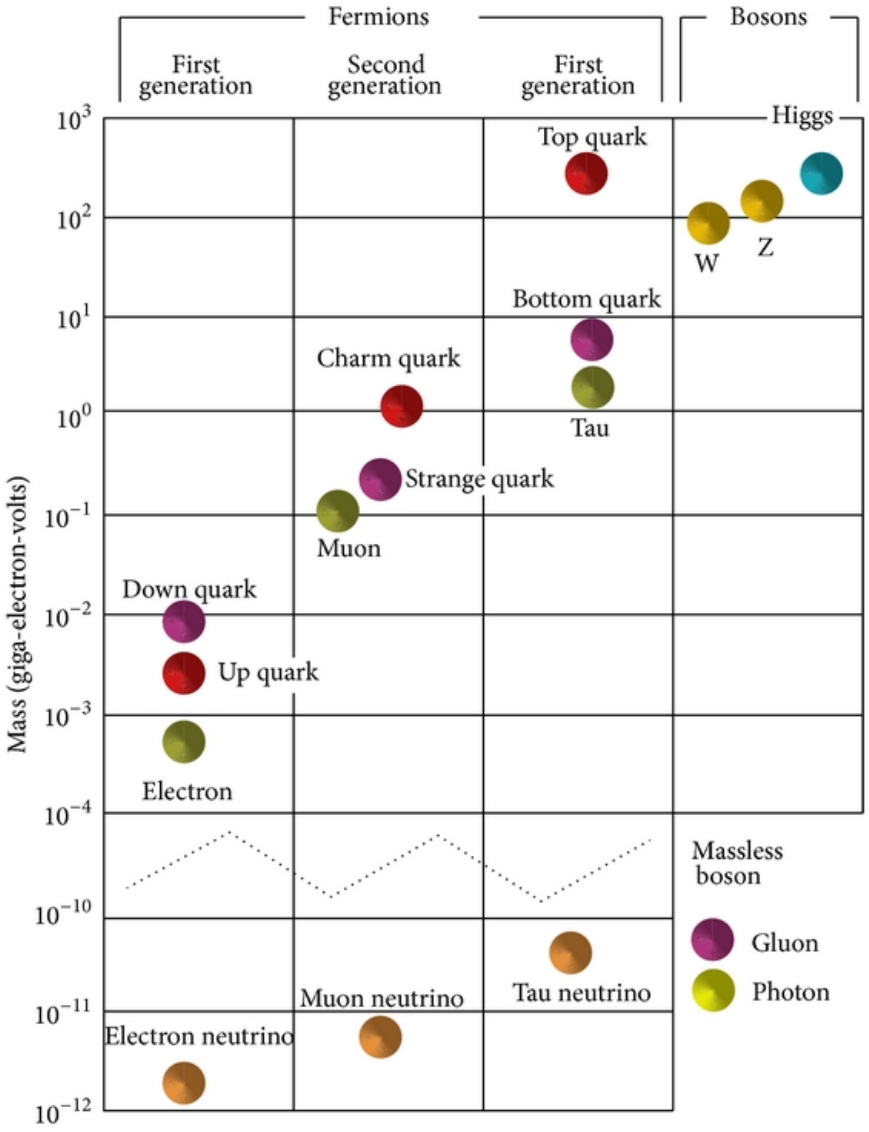

Figure 1.3: Hierarchy distribution of the Standard Model elementary particle masses [17].

1.1.4 SM Feynman rules involving the physical Higgs scalar field

In the SM, the Higgs maintains with the whole physical particle spectrum of the SM, the interactions given by the Feynman rules [18–20] depicted in the Table 1.2. This table enables us to see that, at the leading order (LO), the dominant interactions of the Higgs are first the self interaction, then the interaction with the weak massive gauge bosons and finally the interaction with the top quark. Besides, since the photon and the gluons are massless, there is no interaction of these particles with the Higgs at LO, but at next to leading order (NLO)

through fermionic loops, and also through W weak gauge boson loop for photons.

Interacting fields	**Feynman rule** [18]	**Numerical vertex coupling estimate**
$H - H$	$\frac{1}{(k^2 - M_H^2)}$	/
$H - H - H$	$\frac{3\, e\, M_H^2\, M_Z}{2 M_W \sqrt{M_Z^2 - M_W^2}}$	$196\, GeV$
$Z_\mu - Z_\nu - H$	$\frac{e\, M_Z^3}{M_W \sqrt{M_Z^2 - M_W^2}} g_{\mu\nu}$	$(69\, GeV)\, g_{\mu\nu}$
$W_\mu^+ - W_\nu^- - H$	$\frac{e\, M_W\, M_Z}{\sqrt{M_Z^2 - M_W^2}} g_{\mu\nu}$	$(54\, GeV)\, g_{\mu\nu}$
$\bar{f} - f - H$	$\frac{e\, m_f\, M_Z}{2\, M_W \sqrt{M_Z^2 - M_W^2}}$	0.72 / 0.02 (top/bottom)
$Z_\mu - Z_\nu - H - H$	$\frac{e^2\, M_Z^4}{2\, M_W^2\, (M_Z^2 - M_W^2)} g_{\mu\nu}$	0.29
$W_\mu^+ - W_\nu^- - H - H$	$\frac{e^2\, M_Z^2}{2\, (M_Z^2 - M_W^2)} g_{\mu\nu}$	0.23
$H - H - H - H$	$\frac{-3\, e^2\, M_H^2\, M_Z^2}{2 M_W^2 (M_Z^2 - M_W^2)}$	1.64

Table 1.2: SM Feynman rules involving Higgs. For numerical evaluation we used: $e \equiv e(M_Z) = 0.317$, $M_Z = 91.1876\, GeV$, $M_W = 80.379\, GeV$, $M_H = 125.10\, GeV$, $m_b = 4.18\, GeV$ and $m_t = 172.76\, GeV$ [21].

1.2 How can we produce the Standard Model Higgs boson at the Large Hadron Collider?

At the Large Hadron Collider, we have a hadronic collision between protons accelerated at an energy of about $6.5\, TeV$. At this high energy, each proton is constituted, beside its valence up and down quarks, of a sea of quark and antiquark pairs, as well as a huge amount of gluons. Each frontal hard collision between two protons with quadri-momentum P_1 and P_2 respectively, will essentially involve the collision between two internal partons of quadri-momentum $p_1 = x_1\, P_1$ and $p_2 = x_2\, P_2$; where x_1 and x_2 are fractions of the carried momenta and are varying from 0 to 1. And how likely a given parton i carries a fraction x of the initial

proton's momentum is described by the experimentally deduced parton distribution functions $f_i(x, Q^2)$. For example from CTEQ[6] collaboration [22, 23] or MSTW collaboration [24].

Then here, we are looking for producing the Higgs boson from these partonic collisions. And since the last LEP[7] lower limit on Higgs mass was $114\,GeV$, we are especially interested in hard partonic collisions. On the other hand, we know that the Higgs is mostly interacting with the heavier particles: the top quark, the weak gauge bosons and at a lower level with the bottom quark. So for producing efficiently the Standard Model Higgs boson, we rely especially on processes that involve the top quark, then the bottom quark. We also focus on the processes that are involving the massive weak gauge bosons for their high strength interaction with the Higgs.

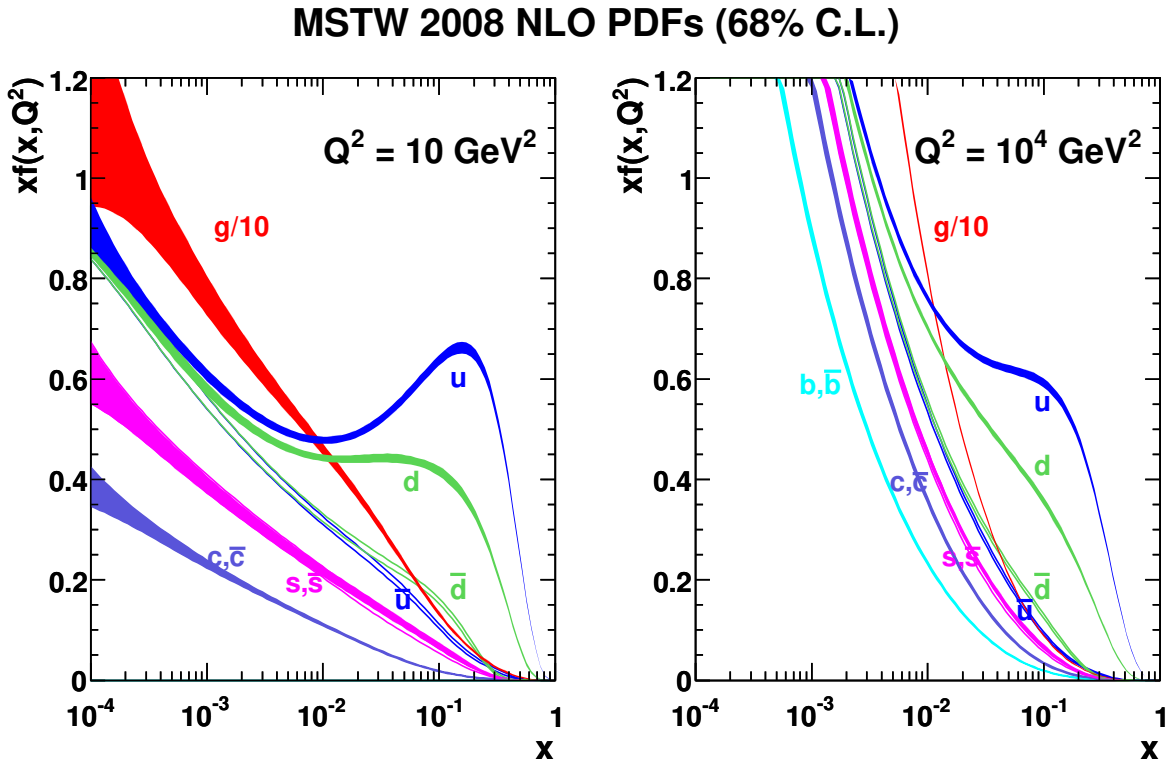

Figure 1.4: Parton density functions for partons inside the proton (MSTW collaboration) [24].

Hence the main production modes of the Higgs boson at LHC, arranged by decreasing order of the cross section, are:

1. **Gluon fusion (ggF):** this is the direct production process of the Higgs via the fusion of two gluons $pp \to gg \to H$. Since the gluon PDFs are largely dominant at the LHC area,

[6]CTEQ: for the **C**oordinated **T**heoretical-**E**xperimental project on **Q**CD.
[7]LEP: for Large Electron Positron collider.

this process is considered the most dominant process at the LHC. It proceeds through a loop of the top quark that has a moslty unit Yukawa coupling.

2. **Vector boson fusion (VBF):** this process can originate from two massive weak gauge bosons $W^{\pm}$ or Z emitted by two quarks. Then those weak gauge bosons annihilate to generate the Higgs boson $pp \to qq \to VVq'q' \to Hq'q'$.

3. **Electroweak boson associated production (WH, ZH):** also called Higgs-strahlung. A quark anti-quark annihilation produces an off-shell vector boson (either a W or Z), which then emits a Higgs boson to return on mass shell $pp \to q\bar{q} \to V^* \to V + H$. (Off-shell means it has an effective mass different from its rest mass).

4. **Pair fusion associated production ($t\bar{t}H$, $b\bar{b}H$):** a top anti-top (or a bottom anti-bottom) quark pair is emitted simultaneously by two gluons. The pair then annihilates to produce a Higgs boson $pp \to ggt\bar{t} \to Ht\bar{t}$. This mode has a cross section of two magnitude orders inferior to the direct production. Thus it's not easily exploitable unless there's a very high luminosity.

The corresponding Feynman diagrams for these Higgs production modes are represented in the Figure 1.5:

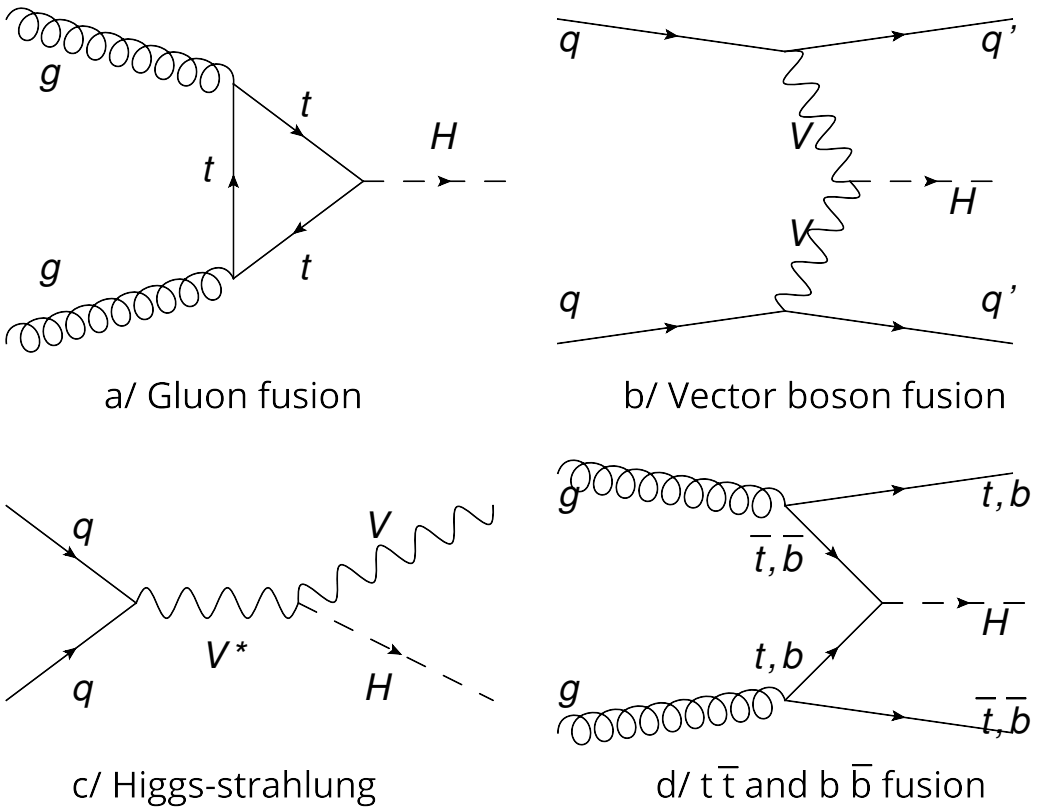

Figure 1.5: Representative Feynman diagrams of the different Higgs production modes at the LHC.

1.3 How does the Standard Model Higgs boson decay?

Taking into account the Standard Model Higgs boson decay rate depicted in the Figure 1.6, we see that for $m_H = 125$ GeV, the Higgs boson decays almost instantaneously. It has an extremely short lifespan of about $\tau_H \sim 10^{-22}s$, since its total decay rate is $\Gamma_H \sim 2\,10^{-3}$ GeV and it should obey the Heisenberg relation $\tau_H \Gamma_H \simeq \hbar$ [8].

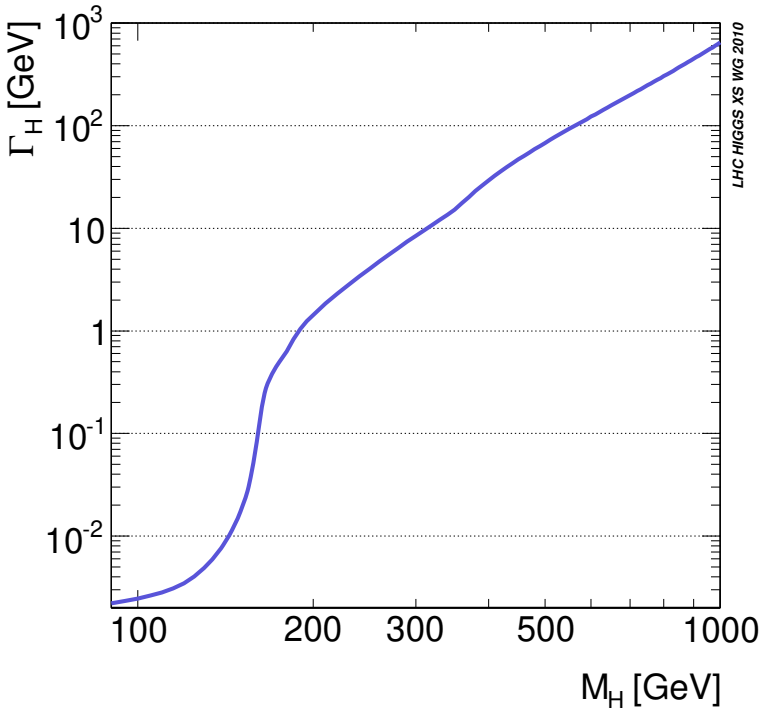

Figure 1.6: The Higgs total decay rate [25].

Since the Higgs boson couples to all the massive particles, the possible decay final states are numerous. We'll resume them in what follows:

1. Decay into a fermion pair:
   - Decay into leptons.
   - Decay into quarks.
2. Decay into gauge bosons:
   - Direct decay into weak bosons.
3. Loop mediated decay into gauge bosons:
   - Decay into two gluons.

[8] $\hbar = 6.582119569...10^{-25}$ GeV.s.

- Decay into two photons.
- Decay into a photon and a Z boson.

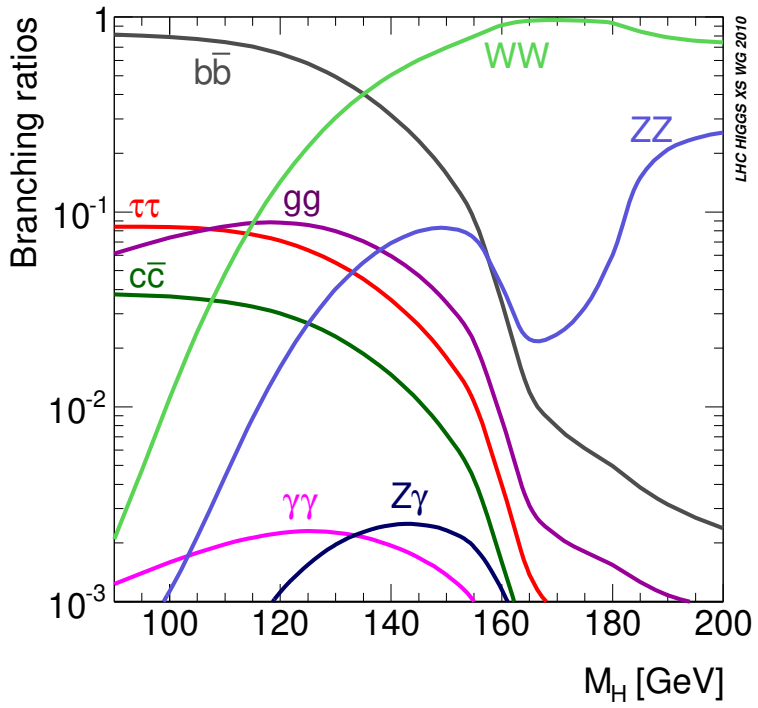

Figure 1.7: Standard Model Higgs boson decay branching ratios [25].

The Higgs boson can thus decay in many different ways, and each decay mode has its own probability of happening. The *branching ratio*, defined as the fraction of the total number of decays following the process, gives an idea of how likely a Higgs boson will decay into one of its decay modes. For example, in around 60% of the time, a Higgs with a mass of 125 GeV will decay to $b\bar{b}$. The Higgs boson branching ratios are shown in the Figure 1.7.

Chapter 2

LHC physics and ATLAS detector

Particle colliders are the most important experimental tool for particle physics nowadays. They show to be pretty useful in confirming and testing theoretical suggestions, be it new or existing theories. In this chapter, we are going to take a closer look at the ATLAS experiment in the Large Hadron Collider, and try to understand the physics involved in the proton proton collision. This chapter is largely inspired from the excellent lecture notes of Schwartz on collider physics [26].

2.1 The Large Hadron Collider

The Large Hadron Collider (LHC) [27] is an underground ring, situated near Geneva, underneath the France-Switzerland border. It consists of a circular tunnel of 27 kilometers in circumference, with a mean depth of 100 meters underground. Its superconducting magnets and accelerating structures can accelerate particles along their way to nearly the speed of light, producing very high energy collisions. It is considered the world's biggest and most powerful particle accelerator of all times. It was built by the CERN (European Organisation for Nuclear Research), with the main objective of discovering the Higgs boson. Its overall aim is to help in answering the fundamental open questions in physics.
The energy density and temperature produced in the collisions at the LHC are similar to how it would've been a few moments after the Big Bang. With this, physicists hope to better understand how the universe evolved.

2.2 Why is the LHC designed the way it is?

To answer this question, we can start by looking for the approximate requirements for discovering a Higgs boson. We'll be using some dimensional analysis and basic Particle Physics.

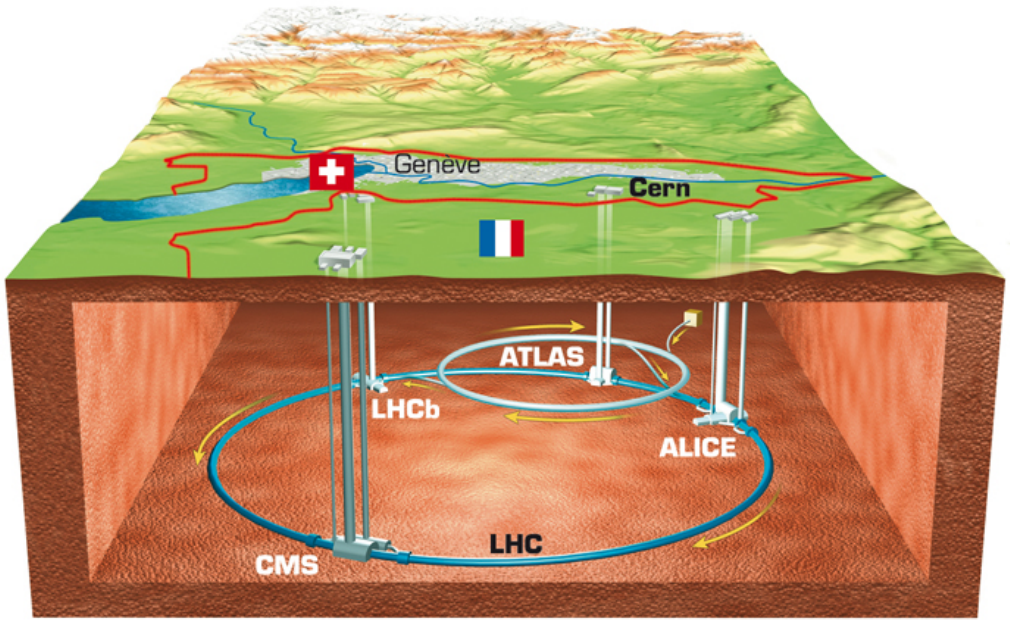

Figure 2.1: Sectional plan of the LHC, with ATLAS, CMS, ALICE and LHCb as detectors locations [28].

Intuitive and rough estimates will be used rather than precision calculations whenever possible to derive results [26].

The base unit for scattering cross sections is the barn (b), and it's defined as: $1\text{b} = 10^{-28}m^2$. We can also define it as the cross section for $n - U^{235}$ scattering (a neutron and a Uranium 235 nucleus), which is $\sim$ 1b. We can notice that cross sections have the same dimensions as an area.

If we want to know the cross section for a proton-proton scattering at the LHC, we can use the fact that a nucleus' volume is proportional to A, the number of its nucleons (protons + neutrons): $V \sim A$ (since we have $V = \frac{4}{3}\pi r^3$). This means that the radius is proportional to $A^{1/3}$: $r \sim A^{1/3}$, which leads to the area of the nucleus scaling like $A^{2/3}$ since it should scale like r^2. Note that from the point of view of scattering, protons and neutrons are pretty much the same (we can't tell the difference between them through the strong interaction). We'll consider both of them as nucleons. So we can write:

$$\sigma(U^{235}, n) \sim 1b$$
$$\sigma(p,p) \sim \frac{\sigma(U^{235}, n)}{A^{2/3}} = \sigma(U^{235}, n).A^{-2/3}$$

And thus, the proton-proton scattering should have a total cross section of: $1 \times 235^{-2/3}b =$

$0.026b \simeq 0.03b$ or $30mb$ in millibarns.
As another way to estimate this, we can use the conversion relation between length and energy. We can derive it from the Planck-Einstein relation [29] as follows:

$$E = h\nu = h\frac{c}{\lambda} = 2\pi\hbar\frac{c}{\lambda}$$
$$\frac{\lambda}{2\pi} = \frac{\hbar c}{E} \Rightarrow \frac{\lambda^2}{4\pi^2} = \frac{\hbar^2 c^2}{E^2} \qquad (m^2)$$

We notice that the left part is a squared length (λ is a wavelength) over radians (no dimension), so the unit is m^2. If we take $E = 1$ GeV then:

$$\frac{1}{GeV^2}\hbar^2 c^2 = 3.895 \times 10^{-32} m^2 \tag{2.1}$$

with the reduced Planck constant $\hbar = 6.58 \times 10^{-25} GeV.s$, light's velocity $c = 3 \times 10^8 m/s$ and $1\,GeV = 10^3 MeV = 10^9 eV$. Considering $1m = 10^{15} fm$ (fm being the femtometer unit), we get the product $\hbar c = 197.32 MeV.fm \simeq 200 MeV.fm$. With this, we can write (2.1) in a way easier to remember and more approximative, taking $\hbar = c = 1$:

$$\frac{1}{fm} \simeq 200MeV, \qquad \text{and} \qquad \frac{1}{GeV^2} \simeq 4 \times 10^{-32} m^2 = 4 \times 10^{-4} b \tag{2.2}$$

It says that the strong interaction scale of Quantum Chromo-Dynamics (QCD), $\Lambda_{QCD} \sim 200MeV$ is the same as the "radius" of the proton $r_p = 0.8fm \sim 1fm$. Which means that the proton scattering cross section area should be roughly: $\sigma \sim \pi r_p^2 \simeq 3fm^2 = 3 \times 10^{-30} m^2 = 0.03b = 30mb$. And thus, it's actually consistent with what we estimated from the $n - U^{235}$ cross section.

This rough number $\sigma \sim 30mb$ is enough to get us started. As an example of a process of interest, let's find the rate for a W boson production. For weak interactions, the typical scale is Fermi's constant G_F:

$$\sigma(pp \to W) \sim G_F \sim \frac{g^2}{M_W^2} \sim \frac{1}{(100GeV)^2} = 10^{-4} GeV^{-2} = 4 \times 10^{-8} b = 40nb$$

So, we can say around 40 in a million proton collisions will produce W boson.
How about a Higgs boson production? The most common production mode for a Higgs particle is, as we've seen in the previous chapter, from gluon fusion in a top loop. The cross section of the Higgs should be down by around a loop factor of $\frac{1}{16\pi^2} \sim 2 \times 10^{-2}$ from weak interaction cross sections that occur at tree level (like W production). We can estimate:

$$\sigma(pp \to H) \sim (loop) \simeq 10^{-2} \times \sigma(pp \to W) \sim 10^{-11} b = 10pb$$

And so, in order to produce 10 Higgs, we'll need about 1 billion proton collisions.

Let's now talk about luminosity, which is the collision rate at the LHC. What kind of luminosity will be needed in order to obtain good results in a reasonable amount of time? Let's take an example: consider we want to observe 100 Higgs bosons in a year. Let's say we look at $H \longrightarrow \gamma\gamma$ decay mode, it has a 10^{-3} branching ratio. Taking experimental efficiencies into consideration, at about $\varepsilon \sim 10^{-2}$ level:

$$\frac{10^9 collisions}{1 Higgs} \times \frac{10^3 Higgs}{H \longrightarrow \gamma\gamma} \times \frac{1}{10^{-2} eff.} \times \frac{100 H \longrightarrow \gamma\gamma}{year} \times \frac{year}{10^7 s} = 10^9 collisions/s = 1 GHz$$

So in order to see 100 Higgs produced in a year, we'll have to collide 1 billion protons per second. How do we do that concretely?

Protons are separated into bunches at the LHC. These bunches move around the tunnel at nearly the speed of light, with around 25 ns ($\sim$ 8 meters) between each group. This spacing means that bunches collide at a 40 MHz frequency. So to obtain a GHz rate, we need around 25 collisions everytime bunches cross each other. This is achieved at the LHC by squeezing the bunches to a spot size of around 10 microns (10^{-6} m) across at the crossing point. With a number of 10^{11} protons per bunch, the collision number per bunch crossing becomes:

$$N_{events} = (10^{11} protons/bunch)^2 . \frac{\sigma_{pp} = 10mb}{\sigma_{beam} = (10\mu m)^2} = 100\, collisions/bunchcrossing$$

Which gives us a total collision rate of 4 GHz.
Regarding the accelerating part, in order to accelerate a particle to a wanted energy, we make use of its electromagnetic properties. A charged particle can thus be accelerated with electric fields E, whereas magnetic fields B are used to control its trajectory. A magnetic field perpendicular to the particles' velocity allows to maintain them in a circular trajectory. Quadrupolar magnets (and sometimes sextupolar) keep the charged particles beam concentrated, otherwise the beam would tend to get dispersed since it consists of particles that have the same electric charge sign. At the LHC, the collision rate we talked about is called **the luminosity**. Instantaneous luminosity is what you integrate over time to get the integrated luminosity. The instantaneous luminosity of the LHC is currently: $L = 10Hz/nb = 10^{34} cm^{-2}.s^{-1}$. If we multiply by the pp cross section: $L \times 10mb = 10^8 Hz = 0.1 GHz$.

So, this is roughly what we need for Higgs physics. To hunt for possible exotic Beyond Standard Model physics particles, we'll most likely have to increase the instantaneous luminosity considerably.

2.3 Particle detection

Detectors help identify and measure the characteristics of particles contributing in a reaction. After taking a look at the physics involved in the making of these devices, we'll proceed to describe the LHC's ATLAS detector.

2.3.1 Detector physics

In order to have a detection, there has to be an interaction. The big majority of detectors are based on the electromagnetic interactions of particles with matter. That's why, with only some few exceptions, only the charged particles are detected directly. Although photons are neutral, they manifest themselves by their interactions with charged particles. Other neutral particles have no electromagnetic interaction. They can only be "seen" following collisions, decays or any other process that produces secondary charged particles [30].

Ionisation

Ionisation is the most common process contributing in the detection. When a charged particle is in motion, its electromagnetic field accelerates the electrons of atoms close to its trajectory and thus ionizes them. The ion can then be detected either chemically or electrically. During the process, the charged particle continues in its trajectory but some of its energy is absorbed by the medium. The theory allows to predict with precision the amount of these losses, largely due to Coulomb scattering by atomic electrons (this is different from Coulomb scattering with nuclei).
The Bethe-Bloch formula expresses the mean energy loss per distance travelled x:

$$-\frac{dE}{dx} = \frac{DZ^2 n_e}{v^2}\left[ln\left(\frac{2mv^2\gamma^2}{I}\right) - v^2 - \frac{\delta}{2}\right] \tag{2.3}$$

where m is the mass, Z the charge and v the velocity of the particle (we consider $\hbar = c = 1$). $\gamma = (1-v^2)^{-1/2}$ is the Lorentz factor. The constant D is: $D = \frac{4\pi\alpha_{em}}{m}$, whereas I is the mean ionisation potential. δ is a factor for the electric-field screening and adds a correction due to the medium's density. As for n_e, it's the electronic density of the medium.
A good knowledge about the ionised medium allows to determine the velocity and charge of the charged particle.

Coulomb scattering

The charged particle can also interact with heavy nuclei electromagnetically through Coulomb scattering. This process is characterized by:

- A motionless target (or almost).
- A transverse scattering or a considerable scattering angle.
- An elastic or quasi-elastic collision (conservation of the energy).

Bremsstrahlung radiation

In this process, the particle-nucleus collision is accompanied with the emission of a photon and thus is different from Coulomb diffusion with its inelasticity.

$$-\frac{dE}{dx} = \frac{E}{\lambda} \tag{2.4}$$

where λ is the wavelength of the radiation:

$$\lambda^{-1} = 4\frac{Z(Z+1)}{m^2}\alpha_{em}^3 n_a ln\left(\frac{183}{Z^{1/3}}\right)$$

with n_a being the atomic density and the other quantities already mentioned above.
Unlike the ionisation, the bremsstrahlung radiation is strongly dependent on the mass of the charged particle ($\propto$ (mass)$^{-2}$), so it will be dominant for small mass particles (electrons and positrons).

Photons absorption

Photons have a high probability of being absorbed or scattered by atoms in a material, to more or less big angles depending on their energy. The density $\mathcal{I}$ of monochromatic (same wavelngth) photons of a beam (or a beam's intensity) varies according to:

$$\frac{d\mathcal{I}}{dx} = -\frac{\mathcal{I}}{l} \tag{2.5}$$

where $l = \frac{1}{n_a \sigma_\gamma}$ is the mean free path. By integrating the last equation we get:

$$\mathcal{I}(x) = \mathcal{I}(x_0)e^{-(x-x_0)/l} \tag{2.6}$$

which indicates an exponential decrease of the beam's intensity in terms of the distance from the atom. Photons' absorption by matter goes through three processes that contribute all to the total cross section σ_γ:
Photoelectric effect

An absorbed photon emits an electron from more or less deep electron shells. The absorption spectrum of the medium depends on the energy of the photons but it's mostly characterized

by peaks corresponding to the binding energies of the electrons.

Compton effect

The Compton effect describes the scattering of a photon by matter. This process is inelastic.

Pair production

Beyond a certain energy threshold $E = 2m_e c^2$, the photons can induce the creation of a particle-antiparticle pair with both m_e as their masses, in presence of an external field. There are two distinct contributions to the cross section: the first is where the external field is that of the atomic electrons, and the second is where the photons interact with the field of the nucleus. At very high energy, the creation of pairs overshadows the photoelectric and Compton effects in the expression of the total cross section σ_γ.

2.3.2 The ATLAS detector

The two main multi-purpose detectors at the LHC are ATLAS (A Toroidal LHC ApparatuS) and CMS (Compact Muon Solenoid). They both have the same basic design. We are more interested in the ATLAS detector since our study will use data from the ATLAS experiment.

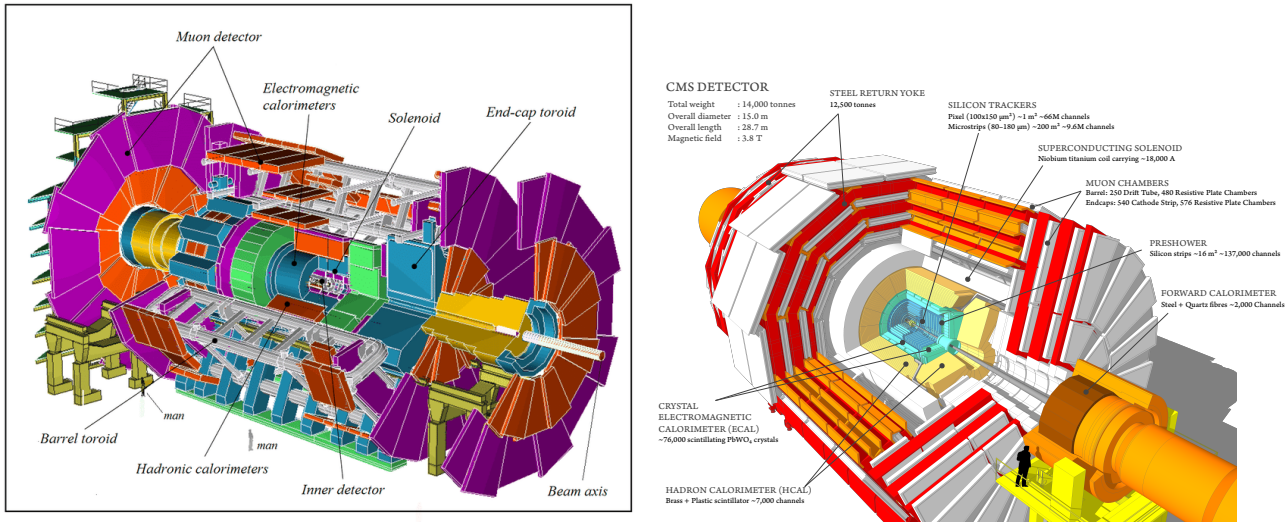

(ATLAS) (CMS)

Figure 2.2: Overview of the ATLAS and CMS detectors at the LHC [31] [32].

The ATLAS detector is a huge cylindrical shaped device, centered around the Interaction Point (IP). It is currently the largest particle detector on earth, with 44 meters long and 25 meters height, weighing around 7000 tons.

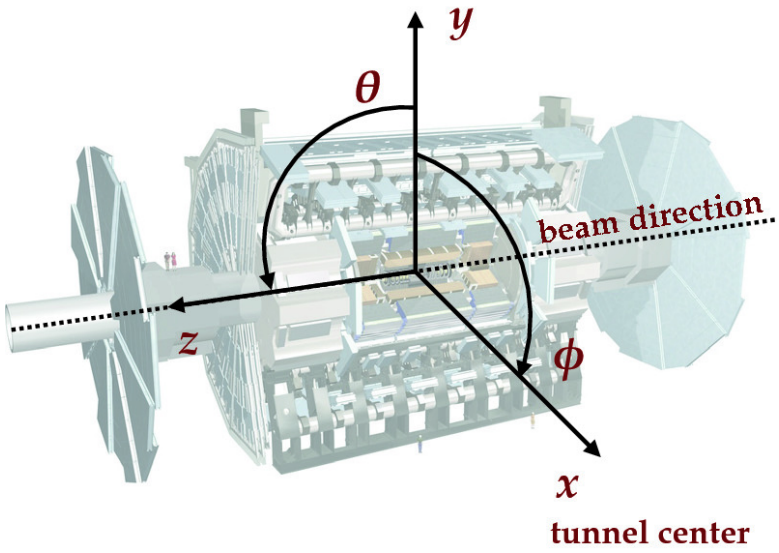

Figure 2.3: The coordinate system in the ATLAS detector [33].

Coordinate system

The coordinate system used in the ATLAS experiment is a right-handed Cartesian frame, defined with the z-axis along the beam direction, the x-axis pointing towards the center of the LHC tunnel and the y-axis pointing upwards. The x-y plane is the transverse plane in accordance with the z-axis i.e. transverse to the beam direction.
Considering the detector's geometry and symmetry around the z-axis, equivalent cylindrical coordinates are generally employed (as shown in the Figure 2.3). A charged particle is characterized by its momentum with the set (p_T, θ, ϕ), where:

- ϕ is the azimuthal angle, measured around the beam axis in the x-y plane.

- θ is the polar angle, measured from the beam axis.

- p_T is the transverse momentum, which is the component of the three-momentum on the transverse plane x-y: $p_T = \sqrt{p_x^2 + p_y^2}$.

The *pseudorapidity* η, defined as: $\eta = -\ln \tan \frac{\theta}{2}$, is usually used instead of the polar angle θ. And the quantity: $\Delta R = \sqrt{(\Delta\eta)^2 + (\Delta\phi)^2}$, is also used to express the distance between two trajectories. We'll discuss the choice of these variables later in this chapter.

Detector components

In a proton-proton collision, transverse sprays of resulting particles will flow from the crossing point of LHC beams through the different components of the detector. Organized from the inside to the outside, the main components of the ATLAS detector are:

- **Inner Detector (ID):** or tracker, to track the trajectory of charged particles and bend it through a magnetic field, in order to measure the momenta. It is divided into three dif-

ferent parts. The region around the beam line consists of silicon pixel detectors. Outside is a silicon semiconductor tracker, followed by a transition radiation tracker.

- **Electromagnetic Calorimeter (ECal):** to measure energies of electrons and photons. It is made of liquid argon.
- **Hadronic Calorimeter (HCal):** to measure energies of protons and neutrons, and provide a good reconstruction of jets and missing transverse energy. It is made of plastic scintillator tiles and iron.
- **Muon Spectrometer (MS):** to measure muons tracks based on their magnetic deflection in large superconducting magnets. It contributes greatly in the large size of the detector.

The Figure 2.4 represents the different components of the ATLAS detector, and shows how different particles appear and interact with them so that they are reconstructed and identified.

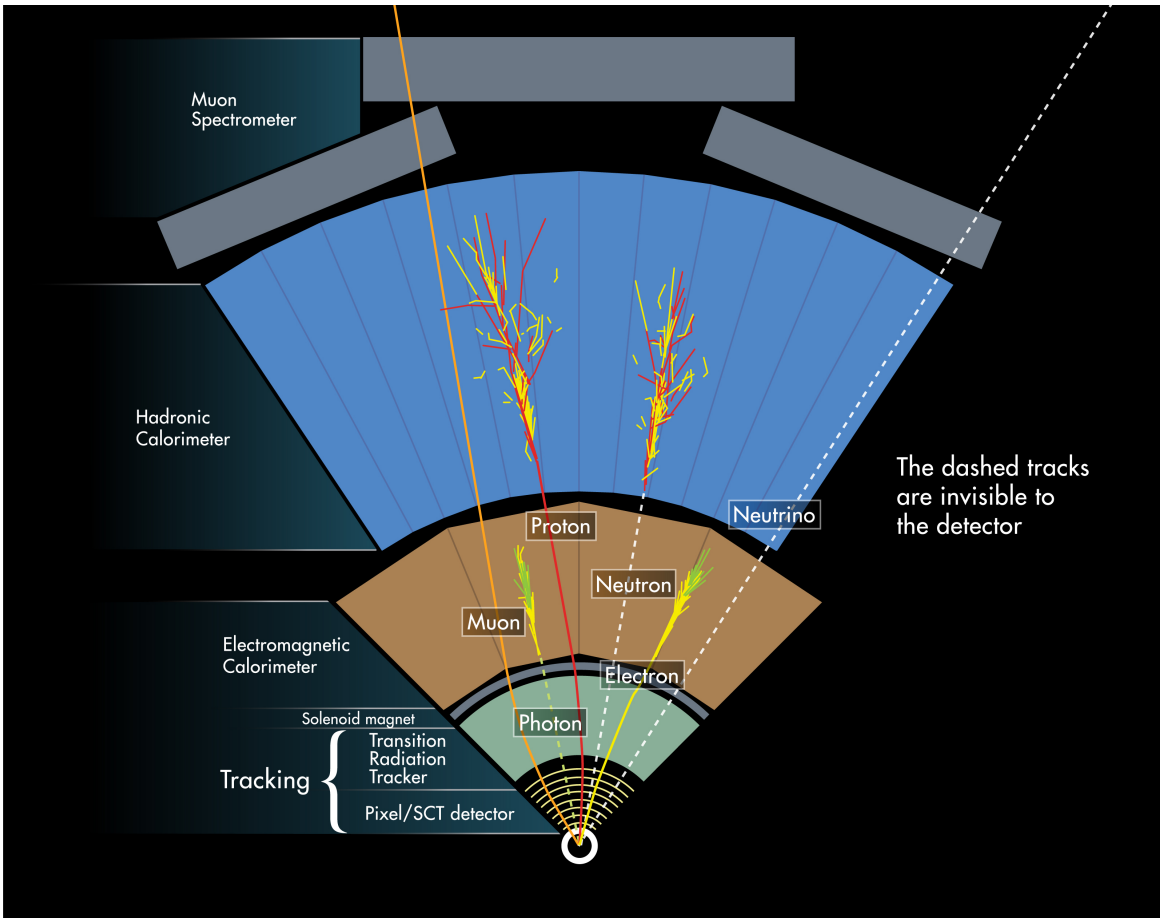

Figure 2.4: Sectional plan of the ATLAS detector showcasing its different components and tracks left by different particles [34].

1. **Electron :** will flow through the inner detector leaving a track behind, before finally stopping in the electromagnetic calorimeter.

2. **Photon :** behaves in a similar way but leaves no track.

3. **Proton :** leaves a track and interacts primarily in the hadronic calorimeter.

4. **Neutron :** behaves in a similar way but leaves no track.

5. **Muon :** passes all the way through ATLAS leaving tracks behind.

6. **Neutrino :** passes through ATLAS without being detected at all.

2.4 Triggering and data acquisition

At the LHC, ATLAS is designed to observe up to 1.7 billion events per second, let's say approximately 1 billion. A rate in GHz is also the order of speed of computer processors nowadays. A computer with a Central Processing Unit (CPU) of 1 GHz means it can make around 1 billion operations every second. One collision event at the LHC fills up around 1 MB of storage space. It is obviously impossible to save all 1 billion events on disk every second. But we also know that only some of these events will contain interesting characteristics, potentially leading to new discoveries. So rather than that, current electronics have the capacity of recording 200 MB/s. So, in order to be recorded and analysed, the 10^9 events need to be filtered and reduced to select around 1000 events only. This is where the **triggering system** takes place; where the data acquisition system directs the data from the detectors to storage. Triggers are a set of criteria and conditions that decide if an event is interesting enough and worth recording or not to disk for physics analyses. Thus it reduces the flow of data into manageable amounts. They are regularly updated and modified to get optimised results or depending on the objectives. The triggering process is extremely crucial to collider experiments; if an important event escapes a trigger, it is forever lost [26].

The online event selection process of the ATLAS triggering system follows two stages [35]:

1. **The Level-1 hardware trigger :** composed of custom-made electronics. Works on data from the calorimeter and muon detectors. After the event occurs, the decision to keep its data is made in less than 2.5 microseconds. The Level-1 trigger can collect around 100,000 events per second at most for the High-Level Trigger (HLT).

2. **The High-Level Trigger (HLT):** software based trigger, consisting of a large farm of CPUs. It improves the analysis of the hardware based Level-1 trigger. It manages a very detailed analysis, either with:

- An overall examination of the event for selected detector components (like calorimeters, trackers or muon detectors).
- Or by using data in smaller and isolated regions of the detector.

The HLT analysis selects about 1000 events per second. They are fully collected into an event record. These events data are saved with a data storage system for offline analysis.

2.5 Kinematics

We have two protons coming in towards each other in opposite directions, each taken to be in the z direction by convention. Let's study the kinematics of this collision at very high center-of-mass energy, by taking it for example at the 13 TeV LHC [26].
Protons are accelerated to nearly the speed of light, with both a momenta of 6.5 TeV. So we write the four momenta as:

$$P^\mu = (P^0, P^1, P^2, P^3) = (\frac{E}{c}, P_x, P_y, P_z)$$

$$P_1^\mu = (6.5,\ 0,\ 0,\ 6.5) \qquad P_2^\mu = (6.5,\ 0,\ 0,\ -6.5) \qquad \text{(TeV)} \tag{2.7}$$

Everytime protons collide, we can say that it's their constituents that are colliding. There are three valence quarks in a proton (two up and one down *uud*), and they're all binded together by gluons. We can also find virtual particles (like a pair of a particle and its anti-particle) that can appear at higher energies in the collision. These constituents are called *partons*.
If we collide two beams of protons together, most of the time, nothing big happens and there's scattering of constituents that carry a negligible fraction of the proton's energy. But sometimes, there's a probability to get a hard quark-gluon scattering. Where the particles involved carry a significant fraction of the protons' energy, giving a significant amount of particles produced, heading at transverse directions to the beams. It is this kind of collisions that we're the most interested in observing and analysing: **the hard processes**.
When we have a hard process, the parton momenta are written as:

$$p_1^\mu = x_1 P_1^\mu \qquad p_2^\mu = x_2 P_2^\mu \tag{2.8}$$

x_1 and x_2 represent the fraction of the proton's momenta for the partons.
According to the parton model [36], momentum fractions x_1 and x_2 are independent. The probability of finding x_1 in the first proton doesn't depend on what happens in the second one. The key to being able to calculate anything at all at the LHC using the perturbation theory is factorization, and this independence is an example of it.

Let's say these two partons of p_1 and p_2 as momentum enter a high energy collision and

produce a Z boson which then gives an e^+/e^- pair as decay result. The angular separation between these produced leptons can be interesting. The **azimuthal angle** ϕ can be measured around the beam line cylinder in the transverse plane, as well as the **polar angle** θ measured from the beam axis. If $(p_1 + p_2)^2 = m_Z^2$, the Z is created at rest in the partonic center-of-mass frame. Whereas it is not at rest in the lab frame, since $p_1 + p_2$ can have some net z-momentum p_z. The lepton pair will be back-to-back in azimuth ($\Delta\phi = \pi$), but θ will depend on this net p_z. So if $p_z = 0$, the e^+e^- pair polar angles will be equal and opposite to each other. However, if there is a net z-momentum, they will get closer together in θ.

From the point of view of a partonic collision, angles in the lab frame are usually not that interesting. So it's preferable to use variables that have the same values both in the lab and partonic center-of-mass frame. These variables are longitudinally *boost invariant*.
We can parametrize a Lorentz boost along the z-direction as the matrix:

$$K_z = \begin{pmatrix} \cosh\beta & 0 & 0 & \sinh\beta \\ 0 & 1 & 0 & 0 \\ 0 & 0 & 1 & 0 \\ \sinh\beta & 0 & 0 & \cosh\beta \end{pmatrix} \tag{2.9}$$

A four momentum p^μ transforms under this Lorentz transformation as:

$$p^\mu \to p'^\mu = \Lambda^\mu{}_\nu(z)\, p^\nu = K^\mu_\nu(z)\, p^\nu \tag{2.10}$$

$$\begin{cases} E \longrightarrow E\cosh\beta + p_z \sinh\beta \\ p_x \longrightarrow p_x \\ p_y \longrightarrow p_y \\ p_z \longrightarrow p_z \cosh\beta + E\sinh\beta \end{cases} \tag{2.11}$$

The **transverse momenta**, which are p_x and p_y (the x and y components of the momentum), are boost invariant.

$$\vec{p}_T \equiv (p_x, p_y), \qquad p_T \equiv |p_T| \tag{2.12}$$

The azimuthal angle ϕ is also boost invariant.

$$tan\phi = \frac{p_x}{p_y} \tag{2.13}$$

To find another boost invariant quantity, let's consider $c = \cosh\beta$ and $s = \sinh\beta$ so that we have $c^2 - s^2 = 1$. Under a Lorentz boost we have:

$$\frac{E + p_z}{E - p_z} \longrightarrow \frac{E(c+s) + p_z(c+s)}{E(c-s) - p_z(c-s)} = \frac{(E+p_z)(c+s)}{(E-p_z)(c-s)} = \frac{E+p_z}{E-p_z}(c+s)^2$$

because $(c+s)(c-s) = c^2 - s^2 = 1$.
This motivates defining the **rapidity** as:

$$y = \frac{1}{2}\ln\frac{E+p_z}{E-p_z} \longrightarrow \frac{1}{2}(\ln\frac{E+p_z}{E-p_z} + 2\ln(c+s)) = y + \ln(c+s) \tag{2.14}$$

So, the difference between two rapidities is boost invariant. Therefore, we define the **angular separation**, which is boost invariant, as:

$$R = \sqrt{(\Delta\phi)^2 + (\Delta y)^2} \tag{2.15}$$

Plotting distributions in terms of rapidity functions instead of polar angle helps better to separate the physics of the protons producing the boost from our hard collision physics.
To see the rapidity as an intuitive concept, let's consider particles with no mass. These particles have $E = \mid \vec{p} \mid$. Then by drawing a small momentum triangle we can find that $\cos\theta = \frac{p_z}{|\vec{p}|} = \frac{p_z}{E}$.

$$y = \frac{1}{2}\ln\frac{E+p_z}{E-p_z} = \frac{1}{2}\ln\frac{1+\cos\theta}{1-\cos\theta} = \frac{1}{2}\ln\frac{2\cos^2\frac{\theta}{2}}{2\sin^2\frac{\theta}{2}} = \ln\cot\frac{\theta}{2}\,, \qquad m = 0 \text{ only} \tag{2.16}$$

Hence there is a simple relation between angle and rapidity for massless particles. This inspires the definition of **pseudorapidity** η as:

$$\eta \equiv \ln\cot\frac{\theta}{2} \tag{2.17}$$

Using Taylor expansions of this last expression around $\theta \simeq \frac{\pi}{2}$ gives:

$$\eta \simeq \frac{\pi}{2} - \theta \tag{2.18}$$

The ATLAS and CMS detectors measure particles up to pseudorapidities of around ± 5.

To summarize, we can say:

1. Rapidity is a *kinematic quantity* defined as $y = \frac{1}{2}\ln\frac{E+p_z}{E-p_z}$.
2. It is not boost invariant in itself, but variations in rapidity are boost invariant.
3. Some other boost invariant quantities are $\vec{p_T} = (p_x, p_y)$ and $\phi = \tan^{-1}\frac{p_x}{p_y}$.
4. Pseudorapidity $\eta \equiv \ln\cot\frac{\theta}{2}$ is a *geometric quantity.*
5. It is the same as rapidity only for massless particles. For particles with mass, differences in pseudorapidities are not boost invariant.

2.6 Observables

All collider observables depend on the momentum and energy of the produced particles. The ideal way is to be able to measure the **4-momentum** of every particle in a significant event, but it is not quite attainable in practice unfortunately. What can actually be measured is the **energy** of all the particles that are stable on detector timescales. It is measured with the various calorimeters deposits and **directions of particles** (η, ϕ). In the calorimetery system, most particles transfer their energy in total, except two: neutrinos and muons. Neutrinos leave the detector without interacting with anything, so they end up not being detected at all. As for muons, they flow all the way through the detector before losing their energy. A muon momentum is measured using the curvature of its trajectory in the muon spectrometer. Strong magnetic fields are used to bend the trajectory. And since the curvature of the energetic tracks is small, a lot of space is needed (what makes ATLAS and CMS so big). There's also use of the curvature of tracks in the inner detector, for distinguishing between charged particles like electrons and measuring their **3-momentum** [26].

The **missing transverse momentum** $\vec{p}_T^{\,\text{miss}}$ is a standard observable derived from the momenta of particles. It is a 2-vector:

$$\vec{p}_T^{\,\text{miss}} \equiv -\sum_j \vec{p}_T^{\,j} \tag{2.19}$$

The **missing transverse energy** (MET) is a related quantity, which is a scalar:

$$E_T^{\text{miss}} \equiv |\vec{p}_T^{\,\text{miss}}| \tag{2.20}$$

Examples :

- An event having a W^- boson that decays into $e^-\nu$. We will only be able to detect the electron and not the neutrino. The 4-momentum of the electron is measurable. The neutrino's momentum should have transverse components (p_x and p_y) opposite to those of the electron. This doesn't apply to the p_z component because of the longitudinal boost of the partonic system. Therefore, the neutrino's transverse components are given by $\vec{p}_T^{\,\text{miss}}$. If it's known that the W boson was on-shell, it gives an additional restriction that can allow the full reconstruction of the neutrino momentum.
- An event having more than one neutrino. All the neutrinos momenta can not be reconstructed. We take $p \to Z \to \nu\nu$ events, the neutrinos could have gone anywhere if there is no transverse momentum to be measured at all (this would not even trigger since there is nothing interesting to see).

$\mathbf{H_T}$ is another common quantity used. There is no precise definition of it, but it usually

indicates the scalar sum of the missing transverse momentum in some object categories. We may find for example:

$$H_T = \sum_{\text{jets } j} |\vec{p}_T^{\,j}|, \qquad \text{or} \qquad H_T = \sum_{\text{leptons } j} |\vec{p}_T^{\,j}| \tag{2.21}$$

The **invariant mass** of certain objects can also be quite interesting:

$$m^2_{\text{objects}} = |\sum_{\text{objects } j} p^\mu_j|^2 \tag{2.22}$$

For example, we will make use of the four-lepton invariant mass later in our study for reconstructing the Higgs signal in the $H \to ZZ^* \to 4l$ channel.
The invariant mass of two particles (1) and (2) is: $m = \sqrt{(E_1 + E_2)^2 - (\vec{p}_1 + \vec{p}_2)^2}$. But we don't always have all three components of the momentum p. In that case, we can at least consider the **transverse mass**:

$$m_T \equiv \sqrt{(E_T^1 + E_T^2)^2 - (\vec{p}_T^{\,1} + \vec{p}_T^{\,2})^2} \tag{2.23}$$

with $E_T = \sqrt{m^2 + p_T^2}$ being the **transverse energy**.
- If p_1 and p_2 are both purely transverse ($\eta = 0$) $\Rightarrow m_T = m$.
- If p_1 and p_2 are both purely longitudinal $\Rightarrow m_T = 0$.
- Otherwise $\Rightarrow 0 < m_T < m$.

2.7 ATLAS search channels for the Higgs boson

We will try to describe the signature of an SM Higgs boson decay at the LHC for a mass around 125 GeV [37–40].

At first, it would seem logical to chose the $b\bar{b}$ decay mode to observe our particle, since it has the largest branching ratio at $m_H = 125$ GeV with 57%. Unfortunately, other hadronic processes usually produce this same final state, which makes the background too large to distinguish a signal.

To achieve a convenient signal to background ratio, it's better to look at decays into leptons or photons. The most common leptonic decay is the $\tau^+\tau^-$ channel which happens 6% of the time. However, there's a probability of 75% for the τ lepton to decay into hadrons. Which makes it suffer from a large background as well. This leaves us with the lighter leptons (muons and electrons). The direct decay into these leptons, like muons, has a really small branching ratio (0.02%), and thus it's not possible to get separated from the typical di-lepton background.

For a good signal to background ratio with a leptonic final state, we have the $W^\pm$ and Z

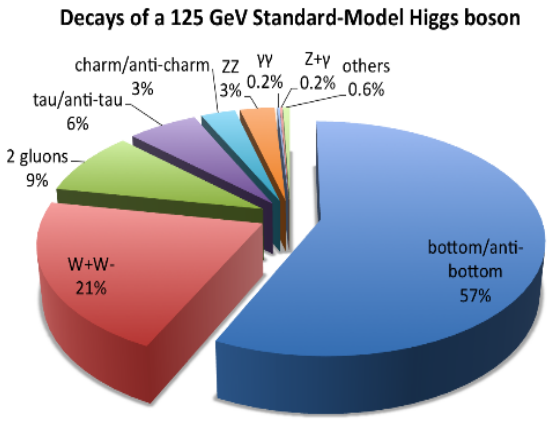

Figure 2.5: Standard Model Higgs boson decay branching ratios at $m_H = 125$ GeV [40].

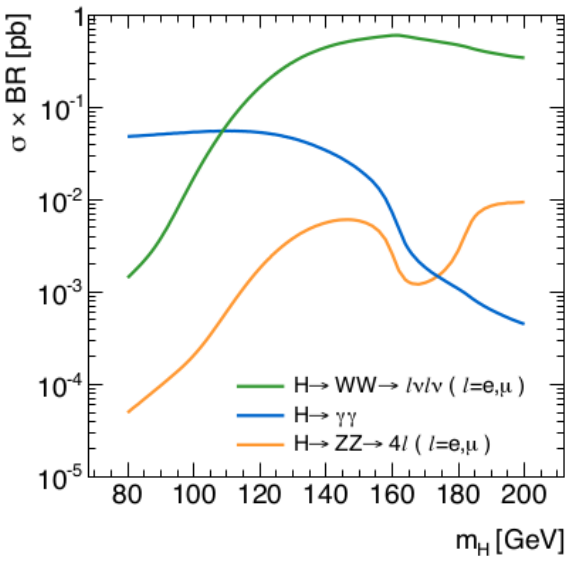

Figure 2.6: Higgs boson production cross section times branching ratio for the three decay channels: $H \to ZZ^* \to 4l$, $H \to W^+W^- \to l\nu l\nu$, $H \to \gamma\gamma$ [37].

bosons decay modes, which subsequently decay into leptons. As for the decay into photons, the $H \to \gamma\gamma$ decay channel can also be very helpful despite its small branching ratio (0.2%).

To resume, the best channels to exploit in order to observe the Higgs signal are:

1. $pp \to H \to ZZ^* \to 4l$
2. $pp \to H \to WW^* \to e\nu\mu\nu$
3. $pp \to H \to \gamma\gamma$

These channels have showed to be crucial for the Standard Model Higgs boson discovery and the measurement of its properties.
Our thesis will focus exclusively on the four-lepton decay channel $pp \to H \to ZZ^* \to 4l$.

Chapter 3

Simulating data for the Higgs search

3.1 Why did we choose the $pp \to H \to ZZ^* \to 4l$ channel?

In this section, we are going to explain why we chose the four-leptons channel: $pp \to H \to ZZ^* \to 4l$ for our study, in the search for a Standard Model Higgs boson. The * on one of the Z bosons means it is off-shell, as it must be since $m_H < 2M_Z$.

$$pp \to H \to ZZ^* \to l^+ l^- l'^+ l'^- \qquad \text{with } l, l' = e, \mu. \tag{3.1}$$

This channel is called the *golden channel*, since it has the cleanest and clearest signature among all the possible Higgs decay modes. It has small background and the Higgs can be fully reconstructed. So the use of this channel provides some exceptional advantages, summed up in what follows [37]:

- The final state can be fully reconstructed by the detector, as it consists of four charged leptons. This allows precise measurements of the Higgs' properties; such as determining the invariant mass for its mass, and the total angular momentum for its spin by using the angular dependence of the 4 leptons.
- The decay chain doesn't involve any hadrons, therefore the leptons in the final state are separated from the hadronic processes of the underlying events. This makes it easy to distinguish the signal from the background resulting from leptonic decays of hadrons.
- The leptons of the final state are produced by a Z boson decay, which is several orders of magnitude heavier than other particles (even when being off-shell). As a result, the leptons will have a relatively high momentum, making them easy to distinguish from leptons produced by QCD processes.

Unfortunately, $H \to ZZ^*$ represents only 3% of Higgs decays, and the Z boson decays

into leptons only 6% of the time, which is a relatively small cross section. Thus if we take the first run of the LHC as an example (run 1): out of the 500 thousands Higgs produced, there were only about 50 events of $H \to ZZ^* \to 4l$ [26]. And by taking experimental efficiencies into consideration, this value further reduces to a measly handful of events actually observed. That's why data selection and collection is so important, as well as reducing the impact of the background processes with a larger cross section, which comes as a priority right after that.

3.2 Background estimation

There are two categories of backgrounds for a signal in any physics process [37]:

1. *Irreducible background* : it consists of the SM processes that share the same final state as the signal reaction.

2. *Reducible background* : it is constituted of events that are different from the signal, but can mimic it because of a misreconstruction of the physics objects.

3.2.1 Irreducible background

Let's focus now on the background of our channel. The SM events which produce the same final state as $H \to ZZ^* \to 4l$ are shown in the Figure 3.1 as Feynman diagrams.

$$\begin{cases} qq \to ZZ^*(\gamma) \to 4l \\ \\ gg \to ZZ^*(\gamma) \to 4l \\ \\ qq \to Z \to 4l \end{cases} \tag{3.2}$$

These processes are not distinguishable from the signal, and contribute in the distribution of the four-lepton invariant mass. Their cross sections are predicted by the Standard Model. And thus even though it's an irreducible background, it can be estimated then taken into consideration in the counting of events.
For Higgs masses below $2M_Z \simeq 182$ GeV, the most significant irreducible background contribution comes from $qq/gg \to Z\gamma$ events, considering the cross section of the photon production is much larger than an off-shell Z boson.
For values of the Higgs boson mass above the threshold $m_H = 2M_Z$, the irreducible background increases since there is a production of a pair of on-shell Z bosons.

For a better understanding of the difference between the signal and the irreducible background process, it's interesting to study some kinematic variables at the Monte Carlo generator

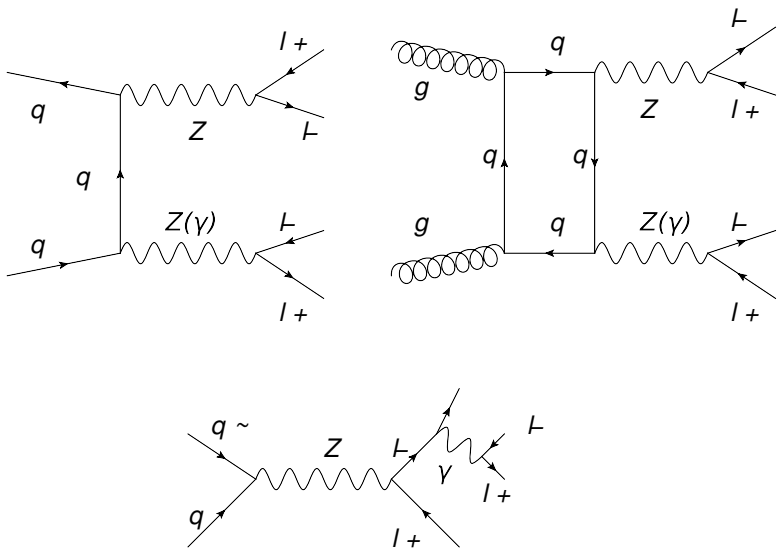

Figure 3.1: Feynman diagrams of the relevant SM processes producing the same final state as a Higgs boson decay into four leptons.

level (before the reconstruction). For example, the Figure 3.2 shows the pseudorapidity distribution. In the region of the detector acceptance ($|\eta| < 2.5$), the signal and background distributions almost entirely overlap. The chosen regions may lead to a loss of events with one of the four leptons falling outside.

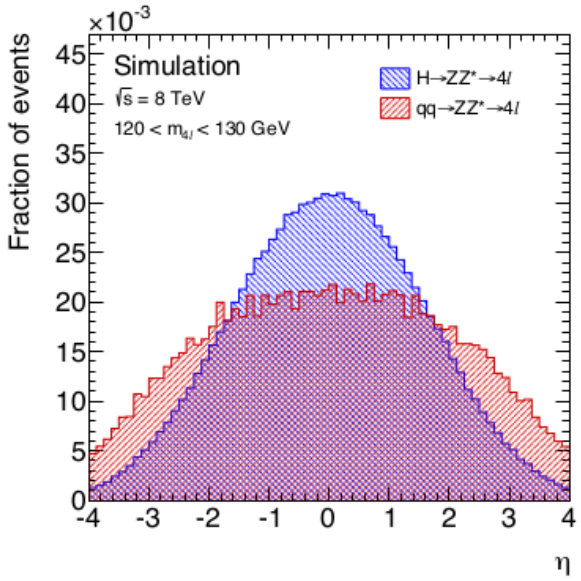

Figure 3.2: Generator-level distributions of the lepton pseudorapidity obtained from the $H \to ZZ^* \to 4l$ signal process (blue) with $m_H = 125$ GeV and the $qq \to ZZ^* \to 4l$ background process (red) [37].

3.2.2 Reducible background

Let's talk about the reducible background now. The ZZ^* background is evaluated by applying the event selection to the simulated events and by normalizing the distributions to the expected number of events from the total integrated luminosity, obtained from the Standard Model cross section prediction. Whereas reducible background events like $Z(\rightarrow ll)$+jets and $t\bar{t}$ are estimated with data-driven methods.

The composition of the reducible background depends on the flavor of the *sub-leading* lepton pair (the pair decaying from the off-shell Z^*). Different approaches are taken for the $ll + \mu^+\mu^-$ and the $ll + e^+e^-$ final states. The small contribution from the WZ reducible background is estimated from simulation.

1. $ll + \mu^+\mu^-$: with a sub-leading muon pair. This reducible background comes from Z+jets and $t\bar{t}$ (mostly $Zb\bar{b}$ processes).

2. $ll + e^+e^-$: with a sub-leading electron pair. This reducible background comes from jets or photons misidentified as electrons.

The background estimates are driven from data, along with verified Monte Carlo simulations. It will contribute greatly in the event selection. This will be discussed in the next section.

3.3 Event selection

To increase the signal-to-background rate, events need to go through some specific selection criteria. Using trigger algorithms, the events are selected by the ATLAS trigger system during the LHC runs. The sample of events picked by the trigger is reduced further by necessitating the presence of at least two lepton pairs with opposite charges ($l^+ l^- l'^+ l'^-$). Precise quality requirements should be satisfied by the leptons, specific for muons and electrons. Then events with four "good" leptons need to pass precise kinematic and topological selection criteria.

3.3.1 Triggers

Of all the events observed by the ATLAS detector, the candidate events for the Higgs boson are only a tiny fraction. The $H \rightarrow ZZ^* \rightarrow 4l$ events all need to have four leptons as final state, so the trigger algorithms specify the presence of electrons or muons with transverse energy/momentum above a distinct threshold. In a Monte Carlo sample of $H \rightarrow ZZ^* \rightarrow 4l$ events with $m_H = 125$ GeV, the fraction of simulated signal events selected by the trigger compared to the actual number of events (efficiency of the triggering algorithms) is found to be:

- 4μ : 92.2%.
- $2e2\mu/2\mu2e$: 90.9%.
- $4e$: 91.8%.

3.3.2 Lepton quality requirements

The offline event selection (or pre-selection) depends on muons and electrons reconstructed by the ATLAS detector. This is performed by applying cuts on transverse momenta p_T and pseudorapidities η of reconstructed leptons. For example, electrons p_T needs to be > 7 GeV and must be within the region $|\eta| < 2.47$.

Electrons

The reconstruction of electrons in ATLAS uses energy deposits in the Electromagnetic Calorimeter associated to a track in the Inner Detector (ID). Unlike muons, that possess a quite unique signature, electrons can be easily mimicked by background objects; such as photons converted in $e^+ + e^-$ pairs, soft hadronic jets or electrons from hadronic decays. In order to avoid these backgrounds, sequential cuts and multi-variate analysis (MVA) techniques are used on different electron identification categories.

Muons

The identification of a muon in ATLAS exploits information from the Muon Spectrometer (MS), the Inner Detector (ID) and the calorimeters to a smaller extent. The ID and the MS both provide independent particle momentum measurements, which improves the resolution by combining them. Muon identification follows various reconstruction criteria, leading to different muon "types" (*Stand-Alone (SA)*, *Combined (CB)*, *Segment-tagged (ST)* and *Calorimeter-tagged (CaloTag)* muons).

3.3.3 Kinematic and topological cuts

The selection of the Higgs boson candidate events is made amidst the ones with two pairs (a quadruplet) of "good" leptons, with Same Flavor and Opposite Sign (SFOS). Within the quadruplet, only one Stand-Alone or Calorimeter-Tagged muon is admitted. The selection of the quadruplet is done separately for all the possible final states for each event.

Building of the quadruplet

- p_T thresholds for the 3 leading leptons of the quadruplet: 20, 15 and 10 GeV.
- One quadruplet for each event, with the leading and sub-leading lepton mass (m_{12} and m_{34} respectively) closest to the Z boson nominal mass.
- Leading lepton mass: $50 < m_{12} < 106$ (GeV).
- Sub-leading lepton mass: $m_{\text{threshold}} < m_{34} < 115$ (GeV).
- Reject quadruplet if $m_{ll} < 5$ (GeV), $\Delta R(l, l') > 0.10\,(0.20)$ for same (different) flavor leptons.

Reducible background suppression

Since the leptons resulting from background events such as Z+jets or $t\bar{t}$ are produced mainly by decays of hadronic particles, they are usually not isolated. For the Higgs boson candidates selection, the background of these events is reduced by applying to every lepton a requirement on the track isolation, calorimetric isolation and on the impact parameter significance.

3.4 Event simulation

In this section, we describe the techniques and steps used in the simulation of high energy proton-proton collision events [41].

3.4.1 Proton-proton collisions

The evolution of a proton-proton collision at the LHC, as showed in the Figure 3.3, can be described as follows:

1. When the two beams of protons running at opposite directions meet, proton-proton collisions happen at the intersection points. Each proton is composed of different partons, that carry fractions of its momentum. The proton composition follows *Parton Distribution Functions (PDFs)*, which are models in terms of energy sharing and flavor.
2. The partons of the colliding protons emit radiations, initiating a succession of decays $q \to qg$, $g \to q\bar{q}$, $g \to gg$. Since the strong coupling constant α_S has a large value, these branching processes have a high probability to happen (starting initial-state parton showers).

3. At a momentum transfer scale Q^2, two partons from the showers enter a hard scattering. The products are the final-state elementary particles. We note that some resonances are short-lived (such as the Z, $W^{\pm}$ and Higgs bosons), and thus decay almost instantly into partons, leptons or photons.

4. The spreading partons (quarks and gluons) begin scattering, initiating final-state showers.

5. Following every decay in the initial and final-state showers, the momentum scale is reduced down to $\Lambda_{QCD} \sim 1$ GeV. The perturbative theory is no longer valid there.

6. Under Λ_{QCD}, partons are confined into colorless hadrons by the strong interaction. After this hadronization, the unstable particles go through decay. Thus, the parton showers become jets of stable and meta-stable particles, which can be observed in particle detectors.

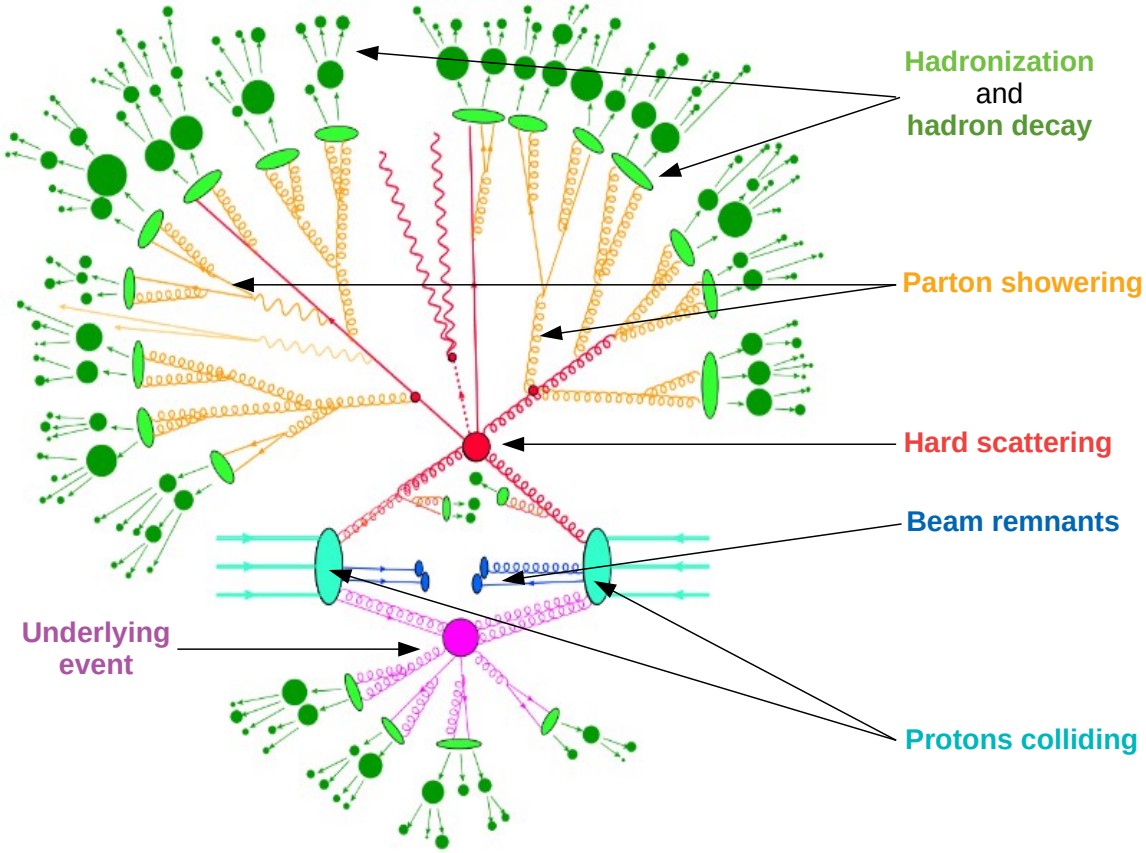

Figure 3.3: Diagram of the evolution of a hard proton-proton collision [42].

The representation of a proton-proton collision is factorized into different subprocesses. With the appropriate method, each of them is rather easy to manage. In order to simulate and reproduce the phenomenology at the LHC, this technique is used by *Monte Carlo Event Generators*.

The *factorisation theorem* allows the hard perturbative and soft non-perturbative processes to be treated separately. A proton-proton scattering ($p_A p_B \to X$) of generic final state X can be represented by this integral over the final state phase-space:

$$\sigma_{AB} = \sum_{a,b} \int dx_a \, dx_b \, d\Phi_{FS} \, f_a(x_a, \mu_F) f_b(x_b, \mu_F) \cdot \hat{\sigma}_{ab \to X} \tag{3.3}$$

where $f_a(x_a, \mu_F)$ and $f_b(x_b, \mu_F)$ are the parton distribution functions, and σ_{AB} is the total cross-section. x_a and x_b the partonic fractions of the proton momentum p_A and p_B respectively, carried by parton a and b involved in the hard interaction. And $\hat{\sigma}_{ab \to X}$ the hard partonic scattering cross-section (calculated using perturbation theory). The *factorisation scale* parameter μ_F replaces the momentum transfer Q^2. This represents the limit separating the hard and the soft process. Further calculations are possible using the perturbative expansion.

Parton distribution functions

In the equation (3.3) we've just seen, the parton distribution functions (PDFs) describe the dynamics of the partons participating in the hard process in relation with the protons colliding. They model the probability of a parton to carry a fraction x of the proton momentum.
The dependence in x is derived from global fit to data. Results are accessible in the tree-level and next-to-leading (NLO) orders, and only partly in the next-to-next-to-leading order (NNLO). The PDF estimations uncertainties need to be taken into consideration in any theoretical prediction (uncertainties on experimental data and analysis, uncertainty on α_S...).
There are many PDF sets available, we mention the most common ones: CTEQ [23], MSTW [24] and NNPDF [43]. They mainly differ in the number of parameters of the model and the data used in the processes fit.

3.4.2 Principles of Monte Carlo event generation

Here we will introduce the main principles on which Monte Carlo event generation is based in order to provide a simulation [44].

Random number generation

A pseudo-random number generator is a deterministic algorithm that produces a series of values "sufficiently" disorganized to look like a random sample. It follows a unifrom distribution (let's say on the interval $[0, 1]$). There are many methods to generate such numbers, such as the middle square method, Fibonacci generator, congruence methods... And there are different tests to check the properties and quality of a pseudo-random number generator.

Such generators are used in computers, and they represent the main source for generating random numbers that follow any classical probability distribution (discrete and continuous). This takes a mojor part in the simulation process.

Monte Carlo methods for integral calculations

We call a *Monte Carlo* method any method aiming to calculate a numerical value by using random number generation, namely probabilistic techniques.
Monte Carlo methods are mainly used for the approximate computation of integrals, based on *the law of large numbers* (which assures that the average of the results collected from performing the same experiment a large number of times ought to be close to the expected value, and gets closer the more the number is larger). Hence it allows the calculation of approximate values of expected values (noted $\mathbb{E}$) of probabilities, using identically and independently distributed realizations of a law that we know how to simulate. For example, suppose we want to calculate the integral $I = \int_a^b h(x)\,dx$, that we can present in the form :

$$I = \int_a^b h(x)\,dx = \int_a^b f_X(x)g(x)\,dx \tag{3.4}$$

where the function f_X is supposed to be a probability density of the random variable X: $f_X(x) \geq 0$ and $\int_a^b f_X(x)\,dx = 1$. The Monte Carlo method suggests to **estimate** I by the quantity:

$$\widehat{I}_n = \frac{1}{n}\sum_{i=1}^{n} g(X_i) \tag{3.5}$$

with X_1, X_2, ..., X_n being independent realizations that follow the density law f_X.
Indeed, according to the law of large numbers, $\widehat{I}_n$ converges almost surely and:

$$\lim_{n\to\infty} \frac{1}{n}\sum_{i=1}^{n} g(X_i) = \mathbb{E}[g(X)] = I \tag{3.6}$$

Thus for n large enough, $\widehat{I}_n$ provides a good approximation of I.

We note that unlike other methods of numerical integration, such as the trapezoidal rule and Simpson's rule who use a deterministic approach, Monte Carlo methods follow a non-deterministic approach. Which means each realization provides a different outcome. Monte Carlo may be slower than the other methods for n points taken, but it shows to be the best for phase-space integrals and higher dimensions. The advantage it has is the independence of the speed of convergence from the dimension of the problem, contrary to other deterministic methods that depend on it, which reduces their speed considerably.

Monte Carlo Event Generators

In order to do the simulation of high energy collisions in detail down to final-state individual stable particles, we use *Monte Carlo Event Generators* (MCEGs). The objective is generating a large amount of simulated collision events, characterized by final-state particles and their four-momenta, taking into consideration the probability to generate an event to be equivalent to the probability of producing the actual event in the real experimental data. They represent a very important tool for collider physics.
The simulated data provided by these generators help in analysing and comparing theoretical models and calculations with experimental data and detector measurements. Collider physics experiments depend on simulated events by MCEG codes (such as Herwig, Pythia, Sherpa, POWHEG...) in order to design and adjust detectors and analysis strategies.

Steps in the event generation process

Making use of the factorization theorem, different steps can be described for the event generation of a hadronic collision (proton-proton) [41].

1. **The computation of the hard subprocess (Matrix Element ME)**: the hard subprocess simulation is the first step of the event generation. A hard process is when partons (quarks and gluons) of the two protons colliding interact with each other at a high momentum scale. Since the strong coupling constant α_S is quite small for the hard subprocess, it can be evaluated with perturbation theory and by a matrix element. In this hard interaction, only one parton of high energy fraction of the proton participates with an energetic parton of the other proton. This produces two further transverse sprays of fundamental objects, whereas the remaining partons keep running without engaging in the main interaction. These partons represent the so-called underlying event, and thus will become relevant later. The particles who appear in the hard subprocess will take place in the following parton shower step.

2. **The parton shower step (PS)**: because of the big momentum transfers throughout the hard subprocess step, the final-state particles gotten from the matrix element have high energies. The involved partons enter a parton shower that keeps going until their energy decreases by collinear parton decay and/or soft gluon emission to the point they enter the hadronization step. This happens because the partons (quarks and gluons) of the hard process who carry a color charge can emit QCD radiation through gluons, who themselves carry a color charge leading them to interact with each other by additional gluon emissions. To describe the parton shower, there exists different approximation schemes.

3. **The hadronization process** : during the parton shower, the partons lose energy through decay and gluons emission, and α_S increases at the same time. At some point, the coupling between color-charged partons becomes strong enough to create colorless hadrons out of binding partons. The hadronization process starts at an energy of around $\sim$ 1GeV (depending on the hadronization model), and the perturbative methods currently available can not calculate it. That's why hadronization models which are based on experimental data are used to describe these hadron formations. Unstable and short-lived hadrons keep decaying into other hadrons until only stable ones are left.

4. **The underlying event** : the partons of the protons that didn't take part in the hard process are called the beam remnants. These can also emit gluons themselves as underlying events, and thus participate in the hadronization process.
   The event generation technically ends here. However, Monte Carlo event generation can keep going with additional steps, for a complete simulation up to a full analysis :

5. **Pile-up simulation** : in a bunch crossing at the collider, there are multiple proton-proton interactions at the same time. They constitute what we call the pile-up. It is modeled using either recorded data events to emulate it or a detailed simulation of the detector to recreate it.

6. **Detector simulation** : a full simulation of the ATLAS detector gives the expected response after the propagation of final-state particles through the magnetic field and their interaction with the different detector components. For each particle, these interactions with the material are simulated, including energy loss, photon conversions and Bremsstrahlung.

7. **Reconstruction and identification step** : what a particle detector measures at first are hits of particles of the final-state in the subdetectors cells. After that, tracks and objects are reconstructed with these data, by applying reconstruction algorithms that take into consideration particle types properties in order to identify these objects.

3.4.3 MadGraph5_aMC@NLO as an event generator

MadGraph5_aMC@NLO [45] is a Monte Carlo event generator for collider physics. It is a fully automated and public computer code. It is used nowadays to simulate LHC events. It is also a tool to obtain future predicitons in new physics models.
This software can generate processes and their Feynman diagrams, it can also include several extensions, such as: the code **Pythia** [46], which is a random event generator, used for parton showering and hadronization (takes jets into consideration). Or **Delphes**, which simulates the

detection process and event reconstruction. This provides a complete LHC simulation, starting from events at the parton level to detector results. Here's a list of these packages:

- **MadAnalysis** : to draw automatically different histograms, in relation with the event generation.
- **ExRootAnalysis** : to convert the different outputs to a ROOT format.
- **Pythia** : to simulate parton showering and hadronization.
- **Delphes** : to simulate the detector.

We can turn on or off these additional pieces, depending on the kind of simulation we actually need. For example, if we only want to calculate a cross-section at the parton level, the basic MadGraph software is enough and the rest is unnecessary. However, if we want to include hadronization and detector simulation, we'll need to use Pythia and Delphes in addition.
Events at the parton level (**MadEvent**) ⇒ Showering and hadronization (**Pythia**) ⇒ Detector response (**Delphes**).
The MC@NLO part is an implementation of this formalism package to MadGraph, combining in a unique framework all of their features, thus superseding both of them and including some new capabilities (it's the most recent version at the moment). It is capable of computing tree-level and one-loop NLO (Next-to-Leading Order) amplitudes for any given process. Physical observables can be predicted with different perturbative accuracies and final-state descriptions using such calculations.

3.4.4 Example using MadGraph5_aMC@NLO simulation

In this example, we are attempting to make a simulation for the $H \to ZZ^* \to 4l$ process, using MadGraph5_aMC@NLO. The software is available to download for free on its official website [47], an online generation is also available (though only in leading order). As the Figure 3.4 shows, the interface is accessible directly through the terminal after installing it on the computer (a Linux operating system is necessary).

Setup

Before starting the simulation, we make sure to configure the process generation properly:

- We generate $H \to ZZ^* \to 4l$ in MadGraph with the command :
  generate p p > h, (h > z l+ l−, z > l+ l−)
- Configuration : we turn ON Delphes, Pythia and MadAnalysis5.

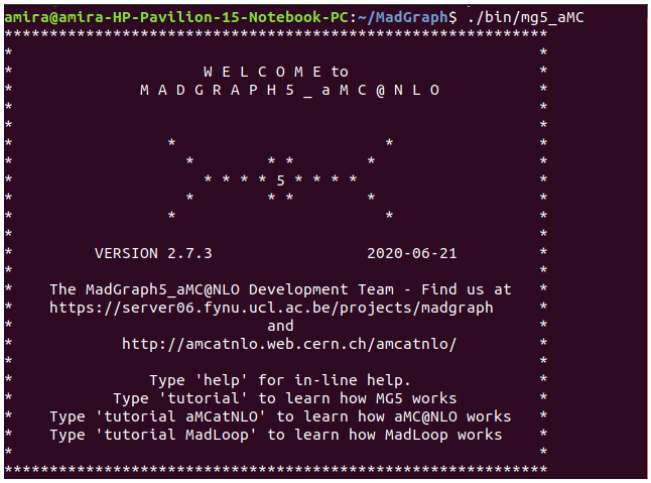

Computer interface.

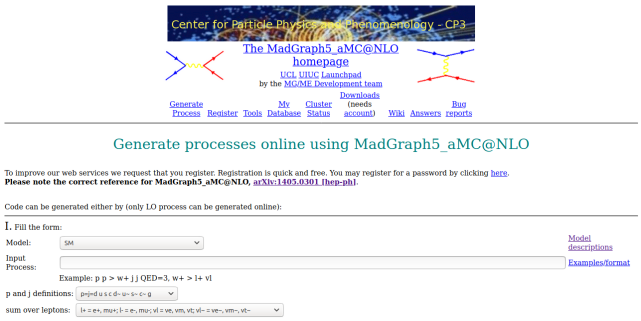

Official website.

Figure 3.4: Screenshot of the MadGraph5_aMC@NLO interface and website [47].

- Histograms : are given for an integrated luminosity of $10 fb^{-1}$.
- Datasets : samples consisting of signal events.
- We set the number of generated events to 10000 events, and the center-of-mass energy to 13 TeV (each beam energy set to 6500 MeV).

After around an hour of compilation, we get a MadAnalysis report file in .pdf version as output. It includes a variety of histograms of different observables of the process, in terms of the number of events. The one we are the most interested in is the four-leptons mass, shown in the following Figure 3.5. We clearly see a peak around 125 GeV.

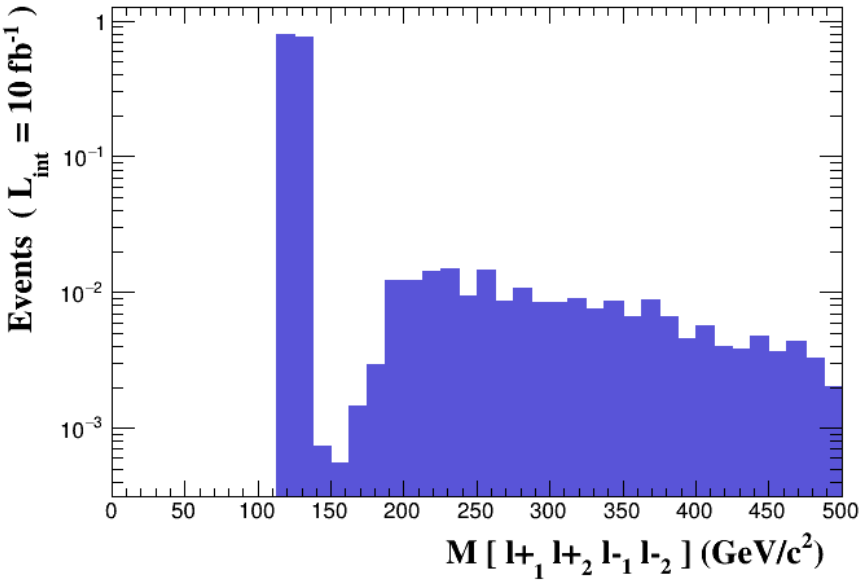

Figure 3.5: Histogram of the four-leptons mass output from MadGraph5_aMC@NLO.

Chapter 4

Reconstructing the Higgs signal through the $pp \to H \to ZZ^* \to 4l$ golden channel

In this section we are ready to describe the experimental Higgs boson search in the four lepton decay channel. Only events with two pairs of oppositely charged electrons or muons are selected; the invariant mass of the four leptons (m_{4l}) is used to reconstruct the mass of the Higgs boson spectrum. The leptons produced by the decay of the Z boson is called the *leading pair*, while the second pair decaying from Z^* represents the *sub-leading pair*. The search for the Higgs boson in the channel $H \to ZZ^* \to 4l$ is done via its four possible final states:

1. $\mu^+ \, \mu^- \, \mu^+ \, \mu^-$ (4μ).
2. $e^+ \, e^- \, e^+ \, e^-$ ($4e$).
3. $\mu^+ \, \mu^- \, e^+ \, e^-$ ($2\mu 2e$).
4. $e^+ \, e^- \, \mu^+ \, \mu^-$ ($2e2\mu$).

4.1 ATLAS Open Data

ATLAS Open Data [48] is a set of *pp* collision data accompanied with several tools [49] released by the ATLAS Collaboration as an open-access to the public, specifically for educational and research purposes. The general aim is to provide a straightforward interface to replicate the procedures used by High-Energy Physics (HEP) researchers and enable users to experience the analysis of particle physics data in educational environments.
Considering our channel is the four-lepton channel, the dataset we'll be using is from "ATLAS

13 TeV samples collection at least four leptons (electron or muon), for 2020 Open Data release" [50,51]. It consists of $10fb^{-1}$ of collision data at a center-of-mass energy of 13 TeV from the 2016 data taking period. This set of real data is accompanied by matching simulated data of Standard Model processes and a selection of Beyond the Standard Model signals.
Events are selected with at least four leptons (electron or muon). Both real and simulated data go through a loose event preselection, in order to reduce processing time by decreasing the overall number of events that will be analysed. The preselection consists of a set of object selection criteria followed by an event selection subjected to these preselected objects.

4.1.1 Experimental samples

Our analysis is based on the datasets collected by the ATLAS experiment during the second run of the LHC operation. The data has been collected by the ATLAS detector at a center-of-mass energy of $\sqrt{s} = \mathbf{13\ TeV}$ during the year 2016. It corresponds to an integrated luminosity of $\mathbf{10fb^{-1}}$.
The 13 TeV ATLAS Open Data events belong to **61 runs** from the first four periods of the 2016 *pp* data-taking and contain approximately **270 million** of collision events. Over a billion particle interactions take place in the ATLAS detector every second. The maximum average number of *pp* interactions per bunch crossing in this dataset is 79.8 collisions and the bunch spacing is 25 ns.
ATLAS has published a volume of $10fb^{-1}$ data at 13 TeV which corresponds to approximately one quadrillion proton-proton collisions or the production of **500 thousand** Higgs bosons. $10fb^{-1}$ is part of the $139fb^{-1}$ collected by the run 2 of LHC (cumulative luminosity: 1^{st} and 2^{nd} run).
The 13 TeV experimental datasets contain several reconstructed physical objects (such as electrons, muons, photons, jets...). Our channel is the $H \to ZZ^* \to$ 4leptons channel, so we'll be using events selected with at least four leptons (electron or muon). Only about less than 900 events of interest remain, considering cross sections and efficiencies. Among the provided experimental data, the observables we will actually use are:

- Transverse momentum of the lepton p_t (Lep_pt);
- Pseudorapidity of the lepton η (Lep_eta);
- Azimuthal angle of the lepton ϕ (Lep_phi);
- Energy of the lepton (Lep_E);
- Charge of the lepton (Lep_charge);
- Type of the lepton (Lep_type; 11 for an electron e, 13 for a muon μ).

4.1.2 Simulated samples

The *pp* collision data is accompanied by a set of Monte Carlo (MC) simulated samples describing several processes, which are used to model the expected distributions of different signal and background events. Simulated data sets allow us to compare theory to real data. They are based on theoretical models of the physical processes expected during collisions, associated with a detailed description of the ATLAS detector.
The aim of the analysis is to isolate the low mass Higgs bosons decaying into Z bosons pair and subsequently four leptons from a sea of various SM processes. This is realised by imposing, on the data sample, cuts which are carefully designed so that a maximum sensitivity of the $H \rightarrow ZZ^* \rightarrow 4l$ process can be reached. We also use histograms analyses to differentiate between physics processes by applying cuts to data, specific physics processes (signal) can be isolated from the background. **Cuts** preferentially remove the unwanted processes (background) but leave as much as possible of the desired process (signal). It is useful to have a good understanding of the physics processes involved when applying cuts.
Among the provided simulated data, same observables as in the experimental samples are needed, plus additional quantities that only accompany the simulated data:

- Weight of a simulated event (mcWeight);
- Scale factor for pile-up reweight (scaleFactor_PILEUP);
- Scale factor electron efficiency(scaleFactor_ELE);
- Scale factor muon efficiency (scaleFactor_MUON);
- Scale factor to account for the different operating efficiencies of the used triggers (scaleFactor_LepTRIGGER).

These scale factors apply corrections for various object efficiencies by using pre-cuts.

Simulated data

According to the ATLAS Collaboration [52], the $H \rightarrow ZZ^* \rightarrow 4l$ signal is modelled using the POWHEG [53] Monte Carlo event generator, which calculates separately the gluon fusion (ggF) and vector-boson fusion (VBF) production mechanisms with matrix elements up to next-to-leading order (NLO). POWHEG is interfaced to PYTHIA [46] for showering and hadronization, which in turn is interfaced to PHOTOS [54] for quantum electrodynamics (QED) radiative corrections in the final state. PYTHIA is used to simulate the production of a Higgs boson in association with a W or a Z boson (VH) and with a $t\bar{t}$ pair ($t\bar{t}H$).
The cross sections for the ggF process have been calculated to NLO [55], and next-to-next-to-leading order (NNLO) in QCD [56]. In addition, QCD soft-gluon re-summations calculated in

the NNLL (next-to-next-to-leading logarithmic) approximation are applied for the ggF process. NLO electroweak (EW) radiative corrections are also applied. The cross sections for VBF processes are calculated with full NLO QCD and EW corrections, and approximate NNLO QCD corrections are available. The cross sections for the associated WH/ZH production processes are calculated at NLO and at NNLO in QCD, and NLO EW radiative correction are applied. The cross sections for associated Higgs boson production with a $t\bar{t}$ pair are calculated at NLO QCD.
The Higgs boson decay branching ratios to the different four-lepton final states are provided by PROPHECY4F [57], which includes the complete NLO QCD+EW corrections and interference effects between identical final-state fermions.

Background simulation

The ZZ^* continuum background is modelled using:

- POWHEG for quark-antiquark annihilation.
- $gg2ZZ$ for gluon-gluon contributions, normalised to the MCFM prediction.

The ZZ^* qq' continuum background is modelled using SHERPA [58]. The QCD scale uncertainty has a $\pm 5\%$ effect on the expected ZZ^* background, and the effect due to the PDF and α_s uncertainties is $\pm 4\%$ ($\pm 8\%$) for quark-initiated (gluon-initiated) processes. TAUOLA [59] is used for the simulation of τ lepton decays which come from both signal and background Z decays. The Z+jets production is modelled using ALPGEN [60] and is divided into two sources: Z+light jets, which includes $Zc\bar{c}$ in the massless $\bar{c}$ quark approximation and $Zb\bar{b}$ with $b\bar{b}$ from parton showers, and $Zb\bar{b}$ using matrix element calculations that take into account the b quark mass. For comparison between data and simulation, the QCD NNLO FEWZ and MCFM cross section calculations are used for inclusive Z boson and $Zb\bar{b}$ production, respectively. The $t\bar{t}$ background is modelled using MC@NLO and is normalised to the approximate NNLO cross section calculated using HATHOR [61].

4.2 Efficiency

Reconstruction and identification efficiency are the two main components of electron and muon detection efficiency [37].

- **Electron reconstruction efficiency:** the tag-and-probe method applied to $Z \to e^+e^-$ events is used to determine the efficiency of the electron reconstruction. The tag is one of the two electrons used to define the event, while the probe, which is the second electron,

is used to measure the efficiency. The charge of the tag+probe electrons must be opposite and their invariant mass m_{ee} should be within ±15 GeV from the Z boson mass m_Z.

- **Electron identification efficiency:** the efficiency of the electron identification algorithms is also measured using a tag-and-probe method from real and simulated $Z \to e^+e^-$, $Z \to e^+e^-(\gamma)$, $J/\Psi \to e^+e^-$ decays. The identification efficiency generally grows as a function of E_T because more energetic electrons are better separated from the background. The shape of the efficiency as a function of the pseudo-rapidity reflects some well-known detector features.

- **Muon reconstruction efficiency:** since the ATLAS detector structure is not the same all over the $|\eta|$ range, the efficiencies in the central ($|\eta| < 2.5$) and in the forward region ($|\eta| > 2.5$) are measured with different strategies. As a function of p_T, the $Z \to \mu^+\mu^-$ sample is complemented with lower p_T muons, obtained from $J/\Psi \to \mu^+\mu^-$ decays. Low p_T muons are very important also in the $H \to ZZ^* \to 4l$ analysis since one of the two Z bosons is off-shell.

4.3 Systematic uncertainties

The systematic uncertainties are determined by comparing the nominal event yield with the one obtained after having modified relevant quantities, by applying *weights* on Monte Carlo. The systematic uncertainty on the energy for electrons or momentum for muons (scale or resolution) is calculated by a scale factor for selecting data events, and by observing the number of events after the selection. Several systematic uncertainties are taken into account in the analysis. We have uncertainties due to the identification and reconstruction of leptons, luminosity, the estimation of background and cross sections of the Higgs boson production.

4.3.1 Leptons

The uncertanties on the lepton reconstruction and identification efficiencies and on the momentum scale and resolution are studied from $Z \to l^+l^-$ and $J/\psi \to l^+l^-$ decays. The 2μ2e and 2e2μ modes differ by the flavor of the lepton pair having a reconstructed invariant mass closest to the Z mass.

- **Electrons**: the relative uncertainty on the signal acceptance due to the uncertainty on the efficiency of reconstruction and electron identification for a Higgs boson of mass $m_{4l} = 600$ GeV is ±2.6% ±1.7% and ±1.8% [7] in channel 4e, 2e2μ and 2μ2e respectively, and ±9.4% (±8.7%/±2.4%) at $m_{4l} = 125$ GeV [52].

- **Muons**: the relative uncertainty on the signal acceptance due to the uncertainty on the efficiency of reconstruction and muon identification for a Higgs boson of mass $m_{4l} = 600$ GeV is $\pm 0.7\%$, $\pm 0.5\%$ and $\pm 0.5\%$ [7] in channel 4μ, $2e2\mu$ and $2\mu 2e$ respectively, and $\pm 0.9\%$, $\pm 0.8\%/\pm 0.5\%$ at $m_{4l} = 115$ GeV [7].

4.3.2 Electron energy scale

The electron energy scale uncertainties determined from $Z \to e^+e^-$ and $J/\psi \to e^+e^-$ decays, is propagated as a function of the pseudo-rapidity η and the transverse energy E_T of the electrons. The uncertainties on the measured Higgs boson mass due to the electron energy scale uncertainty are $\pm 0.04\%$, $\pm 0.025\%$ and $\pm 0.04\%$ for the 4e, $2e2\mu$ and $2\mu 2e$ final states respectively [37].

4.3.3 Muon energy scale

The systematic uncertainties on the muon momentum scale are determined using a large samples of $Z \to \mu^+\mu^-$ and $J/\psi \to \mu^+\mu^-$ decays. The uncertainties on the measured Higgs boson mass due to the muon energy scale uncertainty are $\pm 0.04\%$, $\pm 0.015\%$ and $\pm 0.02\%$ for the 4μ, $2e2\mu$ and $2\mu 2e$ final states, respectively [37].

4.3.4 Integrated luminosity

The normalisation uncertainty on the integrated luminosity is $\pm 2.4\%$ [62,63] for data at 13 TeV.

4.3.5 Background estimation uncertainties

The uncertainties on the data-driven estimation of the reducible background are due to the uncertainty on the transfer factors caused by limited Monte Carlo statistics [7].

4.3.6 Theoretical uncertainties

These uncertainties have been studied for the signal and the background. For the SM ZZ^* background, which is estimated from MC simulation.

- **QCD scale ($\Lambda_{\mathbf{QCD}}$) uncertainty**: the QCD scale uncertainties for the $m_H = 125$ GeV amount to $^{+7\%}_{-8\%}$ for the ggF process, $\pm 1\%$ for the VBF and WH/ZH processes, and $^{+4\%}_{-9\%}$ for the $t\bar{t}H$ process [7].

- **Parton density functions (PDFs) and α_s uncertainty**: the uncertainties related to the parton distribution functions amount to $\pm 8\%$ [7] for the predominantly gluon-initiated ggF and $t\bar{t}H$ processes, and $\pm 4\%$ [7] for the predominantly quark-initiated VBF and WH/ZH processes (Figure 1.5).

- **Uncertainty of the $H \to ZZ^*$ branching ratio**: the uncertainties on the predicted branching ratios amount to $\pm 5\%$ [7].

4.4 ATLAS Open Data code

The release of the 13 TeV ATLAS Open Data is accompanied by a set of Jupyter notebooks (open-source web application for sharing documents containing live codes, equations, visualizations and narrative text) that allow data analysis to be performed directly in a web browser either online or offline by downloading all the data needed locally [64].

So, we worked locally with a Python code given open access at the CERN ATLAS Open Data website `https://atlas.cern/resources/opendata`, that allows to rediscover the Higgs boson in the channel $H \to ZZ^* \to 4l$. A number of Python tools are needed to help us:

- **uproot:** lets us read ".root" files typically used in particle physics by converting them into data formats used in Python.

- **pandas:** lets us store data as dataframes, a format widely used in Python.

- **numpy:** provides numerical calculations such as histogramming.

- **matplotlib:** common tool for making plots, figures, images, visualisations.

However, we did not settle only for the result provided, but we made our own modified and improved version of the initial notebook, in order to obtain additional results. So instead of only one histogram plot of the four-lepton invariant mass as an output, we added four other different manipulations on data enabling us to do a deeper and wider analysis plus more details in the other outputs. This will be discussed more in the next section.

4.5 Statistical reconstruction of the Higgs signal

First level : statistical histograms reconstruction

The selection criteria presented in this chapter are applied to all of the 2016 data of proton-proton collisions at center-of-mass energy $\sqrt{s} = 13$ TeV with an integrated luminosity of $10 fb^{-1}$.

The Figure 4.2 displays the steps of reconstructing the expected distributions of the four-leptons invariant mass m_{4l} for the background and for a Higgs boson signal with $m_H = 125$ GeV compared to the data. Plot (a) consists of the observed Higgs boson candidates (events that pass selection). These experimental data are represented by black dots. Plot (b) represents the expected background contribution, whereas plot (c) is the Higgs signal expectation for a mass around $m_H = 125$ GeV. Plot (d) is the superposition of all the three previous plots. The red histogram represents the expected background for the ZZ^* processes and the purple one represents the reducible Z and $t\bar{t}$ backgrounds.

The plot shows a peak in the low mass region for ZZ^*. Since the Z^* is too small, that peak corresponds to the $Z \to 4l$ production around $m_{4l} = M_Z = 91$ GeV. We can also notice the threshold above $m_{4l} = 2M_Z \simeq 180$ GeV of the on-shell ZZ production, and a narrow peak around $m_{4l} = m_H = 125$ GeV that actually fits with the observed data (excess of events bigger than background).

These plots were made by calculating the four-lepton invariant mass m_{4l} for the selected events, which then was plotted according to the number of events observed and/or expected in the mass range 80-250 GeV, with a step of 5 GeV. This output was given after running our code to calculate the four-lepton mass from experimental and simulated (background and signal) data samples:

$$m_{4l} = \sqrt{E^2 - p_x^2 - p_y^2 - p_z^2} \tag{4.1}$$

with p_x, p_y, p_z being the components of the momentum of the four-lepton system and E the four-lepton energy. We point out that the observables needed are taken directly from the data samples. They are gathered in sets of four selected leptons, and we take the transverse momentum p_T, pseudorapidity η, azimuthal angle ϕ and energy E of each lepton of the quadruplet. An overview of the function used in the code is shown in Figure 4.1:

```
Entrée [11]: def calc_mllll(lep_pt,lep_eta,lep_phi,lep_E):
                 # first lepton is [0], 2nd lepton is [1] etc
                 px_0 = lep_pt[0]*math.cos(lep_phi[0]) # x-component of lep[0] momentum
                 py_0 = lep_pt[0]*math.sin(lep_phi[0]) # y-component of lep[0] momentum
                 pz_0 = lep_pt[0]*math.sinh(lep_eta[0]) # z-component of lep[0] momentum
                 px_1 = lep_pt[1]*math.cos(lep_phi[1]) # x-component of lep[1] momentum
                 py_1 = lep_pt[1]*math.sin(lep_phi[1]) # y-component of lep[1] momentum
                 pz_1 = lep_pt[1]*math.sinh(lep_eta[1]) # z-component of lep[1] momentum
                 px_2 = lep_pt[2]*math.cos(lep_phi[2]) # x-component of lep[2] momentum
                 py_2 = lep_pt[2]*math.sin(lep_phi[2]) # y-component of lep[2] momentum
                 pz_2 = lep_pt[2]*math.sinh(lep_eta[2]) # z-component of lep[3] momentum
                 px_3 = lep_pt[3]*math.cos(lep_phi[3]) # x-component of lep[3] momentum
                 py_3 = lep_pt[3]*math.sin(lep_phi[3]) # y-component of lep[3] momentum
                 pz_3 = lep_pt[3]*math.sinh(lep_eta[3]) # z-component of lep[3] momentum
                 sumpx = px_0 + px_1 + px_2 + px_3 # x-component of 4-lepton momentum
                 sumpy = py_0 + py_1 + py_2 + py_3 # y-component of 4-lepton momentum
                 sumpz = pz_0 + pz_1 + pz_2 + pz_3 # z-component of 4-lepton momentum
                 sumE = lep_E[0] + lep_E[1] + lep_E[2] + lep_E[3] # energy of 4-lepton system
                 return math.sqrt(sumE**2 - sumpx**2 - sumpy**2 - sumpz**2)/1000 #/1000 to go from MeV to GeV
```

Figure 4.1: The function that calculates the four-lepton invariant mass m_{4l} (mllll) in the ATLAS Open Data code.

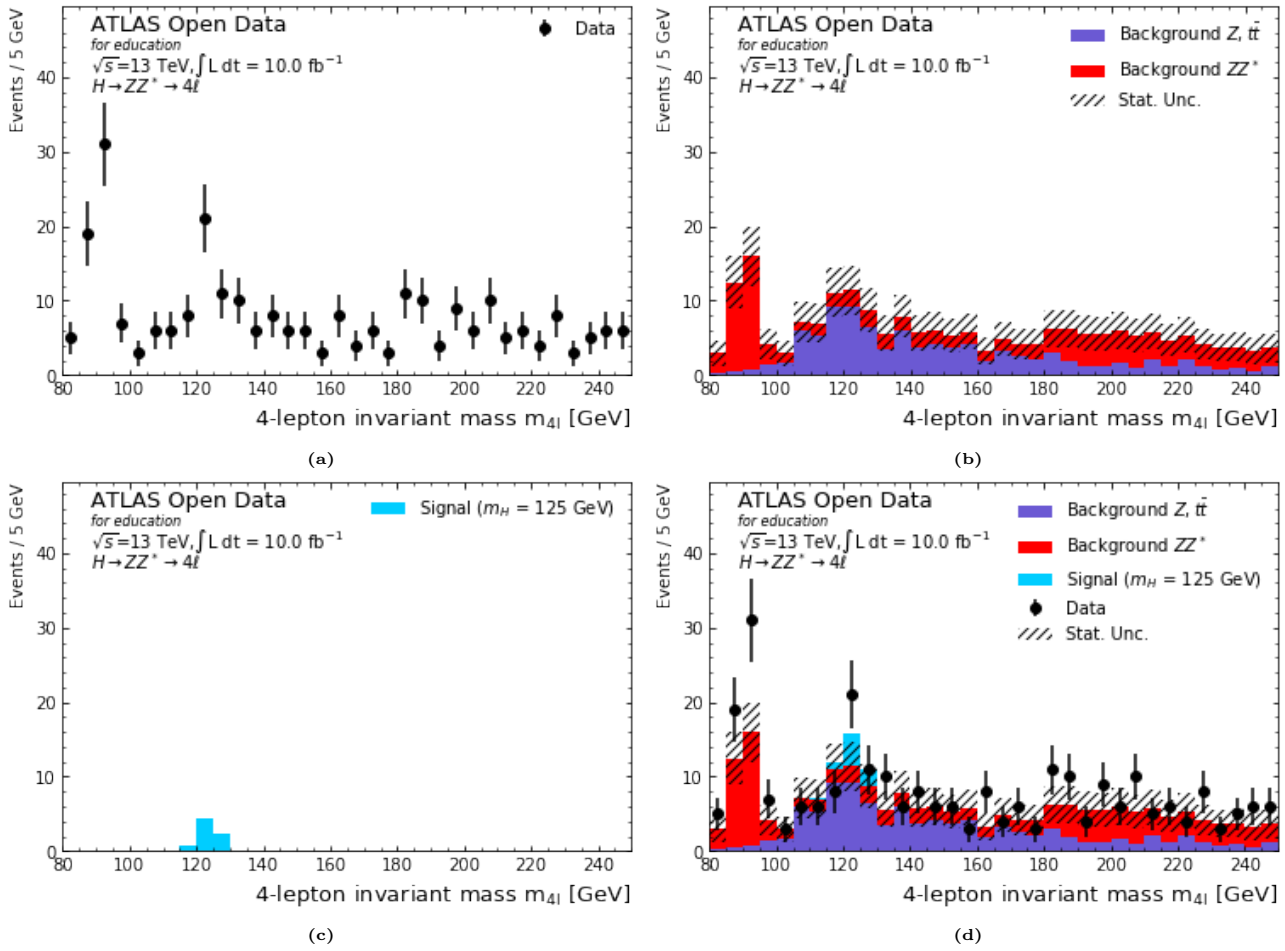

Figure 4.2: Distribution of four-lepton m_{4l} invariant mass by steps: **(a)** experimental data, **(b)** background expectation, **(c)** signal expectation, **(d)** data fitted with background and signal expectations.

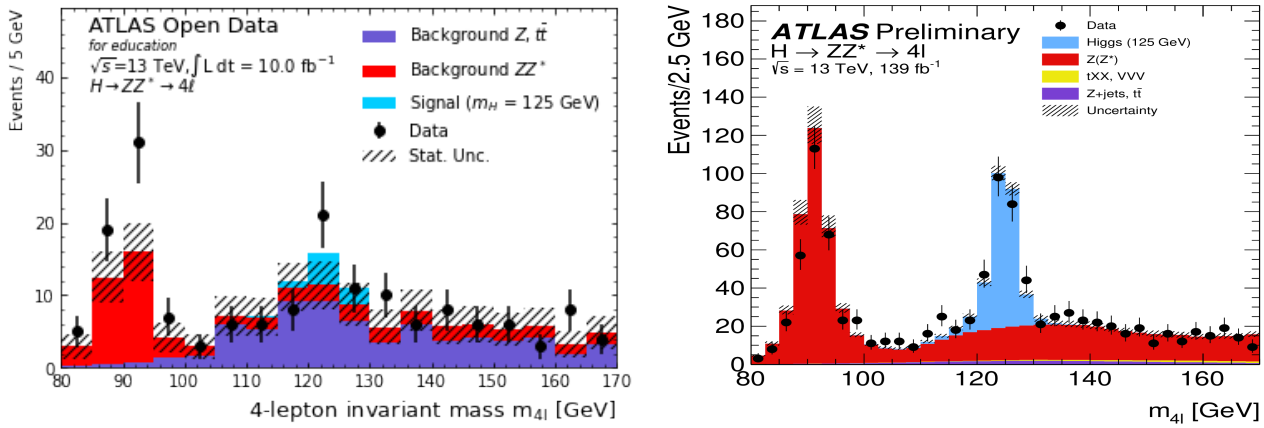

Our finding with $10 fb^{-1}$.

CERN finding $139 fb^{-1}$ (2020) [65].

Figure 4.3: The distribution of the four-lepton invariant mass m_{4l}, for the selected candidates, compared to the expected signal and background contributions for the $\sqrt{s} = 13$ TeV.

The Figure 4.3 shows our output of the four-lepton invariant mass distribution (on the left), next to the most recent ATLAS plot of 2020 (on the right).
We notice a considerable difference in the precision of the two graphs. Experimental data points (black dots) fit way better in the 2020 plot. This is mainly due to the higher integrated luminosity of 139 fb^{-1} (larger number of events).

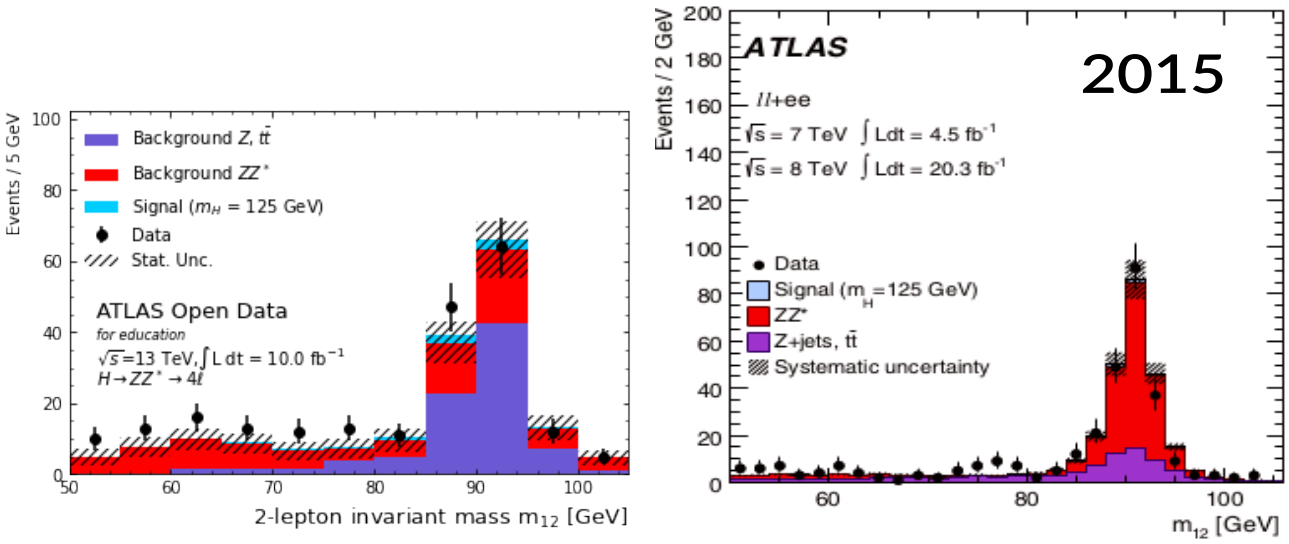

Our finding. CERN finding (2015) [66].

Figure 4.4: Invariant mass distribution of the leading lepton pair (m_{12}).

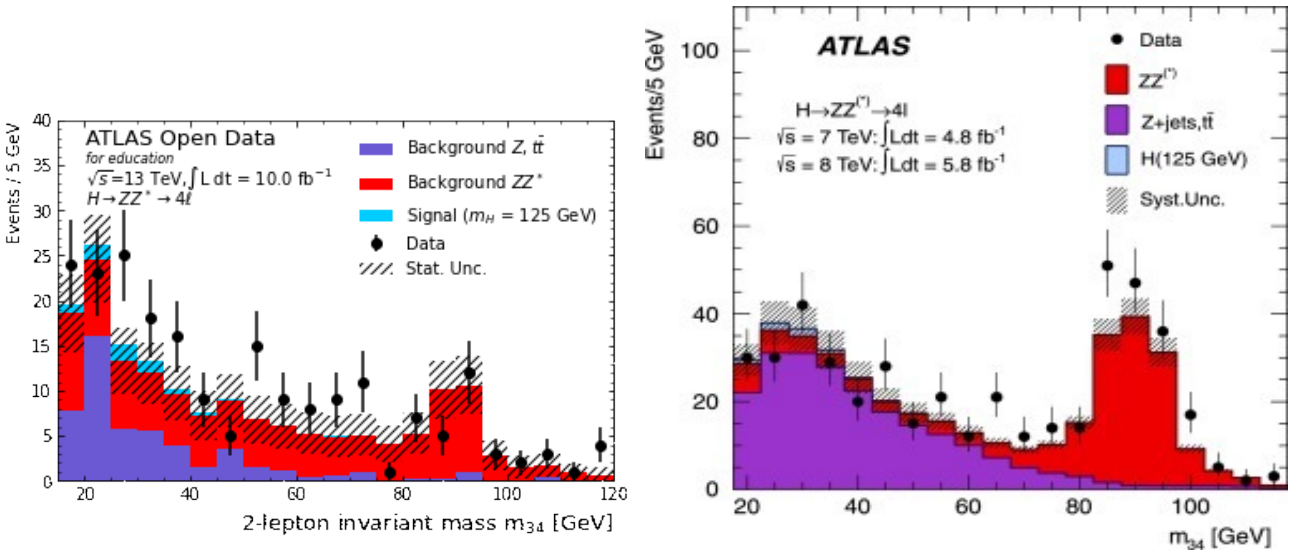

Our finding. CERN finding (2012) [7].

Figure 4.5: Invariant mass distribution of the sub-leading lepton pair (m_{34}).

As for Figure 4.4 and 4.5, they each show the leading and sub-leading leptons mass distribution m_{12} and m_{34} respectively. Our findings (on the left) were made by means of some

modifications to the code. The main idea is defining functions that calculate m_{12} and m_{34}, determined by applying cuts to the leptons selected.

Figure 4.6 shows the distribution of the m_{12} versus m_{34} invariant masses for the selected candidates in the mass range $120 < m_{4l} < 130$ GeV. Where black triangles represent data, the Higgs signal with $m_H = 125$ GeV is represented in blue and it is superimposed on the Z and $t\bar{t}$ background (red) and ZZ^* background (orange).

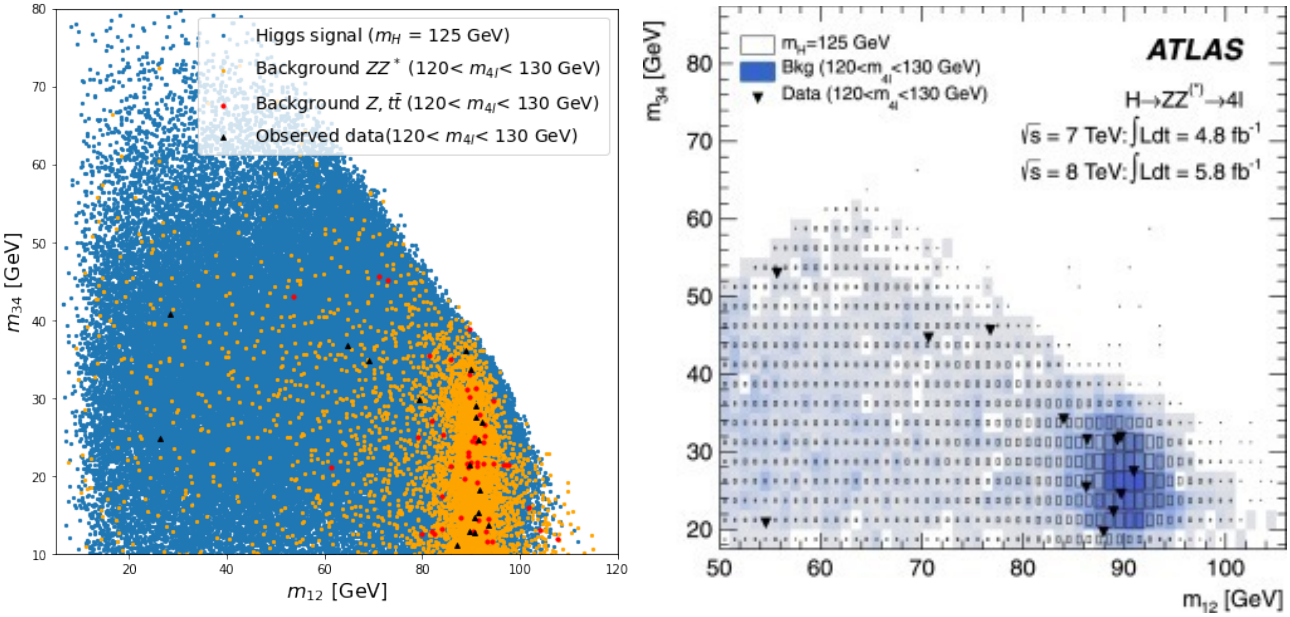

Our finding. CERN finding (2012) [7].

Figure 4.6: Distribution of the m_{34} versus the m_{12} invariant mass.

Second level : statistical precision p-value analysis

For data analysis in High Energy Physics (HEP), precision statistical procedures [67–71] are important in order to exclude or discover a new phenomenon. It determines whether or not the observed data are compatible with a given hypothesis and to determine a degree of incompatibility.

So there are two nested hypotheses tested against each other. The Standard Model (denoted by **b** for background) and the Standard Model containing a Higgs boson with a mass m_H, i.e. the signal+background denoted by $\mathbf{s(m_H) + b}$. To establish a discovery we define the **null hypothesis** as the background only hypothesis noted $H_{null} = H_0$, and test it. We either fail to reject it or manage to reject it in favour of the **alternative hypothesis** noted $H_{alt} = H_1$. Rejection of the null hypothesis H_0 at the level of $\mathbf{5}\sigma$ is considered a discovery. This means that only one background experience could fluctuate and sound like that same excess signal among the billions of colision data are summed up into a single digit that determines whether

the LHC rejected the background only hypothesis in favor of the Higgs boson mass m_H or not. Exclusion of a certain hypothesis requires at least a 95% confidence level (CL) when CL_s (see (A.32)) is less than 5%.

For statistical procedures, we use the frequentist approach. The Bayesian approach is used as a check to set the exclusion limits and the probabilities quantify the degree of confidence in a hypothesis. The frequentist approach begins by defining a statistical test, q_μ, the purpose of which is to quantify the agreement between the observed data and the predictions. It is usual to look at the parameter μ which determines the strength of the $H \to ZZ^* \to 4l$ process and simply called signal strength. This parameter is defined as $\mu = \sigma_{obs}/\sigma_{SM}$, where σ_{SM} is the cross section of the calculated Standard Model. Signal strength is defined so that $\mu = 0$ corresponds to the background-only hypothesis and $\mu = 1$ corresponds to the Standard Model Higgs boson in addition to the background hypothesis. Test statistics for discovery or exclusion are generally based on the **profile likelihood ratio** $\lambda(\mu)$. The two most common test statistics in high energy physics are **Neyman-Pearson** (see Appendix A.3.2) and **Profile Likelihood**.

Likelihood function

The data are available in form of a binned histogram. In most of the cases, each bin content is independent of any other bin and all obey Poisson distributions, assuming that bins contain event-counting information. The likelihood function can be written as a product of Poissonian pdfs (probability density functions) corresponding to each bin. Whose number of event is given by n_i. The expected number of events from signal and background in each bin depends on some unknown parameters: $\mu_i = \mu_i(\theta_1, ..., \theta_m)$. The function to be minimized, in order to fit $\theta_1, ..., \theta_m$, is the following:

$$-2\ln L(\vec{n}, \vec{\theta}) = -2\ln \prod_{i=1}^{n_{bins}} Poiss(n_i; \mu_i(\theta_1, ...\theta_m)) \tag{4.2}$$

$$= -2\sum_{i=1}^{n_{bins}} \ln \frac{e^{-\mu_i(\theta_1,...\theta_m)}\mu_i(\theta_1, ...\theta_m)^{n_i}}{n_i!} \tag{4.3}$$

$$= 2\sum_{i=1}^{n_{bins}} (\mu_i(\theta_1, ...\theta_m) - n_i \ln \mu_i(\theta_1, ...\theta_m) + \ln n_i!) \tag{4.4}$$

The expected number of event in each bin, μ_i, is often approximated by a continuous function $\mu(x)$ evaluated at the center of the bin $x = x_i$. The parameters of the pdf which are not interesting are called nuisance parameters and are used to evaluate the impact of the systematic uncertainties on the measurement of the parameters of interest.

The distribution of the number of events in each bin can be approximated, for sufficiently large number of events, by a Gaussian with standard deviation equal to $\sigma = \sqrt{n_i}$. Then the

probability of the dataset is the product of the probabilities of each bin:

$$P \propto \prod_{i=1}^{n_{bins}} \frac{1}{\sqrt{2\pi\sigma^2}} \left\{ \exp\left[-\frac{1}{2} \left(\frac{n_i - \mu(x_i; \theta_1, ...\theta_m)}{\sigma} \right)^2 \right] \right\} \tag{4.5}$$

Maximizing (4.5) is equivalent to minimizing the negative of its logarithm, and the term $\frac{1}{\sqrt{2\pi\sigma^2}}$ does not depend on the parameters θ if the uncertainties σ are known and fixed, hence it is a constant that we can drop when performing the minimization. So that the maximum likelihood estimate of the model parameters is obtained by minimizing the quantity:

$$\chi^2 = \left[\sum_{i=1}^{n_{bins}} \frac{(n_i - \mu(x_i; \theta_1, ...\theta_m))^2}{\sigma^2} \right] \tag{4.6}$$

called the **chi-squared** χ^2. What we see is that chi-squared fitting is a **maximum likelihood estimation** of the fitted parameters if the measurement errors are independent and normally distributed with constant standard deviation. So the idea is to minimize the mean difference between the observed and expected values.

We use likelihood ratio by dividing the likelihood function from equation (4.9) over its maximum value, which we obtain replacing μ_i with n_i. Hence, we obtain:

$$\lambda = -2ln \frac{L(n_i; \mu_i(\theta_1, ...\theta_m))}{L(n_i; n_i)} = -2ln \frac{e^{-\mu_i} \mu_i^{n_i}}{n_i!} \frac{n_i!}{e^{-n_i} n_i^{n_i}} \tag{4.7}$$

$$= 2 \sum_i \left[\mu_i(\theta_1, ...\theta_m) - n_i + n_i \ln \left(\frac{n_i}{\mu_i(\theta_1, ...\theta_m)} \right) \right] \tag{4.8}$$

the distribution of λ can be used to determine a *p-value*. The profiled likelihood is always normalised to its maximum value given by the maximum likelihood (ML) estimator, which is called **profile likelihood ratio**.

Now we choose a bin represented by the yellow band (Figure 4.7) and we apply the counting to it, where every bin is in fact a counting experiment. We assume it follows a Poisson distribution with mean $\mu_s + \mu_b$:

$$P(n|\mu_s, \mu_b) = \frac{(\mu_s + \mu_b)^n}{n!} e^{-(\mu_s + \mu_b)} \tag{4.9}$$

where the n is the number of events, μ_s and μ_b are the expected number of events from the signal and background, respectively. To establish the existence of the signal process, we test the hypothesis of $\mu_s = 0$ (the background-only hypothesis) against the alternative where the

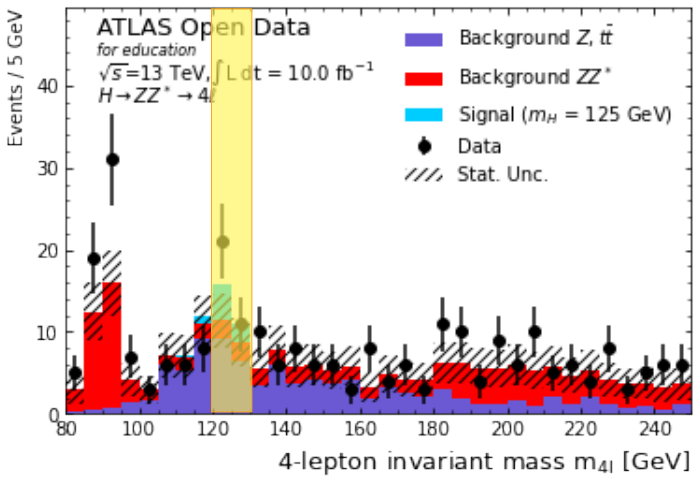

Figure 4.7: The distribution of the four-lepton invariant mass m_{4l} for the selected candidates.

signal exists, that is, $\mu_s > 0$. From (4.9), we construct the profile likelihood ratio:

$$\lambda(0) = \frac{P(n|0,\mu_b)}{P(n|\hat{\mu}_s,\mu_b)} = \left(\frac{\mu_b}{\hat{\mu}_s+\mu_b}\right)^n e^{\hat{\mu}_s} = \left(\frac{\mu_b}{n}\right)^n e^{n-\mu_b} \tag{4.10}$$

$$\boxed{\lambda(0) = \left(\frac{20}{32}\right)^{32} \mathrm{e}^{32-20} = 0.047} \tag{4.11}$$

where $\hat{\mu_s} = n - \mu_b$ is the maximum likelihood estimator of μ_s given that we observe n events in the selection region.
The hypothesis testing performed in the analysis in this Chapter are based on the **profile likelihood ratio**.

The test statistic q_0 for discovery of a positive signal

The test statistic q_μ with $\mu = 0$ is commonly exploited to test against the background-only hypothesis, Where the rejecting the $\mu = 0$ hypothesis effectively leads to the discovery of a new signal.The test statistic can be defined as:

$$q_0 = \begin{cases} -2\ln\lambda(0) & if \quad n > \mu_b \\ 0 & \text{otherwise.} \end{cases} \tag{4.12}$$

$$\boxed{q_0 = 6.080} \tag{4.13}$$

where $\lambda(0)$ is the profile likelihood ratio for $\mu = 0$, as defined in (4.10).

Asymptotically, a test statistic $-2\ln\lambda$ of one parameter of interest μ is distributed as a χ^2

distribution with one degree of freedom. The test statistic q_0, i.e equation (A.31) for $\mu = 0$, may lead to the rejection of the null hypothesis in case of both an upward and a downward fluctuation of the observed data. This is appropriate if the presence of a new phenomenon could lead to an increase or decrease in the number of events found.
If the data fluctuate such that one finds fewer events than even predicted by background processes alone, then one has $q_0 = 0$. Large values of q_0, corresponding to an increasing level of incompatibility between the dataset and the background-only hypothesis. This statistical test is used to calculate the probability (p_0, with $\mu = 0$) that the background can vary to produce an excess at least as large as that observed in the data.

p-value

Assumed an observed data sample, claiming the discovery of a new signal requires to determine that the sample is sufficiently incompatible with the hypothesis that only background (H_0) is present in the data. A test statistic can be used to measure how agreeing or disagreeing the observation is with the hypothesis of the presence of background only.

To quantify the level of disagreement between the observed data and the hypothesis of $\mu = 0$ using the observed value of q_0, we compute the $\mathbf{p-value}$. It is the probability, under postulation of the **null hypothesis** H_{null}, of finding data of equal or greater incompatibility with the predictions of H_{null}. This can be illustrated in Figure 4.8 of the profile likelihood test statistic by the light blue area. Here H_0 is the tested null hypothesis (background-only) and the $p-value$ is given by:

$$p_0 = \int_{q_{\mu=0,obs}}^{\infty} f(q_0|0)dq_0. \tag{4.14}$$

$$\boxed{p_0 = 0.013} \tag{4.15}$$

Where $q_{\mu=0,obs}$ is the value of the statistical test observed by the experiment, and the rejection of the theory of the non-signal, μ takes the value of 0. Here $f(q|0)$ denotes the pdf of the statistic q_0 under assumption of the background-only ($\mu = 0$) hypothesis. There is a probability interpretation of the $p-value$: This statistical quantity expresses how likely the number of observed events would be due only to background processes. We can also write $p-value$ of the hypothesized $\mu = 0$ in the form:

$$p = 1 - \Phi(\sqrt{q_0}) \tag{4.16}$$

where Φ is the standard Gaussian cumulative distribution.

In particle physics, when performing searches, the $p-value$ is generally converted into the

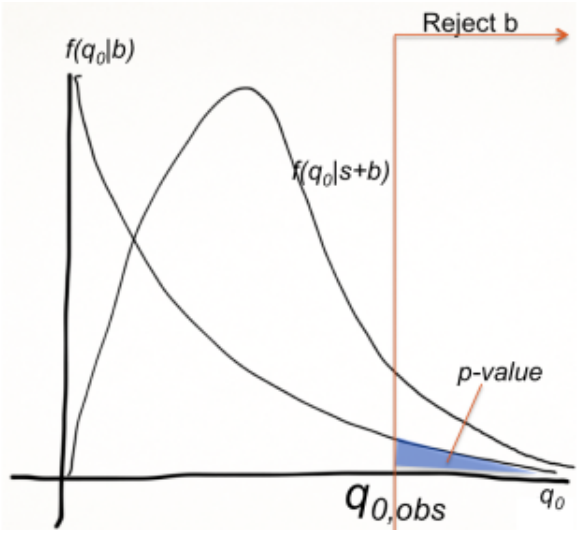

Figure 4.8: The pdf of the Profile-Likelihood, q_0 test statistics, under the null (b) and alternative (s+b) hypotheses.

equivalent significance **Z** defined as a Gaussian distributed variable, which is found Z standard deviations above its mean, has an upper-tail probability equal to **p** (Figure 4.9). That is:

$$Z = \Phi^{-1}(1 - p) \tag{4.17}$$

where p is the $p - value$ and Φ^{-1} is the standard normal quantile. Equation (4.16) and (4.17) lead therefore to the simple result:

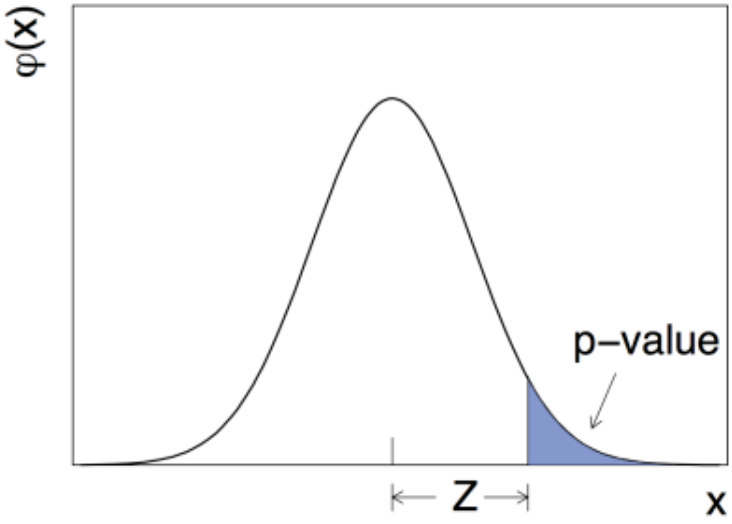

Figure 4.9: The relationship between a $p - value$ and a significance of Z sigma.

$$Z = \sqrt{q_0} = \sqrt{2\left(n \ln\left(\frac{n}{\mu_b}\right) - n + \mu_b\right)} \tag{4.18}$$

$$\boxed{Z = 2.465} \tag{4.19}$$

The quantity Z measures the statistical significance in units of standard deviations or sigmas σ. Often in particle physics, a significance of at least $Z = 5$ (a five-sigma effect (5σ)) is regarded as sufficient to claim a discovery. This corresponds to $p = 2.87 \times 10^{-7}$.

For purposes of excluding the signal hypothesis, a threshold $p - value$ of $\alpha = 0.05$ (i.e., 95% confidence level) is often used, which corresponds to $Z = 1.64$. And since our result is $p = 0.013 < \alpha$ and $Z = 2.465$ to correspend for a 2.5σ (i.e. 99.30% confidence level), this numerical p-value that we obtained still confirm a Higgs mass for around $M_H = 125$ GeV.

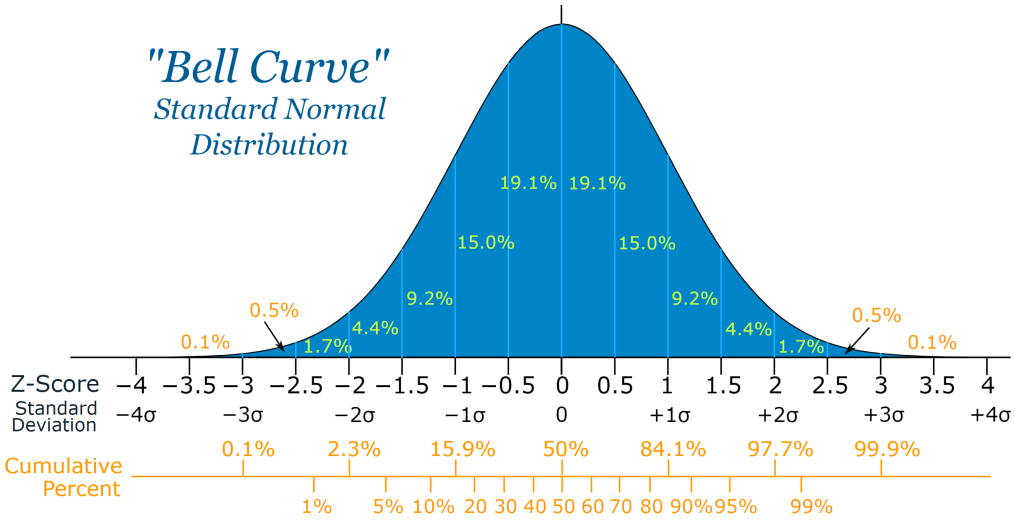

Figure 4.10: Bell curve of the Standard Normal Distribution [72].

The significance of an excess in the data is first quantified with the local p_0, where the 0 corresponds to the value of μ, which implies the purely background model. So this is the probability that the background fluctuates extremely, or more extreme than what we observed in the data. Thus, if p_0 is very low, then it is very unlikely that the local fluctuation is due to background, it is therefore from the signal. By using the p_0 defined in the formula (4.14), the observed $p-value$ is shown as a function of the Higgs mass m_H in Figure 4.11. From the left plot, it is observed that the local minimum of $p_0 = 2.9 \times 10^{-3}$ lies at $m_H = 121 GeV$, corresponding to a statistical significance of 2.76σ. This result rejects the background-only theory in the $H \to ZZ^* \to 4l$ channel. And the right plot obtained from the result of the $H \to ZZ^* \to 4l$ analysis using the full $\sqrt{s} = 7$ TeV and $\sqrt{s} = 8$ TeV statistics, when combained the result, the local minimum of $p_0 = 10^{-4}$, corresponding to 3.6σ. where we conclude, that the result of the

statistical quantity published by the ATLAS collaboration, remains more precise than what we obtained.

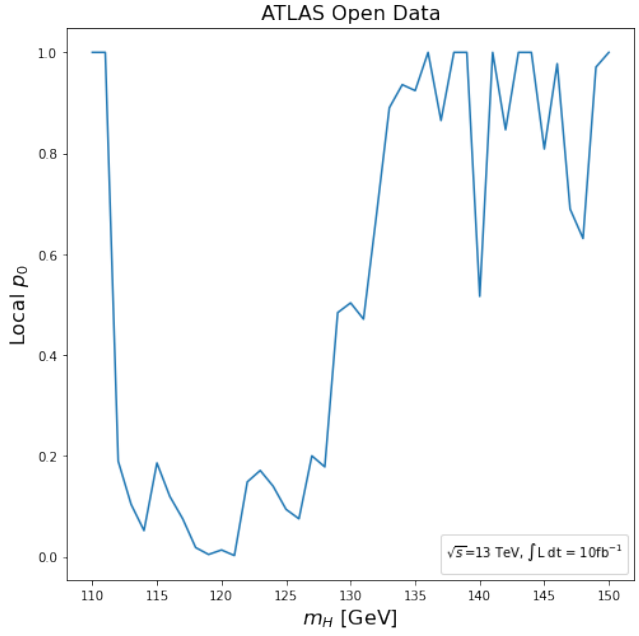

Our finding.

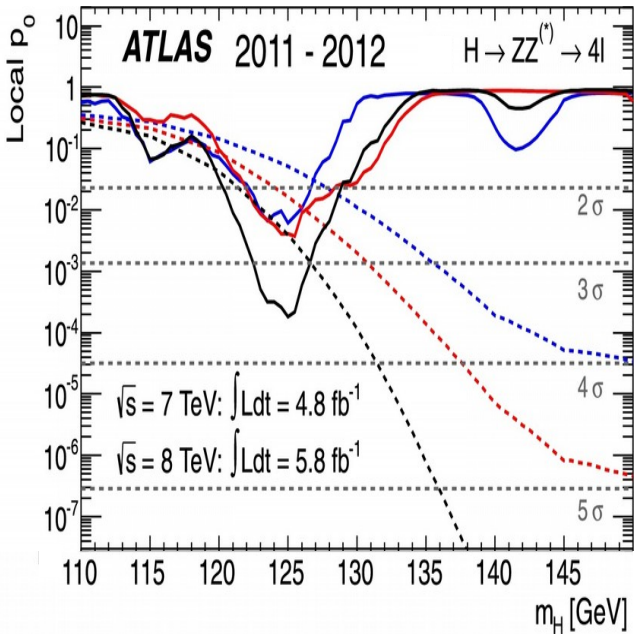

CERN finding [7].

Figure 4.11: Local p_0 value as a function of m_H.

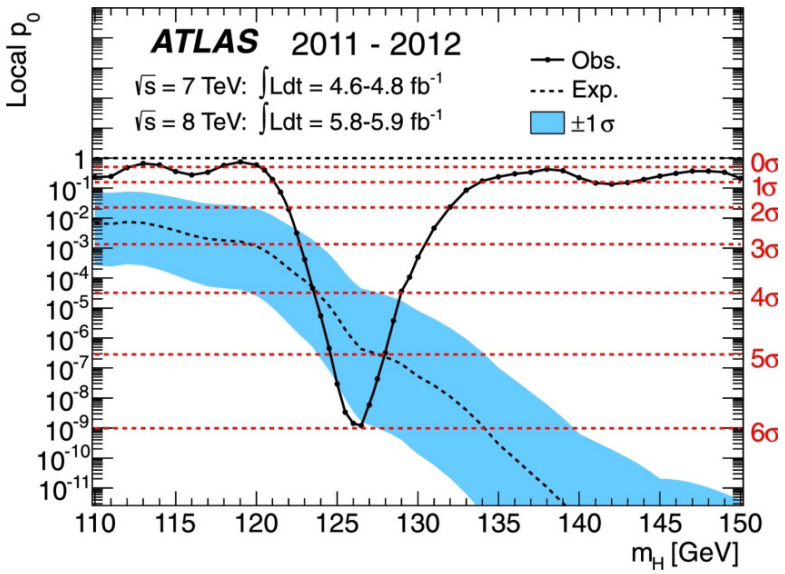

Figure 4.12: Plot of the observed (solid lines) and expected (dashed lines) local p_0-values as a function of the Higgs boson mass. The values of the expected p_0-value are obtained assuming the existence of a Standard Model Higgs boson signal for that mass [7].

The Figure 4.12 shows the combination of the results of the $H \to \gamma\gamma$, $H \to ZZ^* \to 4l$ and $H \to W^+W^- \to l\nu l\nu$ channel, various Higgs boson searches of the ATLAS experiment in

July 2012. An excess of events was around $m_H = 125$ GeV, with a local significance of 6σ, corresponding to $p_0 = 1.7 \times 10^{-9}$. A similar excess was also observed by the CMS experiment who worked in parallel with ATLAS at the LHC.
So this was the final discovery plot of July 2012, with a p-value over the 5-sigma discovery criteria. So, a p-value of 1σ means we have a 1 in 10 chance the signal isn't the Higgs. 3σ means 1 in 1000 chance it isn't a Higgs, this is considered an evidence. 6σ means 1 in a billion chance it is not a Higgs and is only due to background fluctuations. This makes it a real discovery.

Conclusion

In this master thesis, we were interested in reconstructing the Higgs signal from the ATLAS experiment open data at the LHC, through the $pp \to H \to ZZ^* \to 4$ leptons decay channel.

In a first step, we experienced the strengh and the elegance of the Higgs mechanism in generating masses of scalar, vector and fermion Standard Model particles. Then we examined more deepely the Standard Model Feynman rules associated to the Higgs field, to identify the most involved processes in the creation and decay of the Higgs particle in the proton proton collisions at the LHC.

Then, in order to test this theoretical background concretely in the experimental field, we paid attention to the design and making of the Large Hadron Collider with a special interest in the ATLAS detector and data acquisition. Furthermore, we expressed the theory into a manageable form, by simulating the whole collision process that produces the Higgs boson in the golden channel taking place at the LHC. In this simulation, we also took into consideration the background processes that produce the same four leptons final state as the Higgs boson.

Finally, we explored available experimental and simulated data from the ATLAS Open Data portal. We then applied kinematical cuts to these data, to highlight the four leptons Higgs signal in contrast with background events. After that, in a first level statistical analysis, we plotted histograms of the observed data and of the simulated background and Higgs signal. This allowed us to notice that for $M_H = 125$ GeV, the simulated events fit with the observed ones when we jointly take into account the Higgs signal and the background. As for the following step, we relied on a more precise statistical analysis. It consisted in calculating the p-value for various hypothetical Higgs masses. This statistical quantity expresses how likely the number of observed events would be due only to background processes. Although less precise than that published by the ATLAS collaboration, the numerical p-values that we obtained still confirm a Higgs mass for around $M_H = 125$ GeV.

In the end, now that the Standard Model is completed, the relationship between the theory and experiment through data analysis will still help in the search for greater hints to physics beyond the Standard Model. Hence, more precise computations and measurements are needed to explore rare events and look for any potential heavier particles.

Appendix A

Statistical methods for High Energy Physics

A.1 Bayes theorem

Bayes theorem is a basic result in probability theory, it is used to update the estimates of any probability or parameter, based on the observations and the probability laws of those observations. It allows to determine a conditional probability that of A knowing B. It can be derived easily from the definition of conditional probability:

$$P(A|B) = \frac{P(A \cap B)}{P(B)} \tag{A.1}$$

Considering two events A and B, by using equation (A.1) twice we can write:

$$P(A|B) = \frac{P(A \cap B)}{P(B)} \tag{A.2}$$

$$P(B|A) = \frac{P(A \cap B)}{P(A)} \tag{A.3}$$

from which the following equation derives:

$$P(A|B)P(B) = P(B \cap A)P(A) \tag{A.4}$$

according to (A.4), the Bayes theorem can be written in the form:

$$\boxed{P(A|B) = \frac{P(B|A)P(A)}{P(B)}} \tag{A.5}$$

In equation (A.5), $P(A)$ has the role of prior probability and $P(A|B)$ has the role of posterior probability

$$P(H|E) = \frac{P(E|H)P(H)}{P(E)} \tag{A.6}$$

A.1.1 Bayesian Probability

Bayesian Probability makes great use of Bayes Theorem, in the form:

$$P(Theory|Data) = \frac{P(Data|Theory)}{P(Data)} \times P(Theory) \tag{A.7}$$

$P(Theory)$ is called the prior, $P(Data|Theory)$ is the Likelihood: the probability of getting Data if Theory is true. $P(Theory|Data)$ is the Posterior.

A.2 The Likelihood function

The Likelihood function is a function of the parameters of a statistical model calculated from observed data. The result of an experiment can be modeled as a set of random variables $x_1.....x_n$, whose distribution takes into account both the effects of the detector and the theory, which can be described according to certain parameters $\theta_1.....\theta_m$ whose values are unknown.

$$L = f(x_1..., x_n; \theta_1..., \theta_m) \tag{A.8}$$

In case our sample consists of N independent measurements, typically each corresponding to a collision event, the likelihood function can be written as:

$$L = \prod_{i=1}^{N} f(x_1^i..., x_n^i; \theta_1..., \theta_m) \tag{A.9}$$

For example :
The number $P(data|theory)$ of the equation is now generalised to the function $L(a, x)$, where x is the observed value of the data.
The probability of getting x counts from a Poisson process with mean a:

$$P(x, a) = \exp^{-a} \frac{a^x}{x!} \tag{A.10}$$

We also write:

$$L(a, x) = \exp^{-a} \frac{a^x}{x!} \tag{A.11}$$

These are identical joint functions of two variables (x and a) to which we have just happened to have given different names. The equation (A.10) as describing the probability of getting various different x from some fixed a, whereas equation (A.11) describes the likelihood for various different a from some given x.

* If $P(x_1, a) > P(x_2, a)$ then x_1 is more probable than x_2.
* If $L(a_1, x) > L(a_2, x)$ it does not mean that a_1 is more likely than a_2 .

A.2.1 Maximum likelihood estimates

The maximum likelihood estimate is a statistical estimator used to infer the parameters of the probability distribution of a given sample, by finding the values of the parameters maximizing the likelihood function. And to maximize the Likelihood function, a numerical treatment is needed in most of the realistic cases.

Extended likelihood function

The likelihood function expresses the probability density of a sample as a function of the unknown parameters $\theta_1, ..., \theta_m$ given a sample of the N measures of the variables $\vec{x} = (x_1, ..., x_n)$

$$L(\vec{x_1}, ..., \vec{x_N}) = \prod_{i=1}^{N} f(x_1^i, ..., x_n^i; \theta_1, ...; \theta_m) \tag{A.12}$$

The size N of the sample is a random variable. In those cases, the extended likelihood function can be defined as:

$$L(\vec{x_1}, ..., \vec{x_N}) = P(N, \theta_1, ..., \theta_m) \prod_{i=1}^{N} f(x_1^i, .., x_n^i; \theta_1, ..., \theta_m) \tag{A.13}$$

where $P(N, \theta_1, ..., \theta_m)$ is the distribution of N, and in practice is always a Poissonian whose expected rate parameter is a function of the unknown parameters $\theta_1, ..., \theta_m$:

$$P(N; \theta_1, ..., \theta_m) = \frac{\nu(\theta_1, ..., \theta_m)^N \exp^{-\nu(\theta_1, ..., \theta_m)}}{N!} \tag{A.14}$$

$-\log L$ or $-2\log L$ can be used in numerical treatment rather than L either with a standard or an extended likelihood function, because the product of the different terms is transformed into the sum of the logarithms of these terms.
For a Poissonian process that is given by the sum of a signal plus a background process. The

extended likelihood function may be written as:

$$L(\vec{x}; s, s, b, \vec{\theta}) = \frac{(s+b)^N \exp^{-(s+b)}}{N!} \prod_{i=1}^{N} (f_s P_s(x_i; \vec{\theta}) + f_b P_b(x_i, \vec{\theta})) \tag{A.15}$$

where s represents the signal and b the background, f_s and f_b are the fraction of signal and background events, namely:

$$f_s = \frac{s}{s+b} \tag{A.16}$$

$$f_b = \frac{b}{s+b} \tag{A.17}$$

and P_s and P_b are the pdf of the variable x for signal and background, respectively. Replacing f_s and f_b into (A.15) gives:

$$L(\vec{x}; s, b, \vec{\theta}) = \frac{\exp^{-(s+b)}}{N!} \prod_{i=1}^{N} (s P_s(x_i; \vec{\theta}) + b P_b(x_i; \vec{\theta})) \tag{A.18}$$

We use negative logarithm of equation (A.18). That should be minimized in order to determine the best-fit values of s, b and θ:

$$-\ln L(\vec{x}; s, b, \vec{\theta}) = s + b - \sum_{i=1}^{N} \ln \left(s P_s(x_i; \vec{\theta} + b P_b(x_i; \vec{\theta}) \right) + \ln N! \tag{A.19}$$

$\ln N!$ is a constant which can be omitted in the minimization. And the signal strength μ can be used instead of s as the parameter of interest, defined by the following equation:

$$s = \mu s_0 \tag{A.20}$$

Where s_0 is the theory prediction for the signal yield s. $\mu = 1$ corresponds to the nominal value of the theory prediction for the signal yield.

A.3 Hypothesis tests

A hypothesis test is done by comparing some of the observed data samples, which are either more compatible with one theoretical model or another alternative model. Hypothesis tests are used to determine the results of the lead to the rejection of the null hypothesis of predetermined level of significance.

In the test, there are two nested hypotheses tested against each other: null hypothesis H_0 denoted by the background only b and alternative hypothesis H_1 denoted by the background+signal. A test statistic is a variable calculated from of our data sample which has a discriminating power

between two hypotheses H_1 and H_0. We can take as a signal sample all the events whose value of x is greater than a threshold $x > x_{cut}$. x is an example of a test statistic used to discriminate the two hypotheses H_1 = signal and H_0 = background.

The most important steps that can be taken to get a test:
_ We set the null hypothesis H_0 and the alternative hypothesis H_1.
_ The significance level α, as the probability to reject the hypothesis H_0 if it is true (error of the first kind). Hence the selection efficiency for the signal corresponds to $1 - \alpha$.
_ The misidentification probability β, as the probability to reject the hypothesis H_1 if it is true. The case of rejecting H_1 if true is called error of second kind. $1 - \beta$ is also called power of the test.
_ We conclude whether or not the null hypothesis is rejected according to the result of the comparison of the value of the probability p-value to the threshold risk α:

* If $p_{value} \leq 0.05$ is statistically significant. It indicates strong evidence against the null hypothesis, as there is less than a 5% probability the null is correct. Therefore, we reject the null hypothesis, and accept the alternative hypothesis.

* If $p_{value} > 0.05$ is not statistically significant and indicates strong evidence for the null hypothesis. This means we retain the null hypothesis and reject the alternative hypothesis. We should note that we cannot accept the null hypothesis, we can only reject the null or fail to reject it.

The p-value and α have the same formula, but α is a property of the test, computed before you see the data. The p-value is a property of the data.

A.3.1 Statistical tests and p-value

In a statistical test, the *p-value* is the probability of getting the observed value of the test statistic, or a value with even greater evidence against H_0, if the null hypothesis is true.
A result is said to be statistically significant when it is unlikely that it could be obtained by mere chance. In contrast, a statistically insignificant result is one that possibly (more than 5% chance) was obtained by chance.
The p-value is only an indication of how strange the measured result q_{meas} is, assuming the null hypothesis is correct. To obtain the p-value of our result we ask the question: if this experiment were repeated several times, under the null hypothesis, in which fraction of experiment would we obtain a result as extreme, or more extreme than what we observed ?
If the p-value is very small, we can conclude that our q is not compatible with the null hypothesis i.e. we can conclude that the null hypothesis is false. Even in this case, it does not tell us that

our alternative hypothesis is true. The p-value is defined as:

$$p_\mu = \int_{q_{\mu,obs}}^{\infty} f(q_\mu|\mu)dq \tag{A.21}$$

where q_{obs} is the observed value of the test statistic q in data and and $f(q_\mu|\mu)$ represents the probability density function (pdf) of q. μ which corresponds to the two hypotheses:

- ▷ $\mu = 0$: the null hypothesis, background-only hypothesis (b).
- ▷ $\mu = 1$: the alternative hypothesis, signal+background hypothesis (s+b).

The p-value for the signal+background hypothesis is:

$$p_{s+b} = P(q \geq q_{obs}|s+b) = \int_{q_{obs}}^{\infty} f(q|s+b)dq. \tag{A.22}$$

where $f(q|s+b)$ is the p.d.f of q under the assumption of the alternative hypothesis. Equivalently for the null hypothesis:

$$p_b = P(q \leq q_{obs}|b) = \int_{q_{obs}}^{-\infty} f(q|b)dq. \tag{A.23}$$

Figure A.1 shows the distribution of the test statistic q under the s+b and b hypotheses.

In particle physics, the significance of an observation is measured in terms of standard deviations, "**sigma**". The standard deviation measures the likelihood that an observation is due to chance rather than signaling a discovery.

- **Two sigma** effects are likely to occur with a regularity comparable to that of two die rolls producing two consecutive sixes.
- **Three sigma** effect corresponds to a probability of a few thousandths that an observation is due to chance: this is the point at which it is generally accepted that an observation becomes interesting. A result of 3 sigmas is qualified as *evidence*.
- **Four sigma** corresponds to a high probability.
- We need **five sigma** when there is a discovery. At this point, it is considered that there is less than a one in a million chance that the sighting is due to chance. A result of 5 sigmas is considered a true observation.
- **Six sigma** is a one in 500 million chance that the result is the result of fluctuations due to chance.

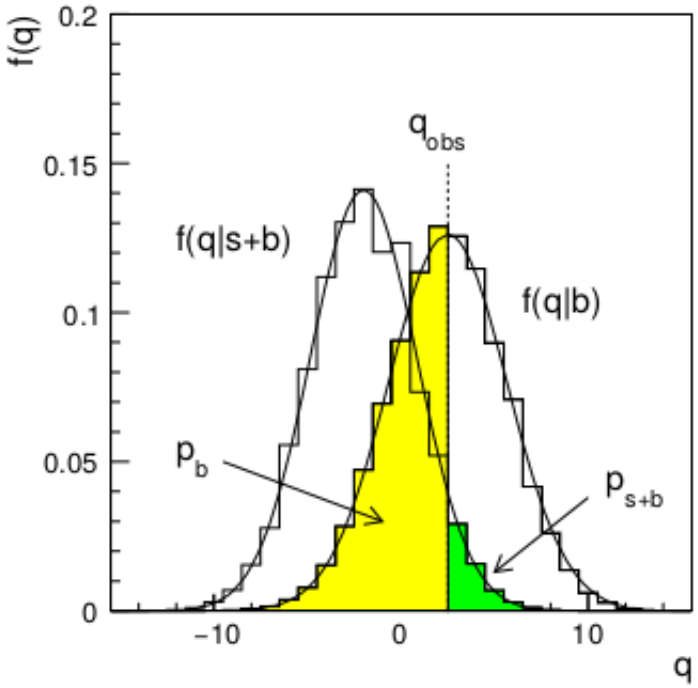

Figure A.1: The distribution of the test statistic q under the s + b and b hypotheses; the corresponding $p-value$ for the test statistic observed in data q_{obs} [71].

A.3.2 The Neyman-Pearson lemma

The Neyman-Pearson lemma ensures that the selection criterion can be considered optimal if it achieves the smallest misidentification probability (β) for a desired value of a signal efficiency $(1-\alpha)$, or a fixed significance level(α), which depends on the likelihood ratio evaluated for the observed data sample x under the two hypotheses H_1 and H_0:

$$\lambda(x) = \frac{L(x|H_1)}{L(x|H_0)} > k_\alpha \tag{A.24}$$

where $L(x|H_0)$ and $L(x|H_1)$ are the values of the likelihood functions for the two considered hypotheses. k_α is a constant whose value depends on the fixed significance level α.
Multivariate discriminators are samples with multiple variables of a statistical test provided by algorithms. The algorithms are "trained" using data samples simulated with computer algorithms (Monte Carlo) i.e. where either H_0 or H_1 is known to be true. Among the most common problems that arise with training of multivariate algorithms, the size of training samples is necessarily finite, hence the true distributions for the considered hypotheses cant be determined exactly form the training sample distribution.

A.4 Projective likelihood ratio

In case of independent variables, the likelihood functions appearing in the numerator and denominator of equation (A.24) can be factorized as product of one-dimensional pdf. Even in the cases when variables are not independent, this can be taken as an approximate evaluation of the Neyman-Pearson likelihood ratio, so we can write:

$$\lambda(x) = \frac{L(x_1, ..., x_n|H_1)}{L(x_1, ..., x_n|H_0)} \simeq \frac{\prod_{i=1}^{n} f_i(x_i|H_1)}{\prod_{i=1}^{n} f_i(x_i|H_0)} \tag{A.25}$$

The approximation may be improved if a proper rotation is first applied to the input variables in order to eliminate their correlation. This approach is called principal component analysis.

A.5 Profile likelihood ratio

The likelihood $L(\mu, \theta)$ is a function of parameter of interest μ and nuisance parameters θ. To test a hypothesized value of μ in chapter 4 are based on the profile likelihhod ratio:

$$\lambda(\mu) = \frac{L(\vec{x}; \mu, \hat{\hat{\theta}})}{L(\vec{x}; \hat{\mu}, \hat{\theta})} \tag{A.26}$$

In the denominator $\hat{\mu}$ and $\hat{\theta}$ are the best fit values of μ and θ corresponding to the observed data sample, and in the numerator $\hat{\hat{\theta}}$ is the best fit value for θ obtained for a fixed value of μ. We have already assumed that all parameters are treated as nuisance parameters and this is the only parameter of interest. The motivation for the choice of (A.26) as the test statistic comes from Wilks theorem that allows to approximate asymptotically $-2\ln\lambda(\mu)$ as a χ^2.

For example:

The data thus consist of two measured values: n and m. We have one parameter of interest, μ, and one nuisance parameter, b. The likelihood function for μ and b is the product of two Poisson terms:

$$L(\mu, b) = \frac{(\mu s + b)^n}{n!} \exp^{-(\mu s+b)} \frac{(\tau b)^m}{m!} \exp^{-\tau b} \tag{A.27}$$

Since $L(\mu, b)$ is a function of the two variables μ and b we use partial derivatives to find the maximum likelihood estimator (MLE). The easy value to find is $\hat{\mu}$:

$$\frac{\partial L(\mu, b)}{\partial \mu} = 0 \Longrightarrow \hat{\mu} = \frac{n - \frac{m}{\tau}}{s}. \tag{A.28}$$

and the same for $\hat{b}$:

$$\frac{\partial L(\mu, b)}{\partial b} = 0 \Longrightarrow \hat{b} = \frac{m}{\tau}. \tag{A.29}$$

To find the MLE $\hat{\hat{b}}$ for a specified μ:

$$\frac{\partial^2 L(\mu, b)}{\partial b^2}, \qquad \hat{\hat{b}} = \frac{n + m - (1+\tau)\mu s}{2(1+\tau)} + \left[\frac{(n + m - (1+\tau)\mu s)^2 + 4(1+\tau)m\mu s}{4(1+\tau)^2}\right] \tag{A.30}$$

A.5.1 Test statistic $q_\mu = -2 \ln \lambda(\mu)$

The definition of $\lambda(\mu)$ in equation (A.26), shows that the profile likelihood is ranging between 0 and 1, with λ near 1 implying good agreement between the data and the hypothesized value of μ. It is convenient to define the test statistic:

$$q_\mu = -2 \ln \lambda(\mu) \tag{A.31}$$

as the basis of a statistical test. Where higher values of q_μ thus correspond to increasing incompatibility between the data and μ.
Minimising the statistic q_μ, or, equivalently, maximising $\lambda(\mu)$, allows to determine the value of the signal strength μ which is the most compatible with the observed data.

A.6 Nuisance Parameters

In statistics, a nuisance parameter is any parameter which is not of immediate interest but which must be taken into account in the analysis of the parameters which pose an interest.
To establish the discovery in particle physics is based on a frequentist significance test using a likelihood ratio as a test statistic. In addition to the parameters of interest such as the speed (cross section) of the signal processing, the signal and background models will generally contain nuisance parameters whose values are not taken as known a priori but must rather be adjusted from the data.

A.7 CL_s method

The CL_s method consists of replacing the p-value used to define the critical region by:

$$CL_s = \frac{p_{H_1}}{1 - p_{H_0}} = \frac{p_\mu}{p_{\mu=0}} = \frac{p_{s+b}}{1 - p_b} \tag{A.32}$$

Where H_1 is the alternative hypothesis, H_0 is the null hypothesis. The CL_s method can be defined for any test statistic, however in the context of setting limits. If a value of μ has a value of CL_s below a value threshold α then the value of μ will be excluded with a confidence level of $1 - \alpha$. To obtain a low value of CL_s and therefore the exclusion of the value μ, a low

value of p_μ is no longer sufficient. It is also necessary that $p_{\mu=0}$ is very low which means that the observation carried out is strongly incompatible with the background assumption, so the experiment has some sensitivity to rule out the signal assumption. In the case of an experiment infinitely sensitive to exclude the hypothesis μ, the exclusion by the standard statistical test is found.

Bibliography

[1] The Nobel Prize in Physics 2013 - NobelPrize.org. https://www.nobelprize.org/prizes/physics/2013/summary/.

[2] S. Weinberg. A model of leptons. Phys. Rev. Lett. Vol.19, p.1264, (1967).

[3] A. Salam and J. C. Ward. Weak and electromagnetic interactions. Nuovo Cimento Vol.XI N°4, (1959).

[4] A. Salam. Renormalizability of gauge theories. Phys. Rev. Vol.127, p.331, (1962).

[5] A. Salam. Weak and electromagnetic interactions. Elementary Particle Theory, ed. N. Svartholm, p.367-377, (1968).

[6] S. L. Glashow and M. Gell-Mann. Gauge theories of vector particles. California Institute of Technology, Report CTSL-28, (1961).

[7] G. Aad *et al.* ATLAS Collaboration. Observation of a new particle in the search for the Standard Model Higgs boson with the ATLAS detector at the LHC. Physics Letters B 716, p.1-29, arXiv:1207.7214 [hep-ex], (2012).

[8] CMS Collaboration. Observation of a new boson at a mass of 125 GeV with the CMS experiment at the LHC. Physics Letters B 716, p.30-61, (2012).

[9] P. Higgs. Broken symmetries and the masses of gauges bosons. Phys. Rev. Lett. Vol.13 N°16, p.508, (1964).

[10] F. Englert and R. Brout. Broken symmetry and the mass of gauge vector mesons. Phys. Rev. Lett. Vol.13 N°9, p.321, (1964).

[11] J. Goldstone. Field theories with superconductor solutions. Nuovo Cimento Vol.XIX N°1, p.150, (1961).

[12] J. Goldstone, A. Salam, and S. Weinberg. Broken symmetries. Phys. Rev. Vol.117 N°3, p.965, (1962).

[13] G. S. Guralnik, C. R. Hagen, and T. W. B. Kibble. Global conservation laws and massless particles. Phys. Rev. Lett. Vol.13 N°20, p.585, (1964).

[14] **(Figure)**. https://external-preview.redd.it/FjCgC3Vz3uzfthWC_bBOz2odTdsA1BFrSbwHkm739FY.png?auto=webp&s=a99e04e27ee86cb279bc6de9c75d6b5d68828a89.

[15] **(Figure)** A Historical Profile of the Higgs Boson - CERN Document Server. http://cds.cern.ch/record/1638469/plots.

[16] P. A. Zyla *et al.* Particle Data Group. Review of Particle Physics. Progress Theoretical Experimental Physics 083C01, (2020).

[17] **(Figure)** Masses of leptons, of quarks, and of the Higgs boson and neutrino mass... - Download Scientific Diagram. https://www.researchgate.net/figure/Masses-of-leptons-of-quarks-and-of-the-Higgs-boson-and-neutrino-mass-splittings-in-t fig8_270677389.

[18] K. Aoki, Z. Hioki, R. Kawabe, M. Konuma, and T. Muta. Electroweak Theory. Supplement of the Progress of Theoretical Physics N°73, (1982).

[19] A. Denner. Techniques for the calculation of electroweak radiative corrections at the one-loop level and results for W-physics at LEP200. Fortschr. Phys. Vol.41 N°4, arXiv:0709.1075 [hep-ph], (1993).

[20] G. Bélanger, F. Boudjema, J. Fujimoto, T. Ishikawa, T. Kaneko, K. Kato, and Y. Shimizu. Automatic Calculations in High Energy Physics and GRACE at one-loop. Physics Reports 430, arXiv:hep-ph/0308080, (2006).

[21] Particle Data Group - 2020 Review. https://pdg.lbl.gov/index.html.

[22] The CTEQ Meta-Page. https://www.physics.smu.edu/scalise/cteq/.

[23] J. Gao P. Nadolsky, M. Guzzi, J. Huston, H. L. Lai, Z. Li, J. Pumplin, D. Stump, and C. P. Yuan. Progress in CTEQ-TEA PDF analysis. arXiv:1206.3321 [hep-ph], (2012).

[24] A. D. Martin, W. J. Stirling, R. S. Thorne, and G. Watt. Parton distributions for the LHC. Eur. Phys. J. C 63, arXiv:0901.0002 [hep-ph], (2009).

[25] **(Figure)** CERNYellowReportPageBR2010 - LHCPhysics - TWiki. https://twiki.cern.ch/twiki/bin/view/LHCPhysics/CERNYellowReportPageBR2010.

[26] M. D. Schwartz. TASI Lectures on Collider Physics. Lecture notes, arXiv:1709.04533v1 [hep-ph], (2017).

[27] The Large Hadron Collider - CERN. https://home.cern/science/accelerators/large-hadron-collider.

[28] **(Figure)** Le LHC en bref - LHC France. https://www.lhc-france.fr/spip.php?rubrique1.

[29] D. Griffiths. Introduction to elementary particles. Wiley, Physics textbook, (1987).

[30] L. Marleau. Introduction à la physique des particules. Université Laval, Québec, (1998-2017).

[31] **(Figure)** The ATLAS detector layout - Download Scientific Diagram. https://www.researchgate.net/figure/The-ATLAS-detector-layout-40_fig9_274319826.

[32] **(Figure)** Cutaway diagrams of CMS detector - CERN Document Server. http://cds.cern.ch/record/2665537/files/.

[33] **(Figure)** C. Doglioni. Measurement of the inclusive jet cross section with the ATLAS detector at the Large Hadron Collider. Springer Theses, (2012).

[34] **(Figure)** How ATLAS detects particles : diagram of particle paths in the detector - CERN Document Server. https://cds.cern.ch/record/1505342.

[35] Trigger and Data Acquisition System. https://atlas.cern/discover/detector/trigger-daq.

[36] R. P. Feynman. The behavior of hadron collisions at extreme energies. Conf. Proc. C 690905, p.237-258, (1969).

[37] A. Castelli. Measuring the Higgs boson mass using event-by-event uncertainties. PhD Thesis, CERN-THESIS-2015-118, (2015).

[38] Y. Li. Observation of the higgs boson and measurement of its properties in the HWW* channel with the ATLAS detector at the LHC. PhD Thesis, Université Paris Sud - Paris XI; Nanjing University (Chine), tel-01157549 [hep-ex], (2015).

[39] A. Calandri. Properties of the Higgs boson in the 4 leptons final state with the ATLAS experiment at the LHC : mass, limit on the high mass contribution and on the Higgs width. PhD Thesis, Université Paris Sud - Paris XI, tel-01187079 [hep-ex], (2015).

[40] **(Figure)** International Physics Masterclasses. https://atlas.physicsmasterclasses.org/en/zpath_hboson.htm.

[41] M. Machet. Higgs boson production in the diphoton decay channel with CMS at the LHC: first measurement of the inclusive cross section in 13 TeV pp collisions, and study of the Higgs coupling to electroweak vector bosons. PhD Thesis, Université Paris-Saclay, tel-01400151 [hep-ex], (2016).

[42] **(Figure)** G. Luisoni. An introduction to POWHEG. Presentation, CERN Indico, (2017).

[43] R. D. Ball, V. Bertone, F. Cerutti, L. Del Debbio, S. Forte, A. Guffant, J. I. Latorre, J. Rojo, and M. Ubiali. Impact of Heavy Quark Masses on Parton Distributions and LHC Phenomenology. Nucl. Phys. B 849, arXiv:1101.1300 [hep-ph], (2011).

[44] M. Ould Mohamed. Initiation aux méthodes Monte Carlo. Lecture notes, Université Saad Dahleb Blida-1, (2018).

[45] J. Alwall, R. Frederix, S. Frixione, V. Hirschi, F. Maltoni, O. Mattelaer, H.-S. Shao, T. Stelzer, P. Torrielli, and M. Zaro. The automated computation of tree-level and next-to-leading order differential cross sections, and their matching to parton shower simulations. Journal of High Energy Physics N°7, arXiv:1405.0301 [hep-ph], (2014).

[46] A. Goswami, R. Nayak, B. K. Nandi, and S. Dash. Effect of color reconnection and rope formation on resonance production in p-p collisions in Pythia 8. arXiv:1911.00559 [hep-ph], (2019).

[47] MadGraph Home Page. http://madgraph.phys.ucl.ac.be/.

[48] ATLAS Open Data - GitBook. http://opendata.atlas.cern/books/current/openatlasdatatools/_book/.

[49] Home - ATLAS Open Data 13 TeV Documentation. http://opendata.atlas.cern/release/2020/documentation/.

[50] CERN Open Data Portal. http://opendata.cern.ch/record/15005.

[51] ATLAS Collaboration. ATLAS 13 TeV samples collection at least four leptons (electron or muon), for 2020 Open Data release. CERN Open Data Portal, 10.7483/OPENDATA.ATLAS.2Y1T.TLGL, (2020).

[52] ATLAS Collaboration. Measurements of the properties of the Higgs-like boson in the four lepton decay channel with the ATLAS detector using 25 fb^{-1} of proton-proton collision data. ATLAS notes, ATLAS-CONF-2013-013, (2013).

[53] P. Nason, C. Oleari, M. Rocco, and M. Zaro. An interface between the POWHEG BOX and MadGraph5_aMC@NLO. arXiv:2008.06364 [hep-ph], (2020).

[54] P. Golonka and Z. Was. PHOTOS Monte Carlo: a precision tool for QED correctionsin Z and W decays. Eur. Phys. J. C 45, p.97-107, (2006).

[55] G. Echevarria, Z. Kang, and J. Terry. Global analysis of the Sivers functions at NLO+NNLL in QCD. arXiv:2009.10710 [hep-ph], (2020).

[56] H. M. Georgi, S. L. Glashow, M. E. Machacek, and D. V. Nanopoulos. Higgs bosons from two-gluon annihilation in proton-proton collisions. Phys. Rev. Lett. 40, p.692, (1978).

[57] A. Denner, S. Dittmaier, and A. Mück. PROPHECY4F 3.0: A Monte Carlo program for Higgs-boson decays into four-fermion final states in and beyond the Standard Model. arXiv:1912.02010 [hep-ph], (2020).

[58] E. Bóthmänn and D. Napoletano. Automated evaluation of electroweak Sudakov logarithms in Sherpa. arXiv:2006.14635 [hep-ph], (2020).

[59] S. Jadach, Z. Was, R. Decker, and J. H. Kühn. The τ decay library TAUOLA, version 2.4. Computer Physics Communications 76, p.361-380, (1993).

[60] J. T. Childers, T. D. Uram, T. J. LeCompte, M. E. Papka, and D. P. Benjamin. Adapting the serial Alpgen parton-interaction generator to simulate LHC collisions on millions of parallel threads. Computer Physics Communications 210, p.5459, (2017).

[61] P. Kant, O. M. Kind, T. Lohse T. Kintscher, T. Martini, S. Mölbitz, P. Rieck, and P. Uwer. HATHOR for single top-quark production: Updated predictions and uncertainty estimates for single top-quark production in hadronic collisions. arXiv:1406.4403 [hep-ph], (2015).

[62] ATLAS Collaboration. Luminosity determination in pp collisions at $\sqrt{s}$= 13 TeV using the ATLAS detector at the LHC. ATLAS notes, ATLAS-CONF-2019-021, (2019).

[63] Counting collisions - ATLAS Experiment at CERN. https://atlas.cern/updates/news/counting-collisions.

[64] ATLAS Open Data. https://atlas.cern/resources/opendata.

[65] **(Figure)** Measurement of the Higgs boson mass in the $H \to ZZ^* \to 4l$ decay channel with $\sqrt{s} = 13$ TeV pp collisions using the ATLAS detector at the LHC. https://atlas.web.cern.ch/Atlas/GROUPS/PHYSICS/CONFNOTES/ATLAS-CONF-2020-005/.

[66] **(Figure)** G. Aad *et al.* ATLAS Collaboration. Measurements of Higgs boson production and couplings in the four-lepton channel in pp collisions at center-of-mass energies of 7 and 8 TeV with the ATLAS detector. Physical Review D 91 p.15, arXiv:1408.5191 [hep-ex], (2015).

[67] E. Gross. Practical Statistics for High Energy Physics. Proceedings of the 2015 European School of High-Energy Physics, CERN Yellow Reports: School Proceedings 4/2017, CERN-2017-008-SP, (2017).

[68] L. Lista. Practical Statistics for Particle Physicists. arXiv:1609.04150v2 [physics.data-an], (2017).

[69] L. Lista. Statistical Methods for Data Analysis in Particle Physics. Lecture Notes in Physics 909, Springer International Publishing, (2016).

[70] R. J. Barlow. Practical Statistics for Particle Physics. arXiv:1905.12362 [physics.data-an], (2019).

[71] G. Cowan, K. Cranmer, E. Gross, and O. Vitells. Asymptotic formulae for likelihood-based tests of new physics. arXiv:1007.1727v3 [physics.data-an], (2013).

[72] **(Figure)** The Bitcoin Bell-Curve - A Long-Term Solution to Global Wealth & Income Inequality - by Hass McCook - Medium. https://medium.com/@hassmccook/the-bitcoin-bell-curve-a-long-term-solution-to-global-wealth-income-inequality-de995